UNIVERSITY OF CALIFORNIA SAN DIEGO

# Oceanic and Atmospheric Processes that Contribute to Arctic Warming: Insights from Idealized Models

A dissertation submitted in partial satisfaction of the
requirements for the degree Doctor of Philosophy

in

Oceanography

by

Emma Beer

Committee in charge:

Professor Ian Eisenman, Chair
Professor Nicholas J. Lutsko
Professor Jennifer A. MacKinnon
Professor David Saintillan
Professor Fiammetta Straneo

2023

The Dissertation of Emma Beer is approved, and it is acceptable in quality and form for publication on microfilm and electronically.

University of California San Diego

2023

TABLE OF CONTENTS

LIST OF FIGURES

LIST OF TABLES

ACKNOWLEDGEMENTS

First, I would like to acknowledge my advisor, Ian Eisenman. Thanks for the constant encouragement and engagement throughout my PhD. This inspired and motivated me in my research and other endeavors. I would also like to acknowledge my PhD committee members, collaborators, and the whole Eisenman group for providing useful feedback and additional support along the way. Also thanks to Shantong Sun and Matt Luongo for being a great office and lab mate, respectively. And a special acknowledgement to the 2017 PO cohort at Scripps: Alice Ren, Annie Adelson, Bobby Sanchez, Channing Prend, Lauren Kim, and Noel Brizuela. Thanks for making the early years fun and for creating such a welcoming space in a new environment.

Finally, I would like to acknowledge all the people who distracted me from work in various forms. In San Diego this includes friends, housemates, and most of all Bobby. And in England, I would like to acknowledge my family and friends, especially my parents. Thanks for always being there, for making trips out to San Diego, and for negotiating time zones.

Chapter 2, in full, is a reprint of the material as it appears in Journal of Climate, 2022. Beer, E., and I. Eisenman, 2022: Revisiting the role of the water vapor and lapse rate feedbacks in the Arctic amplification of climate change. *Journal of Climate*, **35(10)**, 2975-2988. The dissertation author was the primary investigator and author of this paper.

Chapter 3, in full, is a reprint of the material as it appears in Geophysical Research Letters, 2020. Beer, E., I. Eisenman, and T. J. W. Wagner, 2020: Polar amplification due to enhanced heat flux across the halocline. *Geophysical Research Letters*, **47(4)**. The dissertation author was the primary investigator and author of this paper.

Chapter 4, in full, is a reprint of the material as it appears in Journal of Physical Oceanography, 2023. Beer, E., I. Eisenman, T. J. W. Wagner, and E. C. Fine, 2023: A Possible Hysteresis in the Arctic Ocean due to Release of Subsurface Heat during Sea Ice Retreat. *Journal of Physical Oceanography*, **53(5)**, 1323–1335. The dissertation author was the primary investigator and author of this paper.

## VITA

| | |
|---|---|
| 2016 | Bachelor of Arts in Mathematics, University of Oxford |
| 2020 | Master of Science in Oceanography, University of California San Diego |
| 2023 | Doctor of Philosophy in Oceanography, University of California San Diego |

## PUBLICATIONS

Beer, E., I. Eisenman, T. J. W. Wagner, and E. C. Fine, 2023: A Possible Hysteresis in the Arctic Ocean due to Release of Subsurface Heat during Sea Ice Retreat. *Journal of Physical Oceanography*, **53(5)**, 1323–1335.

Beer, E., and I. Eisenman, 2022: Revisiting the role of the water vapor and lapse rate feedbacks in the Arctic amplification of climate change. *Journal of Climate*, **35(10)**, 2975-2988.

Beer, E., I. Eisenman, and T. J. W. Wagner, 2020: Polar amplification due to enhanced heat flux across the halocline. *Geophysical Research Letters*, **47(4)**.

Johnson, H. L., S. B. Cornish, Y. Kostov, E. Beer, and C. Lique, 2018: Arctic Ocean freshwater content and its decadal memory of sea-level pressure. *Geophysical Research Letters*, **45(10)**, 4991–5001.

ABSTRACT OF THE DISSERTATION

Oceanic and Atmospheric Processes that Contribute to Arctic Warming: Insights from Idealized Models

by

Emma Beer

Doctor of Philosophy in Oceanography

University of California San Diego, 2023

Professor Ian Eisenman, Chair

The surface temperature in the Arctic has warmed at twice the rate of the global mean temperature during recent decades. This Arctic amplification of global warming has been a striking feature of climate change, and many studies have investigated what processes contribute to this phenomenon. Many of these processes are often described in the context of climate feedbacks using analyses focused on top-of-the-atmosphere radiative changes. In this context, regional surface warming can then be partitioned into contributions from each feedback process. However, this partitioning can be complicated by interactions between feedbacks themselves and atmospheric heat transport. In the second chapter, we instead apply a feedback-locking

approach and evaluate the resulting changes in surface temperature. These results are strikingly different from previous feedback analyses, highlighting the important role of interactions within the climate system. This chapter and many other previous studies focus only on the role of atmospheric and surface processes in Arctic amplification. However, substantial questions remain regarding the role of ocean heat transport. In the third chapter, we investigate changes in oceanic heat fluxes under global warming. We find a mechanism associated with the presence of sea ice that drives enhanced horizontal ocean heat transport into the Arctic region and can contribute substantially to Arctic amplification if this heat is allowed to reach the surface. Currently, only a small amount of the heat stored at depth in the Arctic Ocean can reach the surface, but recent observational studies have argued that sea ice retreat could result in enhanced vertical mixing. In the fourth chapter, we investigate the impacts of a positive feedback whereby increased vertical mixing due to sea ice retreat causes the previously isolated subsurface Arctic Ocean heat to melt more sea ice. We find that an abrupt "tipping point" can occur under global warming, with an associated hysteresis window, for a limited range of parameters. Throughout the thesis, we use idealized models to show how ocean and climate processes can impact Arctic warming, providing insights into possible physical mechanisms that could be at play now or in the future.

# Chapter 1

# Introduction

During the past 20 years, surface temperatures in the Arctic have increased more than twice as fast as the global mean (Pörtner et al., 2019). This process, known as Arctic amplification, is a robust feature of both observations of the past and model projections of the future (cf. Serreze et al., 2000; Holland and Bitz, 2003; Collins et al., 2013; England et al., 2021). This has local consequences for the extent of sea ice, and the ecosystems and communities which depend on it, as well as possible global consequences for weather patterns and ocean currents. Given the large consequences of Arctic amplification, there has been a sustained effort to improve predictions and observations of Arctic temperatures and sea ice extent through collaborative international projects. For example, during the duration of this PhD thesis, there has been the Polar Prediction Project (PPP) by the World Meteorological Organization, the Sea Ice Prediction Network–Phase 2 (SIPN2), and the Multidisciplinary drifting Observatory for the Study of Arctic Climate (MOSAiC). However, there is still substantial variability across climate models in the magnitude of projected Arctic amplification (Lee et al., 2021).

A large source of variance in projected surface warming between climate models can be attributed to differences in climate feedbacks (Bonan et al., 2018). Feedbacks in the climate system can act to enhance or dampen temperature changes resulting from greenhouse gas forcing. Feedbacks are positive if they lead to more warming after a heating perturbation, and negative if they lead to less warming after a heating perturbation. In models and observations, there

are more positive feedbacks in the Arctic than in other regions. However, the contribution of individual feedback processes to Arctic amplification is complicated by changes in atmospheric heat transport associated with the strength of individual feedbacks and changes in regional warming (Langen et al., 2012; Alexeev and Jackson, 2013; Merlis, 2014; Russotto and Biasutti, 2020). This leads to multiple ways of interpreting the contribution of feedbacks to Arctic amplification and highlights the important role of heat transport in the climate system.

The contribution of surface and atmospheric processes to Arctic warming, such as the surface albedo feedback (e.g. Hall, 2004), have been well documented. However, the role of ocean processes in Arctic amplification is less certain. For example, increases in high-latitude ocean heat transport (OHT) are found to be positively correlated with Arctic amplification (Holland and Bitz, 2003; Mahlstein and Knutti, 2011; Nummelin et al., 2017). However, the underlying mechanism for the increase in OHT has remained elusive. Furthermore, substantial sea ice retreat in the Arctic Ocean is reducing the barrier between the ocean and atmosphere. In the Arctic Ocean, water flows in from the Atlantic Ocean and Pacific Ocean where it is warmed at the surface and resides at depth as a reservoir of potential heat. It is estimated that enough heat is stored in the deeper layers of the Arctic Ocean to melt all the Arctic sea ice many times over. Hence, increases in heat fluxes from these deeper layers to the surface of the Arctic Ocean have potentially large consequences.

In the thesis, I examine specific processes and interactions in the atmosphere and ocean that contribute to Arctic warming. In the second chapter, I investigate how warming from climate feedbacks and atmospheric heat transport interact and change regional warming patterns. In the third chapter, I look at a mechanism that causes increased horizontal heat transport into the Arctic Ocean, as well as enhanced Arctic amplification. In the fourth chapter, I investigate a possible positive feedback in the Arctic Ocean between retreating sea ice and enhanced vertical heat fluxes in the ocean, focusing on the possibility of a "tipping point" during sea ice decline. Many of these processes are alluded to in observational studies but remain difficult to capture using comprehensive climate models. Using idealized models allows us to build understanding

of physical processes using a simple environment and to test hypotheses that can be challenging to assess in more complex models. Understanding processes at a fundamental level should help to detect and resolve model biases, contributing to reducing the uncertainty in future projections of Arctic amplification.

# Background

## Climate feedbacks

Climate feedbacks play an important role in Arctic amplification and are the focus of the second chapter. Some of the major climate feedbacks are briefly summarized here.

The surface albedo feedback (SAF), which has been identified as the primary driver of Arctic amplification in some previous studies (Manabe and Wetherald, 1975; Manabe and Stouffer, 1980; Hall, 2004; Screen and Simmonds, 2010; Taylor et al., 2013), results from a perturbation to the sea ice cover, since a darker ocean absorbs more solar radiation than a reflective sea ice cover. Other processes that have also been found to contribute substantially to Arctic amplification include latitudinal variations in the Planck feedback and the lapse rate feedback (Pithan and Mauritsen, 2014; Stuecker et al., 2018; Goosse et al., 2018). The Planck feedback is governed by the Stefan-Boltzmann law which describes how warmer temperatures lead to more outgoing longwave radiation (OLR), and is therefore a negative feedback globally. However, this relationship is nonlinear, such that for a globally uniform increase in temperature, there would be smaller increases in OLR in cold high-latitude regions, which results in larger increases in warming. The lapse rate feedback arises from vertically uneven warming in the atmosphere. It acts as a positive feedback in the Arctic and a negative feedback in lower latitudes, meaning that it amplifies warming in the Arctic and dampens warming in the tropics. Another major climate feedback is the water vapor feedback, which arises because a warmer atmosphere can hold more water vapor which is a greenhouse gas. It is a positive feedback everywhere, increasing the level of global warming, but it is strongest in low latitudes.

## Arctic Ocean stratification

The later chapters focus on ocean processes that occur due to warm reservoirs of water at depth in the Arctic Ocean. Features of the stratification in the Arctic Ocean are summarized here.

The polar oceans are stratified primarily by salt. This is in contrast to most of the Earth's oceans, which are primarily temperature stratified. Within the Arctic Ocean (especially in the Eurasian Basin), a pool of warm, salty water from the Atlantic sits below a fresh and cold surface mixed layer (SML) consisting of polar origin water. The two water masses are separated by a layer in which salinity rapidly changes, known as the halocline.

Atlantic Water (AW) flows into the Arctic through Fram Strait and the Barents Sea and resides at depths of 200–800 m in the central Arctic (Carmack et al., 2015). In the Pacific sector, the AW is cooler and sits at a lower depth with Pacific-origin water of an intermediate density at a depth centered around 50 m (Timmermans et al., 2014), as seen in Fig. 1.1.

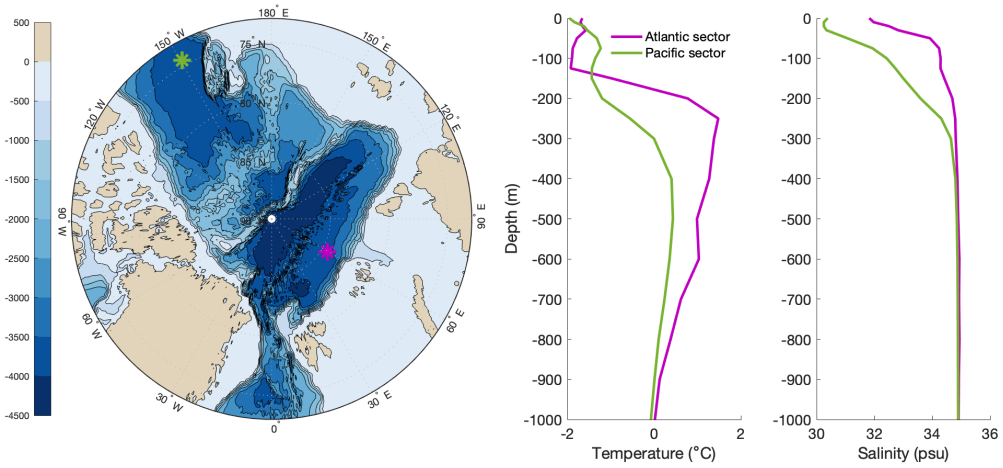


**Figure 1.1.** Examples of stratification in the Atlantic and Pacific sectors of the Arctic. (a) Arctic bathymetry. Profiles of temperature (b) and salinity (c) from the Atlantic (pink) and Pacific (green) sectors in the Arctic Ocean are indicated by the stars in panel (a). Bathymetry data is from ETOPO1 (Amante and Eakins, 2009) and temperature and salinity data is March climatology from LEVITUS94 (Levitus et al., 1994; Levitus and Boyer, 1994).

Increased stratification from the Pacific water limits heat fluxes from the AW to the surface. Only very small heat fluxes (0.05-0.3 W $m^{-2}$) have been observed in the Pacific sector with

double-diffusive staircases (which require very low mixing rates) being a primary mechanism of vertical heat transport (Timmermans et al., 2008). This is in contrast to the Atlantic sector, where the AW is higher in the water column and there is less stratification, meaning the AW is more readily mixed to the surface. Here, heat fluxes observed typically range from around 1-10 W $m^{-2}$ (Carmack et al., 2015; Polyakov et al., 2017; Peterson et al., 2017) but can be as high as 100 W $m^{-2}$ north of Svalbard where AW enters the Arctic (Sirevaag and Fer, 2009; Peterson et al., 2017).

## Idealized climate model developments

This thesis uses a range of idealized models primarily built of two types of models that have been useful tools in climate science for analyzing climate feedbacks and tipping points.

Single column models (SCMs) consist of a single (vertical) space dimension. Versions have been used to study tipping points associated with the SAF, some of which include sea ice thermodynamics, a mixed layer, and seasonal variations (Eisenman and Wettlaufer, 2009; Eisenman, 2012). Energy balance models (EBMs) typically refer to a model based on the top-of-the-atmosphere energy balance with solar forcing, outgoing longwave radiation (OLR), a representation of meridional heat transport, and latitudinal variations (Budyko, 1969; Sellers, 1969; North, 1975).

A common extension of EBMs is to diffuse moist static energy (MSE) as a better representation of latitudinal energy transport. This is based on the Clausius-Clapeyron relation, relating water vapor pressure to temperature, to model MSE as a function of the surface temperature assuming constant relative humidity in the atmosphere. It has been shown that this type of model (a Moist Energy Balance Model or MEBM) does a reasonably good job of approximating the zonal-mean temperature response to $CO_2$ doubling in GCMs, and this type of model has provided useful insights into climate mechanisms and model uncertainty (Flannery, 1984; Hwang and Frierson, 2010; Roe et al., 2015; Merlis and Henry, 2018; Bonan et al., 2018).

# Chapter 2

# Revisiting the role of the water vapor and lapse rate feedbacks in the Arctic amplification of climate change

**Abstract**

The processes that contribute to the Arctic amplification of global warming are often described in the context of climate feedbacks. There are multiple ways of defining how a climate feedback contributes to Arctic amplification which can lead to substantially different results. Previous studies have used a traditional feedback analysis framework to partition the regional surface warming into contributions from each feedback process. However, this partitioning can be complicated by interactions in the climate system. Here we focus instead on the physically intuitive approach of inactivating individual feedback processes during forced warming and evaluating the resulting change in the surface temperature field. We investigate this using a moist energy balance model with spatially-varying feedbacks that are specified from comprehensive climate model results. We find that when warming is attributed to each feedback process by comparing how the climate would change if the process were not active, the water vapor feedback is the primary reason that the Arctic region warms more than the tropics, and the lapse rate feedback has a neutral effect on Arctic amplification by cooling the Arctic and the tropics by approximately equivalent amounts. These results are strikingly different from previous feedback analyses, which identified the lapse rate feedback as the largest contributor to Arctic amplification,

with the water vapor feedback being the main opposing factor by warming the tropics more than the Arctic region. This highlights the importance of comparing different approaches of analyzing how feedbacks contribute to warming in order to build a better understanding of how feedbacks influence climate changes.

## 2.1 Introduction

The Arctic is warming at a faster rate than lower latitudes, a process known as Arctic amplification, and it is projected to continue to do so in the future (e.g., Collins et al., 2013). Climate feedbacks play an important role in Arctic amplification, and different feedbacks have been variously proposed to be the main drivers (e.g., Hall, 2004; Screen and Simmonds, 2010; Taylor et al., 2013; Pithan and Mauritsen, 2014; Goosse et al., 2018; Stuecker et al., 2018). These include latitudinal variations in the Planck feedback, since the Planck feedback is a weaker negative feedback in the polar regions; the lapse rate feedback which accounts for vertical variations in warming in the atmosphere; and the surface albedo feedback (SAF), which occurs due to the loss of snow and sea ice causing a change in absorbed solar radiation and has traditionally been thought to play a key role in Arctic amplification. Other climate processes that have also been proposed to play a role in Arctic amplification include the water vapor feedback, since a warmer atmosphere can hold more water vapor which is a greenhouse gas, as well as cloud feedbacks and poleward heat transport in both the atmosphere and ocean (e.g., Holland and Bitz, 2003; Alexeev et al., 2005; Francis and Hunter, 2006; Kay and Gettelman, 2009; Hwang et al., 2011; Mahlstein and Knutti, 2011; Alexeev and Jackson, 2013; Goosse et al., 2018; Beer et al., 2020).

However, there is substantial disagreement among studies about which processes are the primary drivers of Arctic amplification. This disagreement can be attributed in part to the complexity of the climate system making it challenging to quantify the effects of a single process. One metric that has been used to measure climate change is radiative forcing, which measures

the net change in the Earth's energy balance and allows a relatively simple method for comparing the climate response to different forcings and feedbacks (Myhre et al., 2013). A typical form of analysis using radiative forcing borrows the feedback framework from electrical engineering and relates perturbations of top-of-the-atmosphere (TOA) radiative forcing to changes in the global mean surface temperature (see Fig. 2.6 in appendix A). A traditional feedback analysis is then used to attribute warming caused by each feedback by partitioning the total change in global-mean surface temperature into individual contributions from feedbacks and other processes (e.g., Dufresne and Bony, 2008).

More recently, this traditional feedback analysis framework has been extended to look at regional warming due to local values of spatially-varying feedbacks (e.g., Armour et al., 2013), and a number of studies have investigated the contribution of each climate feedback to Arctic amplification. Using this method, the lapse rate feedback has been identified to contribute the most to Arctic amplification, followed by variations in the Planck feedback and the SAF (Pithan and Mauritsen, 2014; Stuecker et al., 2018; Goosse et al., 2018). The water vapor feedback, while being a positive feedback everywhere, is strongest in low latitudes and is found to contribute more to tropical warming than Arctic warming, making it the largest factor opposing Arctic amplification according to these studies. Studying local warming using such an analysis of the regional structure of feedbacks is relatively computationally efficient and allows for a clean decomposition of the surface warming, because the sum of the warming contributions of individual feedbacks is equal to the total warming. However, it does not consider changes in atmospheric heat transport (AHT) associated with the strength of individual feedbacks, which effects local warming and can have an influence on Arctic amplification (e.g., Langen et al., 2012; Merlis, 2014; Russotto and Biasutti, 2020). Therefore, one might argue that the traditional feedback analyses for the attribution of Arctic amplification do not have as clear a physical interpretation as the application of this method to attribute global-mean surface temperature changes.

Another method that has been used to assess the influence of climate feedbacks is feedback

locking. Warming can be attributed to individual feedbacks in this method by "locking" feedbacks in a model and looking at the change in forced warming when the feedback does not act on the perturbation to the climate system. For example, studies that locked the surface albedo feedback have found it has a large impact on polar amplification (Hall, 2004) but a smaller impact on the global mean temperature (Graversen and Wang, 2009). By locking cloud feedbacks, it has been found that global cloud radiative feedbacks have a warming effect on the Arctic, but both global and local Arctic cloud radiative feedbacks have little influence on Arctic amplification (Middlemas et al., 2020). Studies that lock climate feedbacks have also found that AHT can compensate for feedbacks being inactivated, causing the warming response to be similar to when all feedbacks are included (Langen et al., 2012). AHT has similarly been found to compensate for latitudinal differences in climate feedbacks, causing feedbacks to have similar contributions to warming both the tropical and polar regions (Russotto and Biasutti, 2020). A benefit of this method is that perturbing the strength of feedbacks in a model allows for other feedbacks and processes to adjust to changes in the perturbed feedback, although a drawback is that the warmings attributed to individual feedbacks do not sum up to the total amount of warming due to feedback interactions (as discussed in Sec. 2.4 below).

Feedback locking experiments in comprehensive climate models are computationally expensive, so previous studies have typically focused on locking a single feedback process. A moist energy balance model (MEBM), which approximates AHT as a diffusive process that involves both surface temperature and specific humidity, is more computationally efficient. Although idealized, MEBMs have been shown to capture the changes in temperature and AHT seen in comprehensive climate models (Bonan et al., 2018; Armour et al., 2019), and many studies have demonstrated that they can be a useful tool to assess the impact of individual radiative feedbacks on changes in temperature and AHT under global warming (Hwang and Frierson, 2010; Hwang et al., 2011; Rose et al., 2014; Roe et al., 2015; Bonan et al., 2018; Russotto and Biasutti, 2020).

In this study, we evaluate the contributions of each climate feedback to Arctic amplification

using a suite of feedback locking simulations with a MEBM, and we compare this with the results of a traditional feedback analysis. Determining how much each feedback contributes to Arctic amplification depends on how a feedback contribution is defined. We contrast the two methods and quantify how the warming anomaly associated with a given feedback causes further warming anomalies associated with each of the other feedbacks and AHT. These effects cause the difference between warming contributions in the traditional feedback analysis and the warming attributed to each feedback in the feedback locking analysis. We specify feedbacks from the Coupled Model Intercomparison Project phase 5 (CMIP5; Taylor et al., 2012), allowing a direct comparison with previous studies that used traditional feedback analyses (Pithan and Mauritsen, 2014; Goosse et al., 2018).

## 2.2 Attributing warming to individual feedbacks

We use an MEBM, which solves for the change in surface temperature under heating that includes both specified forcing and simulated changes in AHT. For the feedback locking analysis, we lock individual climate feedbacks in the MEBM, while allowing everything else to evolve. By taking the difference in surface warming between the simulation with all feedbacks active and the simulation with the individual feedback locked, we calculate the warming associated with the locked feedback. This approach accounts for feedback interactions in that the additional warming that arises when a feedback is included is modulated by the other feedbacks and AHT (see details in Sec. 2.4). We compare the warming calculated from the locking analysis to warming contributions from a traditional feedback analysis.

For both analyses, we use spatially-varying climate feedback parameter values diagnosed from CMIP5 global climate model (GCM) simulations (see appendix B for details regarding the calculation of feedback parameter values). Each climate feedback parameter has a meridional structure, $\lambda_i(\phi)$, where $\phi$ is the latitude. The sum of the individual feedbacks is the total feedback

parameter:

$$\lambda(\phi) = \lambda_0 + \sum_i \lambda_i(\phi), \tag{2.1}$$

where the Planck feedback has been divided into a global-mean value $\lambda_0$ and latitudinally-varying departures from this which is one of the terms $\lambda_i$, with $i$ is the index of the individual feedback. Note that when we refer to the index associated with a specific feedback, we will insert for $i$ an abbreviation for the name of the feedback rather than a number, e.g., $\lambda_{LR}$ for the lapse rate feedback parameter.

The TOA energy budget, which relates changes in surface temperature $T(\phi)$ to changes in heating $F(\phi)$, can be written as

$$0 = \lambda(\phi)T(\phi) + F(\phi). \tag{2.2}$$

The heating can be broken down into perturbations to the radiative forcing (e.g., from rising greenhouse gas concentrations) $F_{RAD}$, changes in ocean heat uptake and transport which is diagnosed as the anomalous net surface heat flux $F_{OHU}$, and changes in AHT convergence in the atmospheric column $F_{AHT}$:

$$F(\phi) = \underbrace{F_{RAD}(\phi)}_{\substack{\text{perturbation to} \\ \text{radiative forcing}}} + \underbrace{F_{OHU}(\phi)}_{\substack{\text{change in ocean} \\ \text{heat uptake}}} + \underbrace{F_{AHT}(\phi)}_{\substack{\text{change in atmospheric} \\ \text{heat transport}}} . \tag{2.3}$$

Values of $F_{RAD}$ and $F_{OHU}$ are diagnosed from CMIP5 (see appendix B) as functions of latitude, similar to the feedback parameters $\lambda_i$. The perturbations in surface temperature $T$ and AHT $F_{AHT}$ are computed with the MEBM. The computed $T$ and $F_{AHT}$ fields in the MEBM simulation with all feedbacks are used in the traditional feedback analysis.

### 2.2.1 Moist energy balance model (MEBM)

MEBMs are based on the dry energy balance model (EBM) framework (Budyko, 1969; Sellers, 1969) but add the latent heat effects of atmospheric moisture transport, which allows them to more accurately portray AHT (Hwang and Frierson, 2010). Here we use an MEBM that was developed and evaluated in previous studies (Roe et al., 2015; Siler et al., 2018; Bonan et al., 2018; Armour et al., 2019).

We use a perturbation form of the MEBM that solves for the climate response to a change in forcing, with the values of $\lambda_0$, $\lambda_i(\phi)$, $F_{RAD}(\phi)$, and $F_{OHU}(\phi)$ specified based on CMIP5 output. The MEBM approximates AHT as the diffusion of moist state energy (MSE) $h$, taking into account converging meridians on the Earth and using a constant diffusion coefficient $D = 2.61 \times 10^{-4}$ kg m$^{-2}$ s$^{-1}$ [consistent with the diffusivity value of $1.06 \times 10^6$ m$^2$ s$^{-1}$ used in Hwang and Frierson (2010)] to give the perturbation in AHT as

$$F_{AHT}(\phi) = D\frac{d}{dx}\left[(1-x^2)\frac{dh(\phi)}{dx}\right], \tag{2.4}$$

where $x \equiv \sin\phi$ and the MSE perturbation is

$$h(\phi) \equiv c_p T(\phi) + L_v q(\phi). \tag{2.5}$$

Here, $c_p = 1004$ J kg$^{-1}$ K$^{-1}$ is the specific heat of air and $L_v = 2.45 \times 10^6$ J kg$^{-1}$ is the latent heat of vaporization. The anomalous specific humidity $q$ is calculated using the Clausius-Clapeyron relation which approximately relates water vapor pressure to temperature:

$$q(\phi) = \frac{\epsilon r e_0}{p}\left\{\exp\left[\frac{a\,(T_0(\phi)+T(\phi))}{b+T_0(\phi)+T(\phi)}\right] - \exp\left[\frac{a\,T_0(\phi)}{b+T_0(\phi)}\right]\right\}, \tag{2.6}$$

where $\epsilon = 0.622$ is the moisture constant, $e_0 = 611.2$ Pa is the vapor pressure, $p = 9.8 \times 10^4$ Pa is the surface pressure, $a = 17.67$ and $b = 243.5$ K are the saturation vapor constants, and $T_0$ is

the mean state temperature expressed as the departure from 273.15 K which is estimated from ERA-Interim Reanalysis (Dee et al., 2011) as a function of latitude. As in previous studies, we keep the relative humidity fixed at a value of $r = 0.80$ in the calculation of MSE (e.g., Hwang and Frierson, 2010; Roe et al., 2015; Siler et al., 2018), so we are only including changes in specific humidity due to changes in temperature. This allows the MSE $h$ to be written as a function of only the surface temperature $T$ simulated in the MEBM and specified model parameters.

This MEBM configuration is adopted from Bonan et al. (2018), who found that the MEBM can account for 90% of the variance in surface temperature in the CMIP5 GCMs.

### 2.2.2 Traditional feedback analysis

We begin by considering a traditional analysis of the warming contributions associated with the regional structure of feedbacks. First, Eqs. 2.1-2.2 are rearranged as

$$T(\phi) = \frac{F(\phi)}{-\lambda_0} + \sum_i \lambda_i(\phi) \frac{T(\phi)}{-\lambda_0}. \tag{2.7}$$

Eq. 2.7 is illustrated schematically in Fig. 2.6 in appendix A. The first term represents warming in the absence of any feedbacks, and it can be readily split into warming contributions from $F_{RAD}$, $F_{OHU}$, and $F_{AHT}$. The second term represents the sum of the warming contributions from each feedback $T_{i*}$, which are defined as

$$T_{i*}(\phi) \equiv \lambda_i(\phi) \frac{T(\phi)}{-\lambda_0}. \tag{2.8}$$

The feedback parameters and warming contributions based on this traditional feedback analysis are plotted in Fig. 2.1a,b,c,d.

### 2.2.3 Feedback locking analysis

To examine the amount of warming that would occur in the absence of a given feedback process, we run a simulation with the MEBM in which an individual feedback parameter field

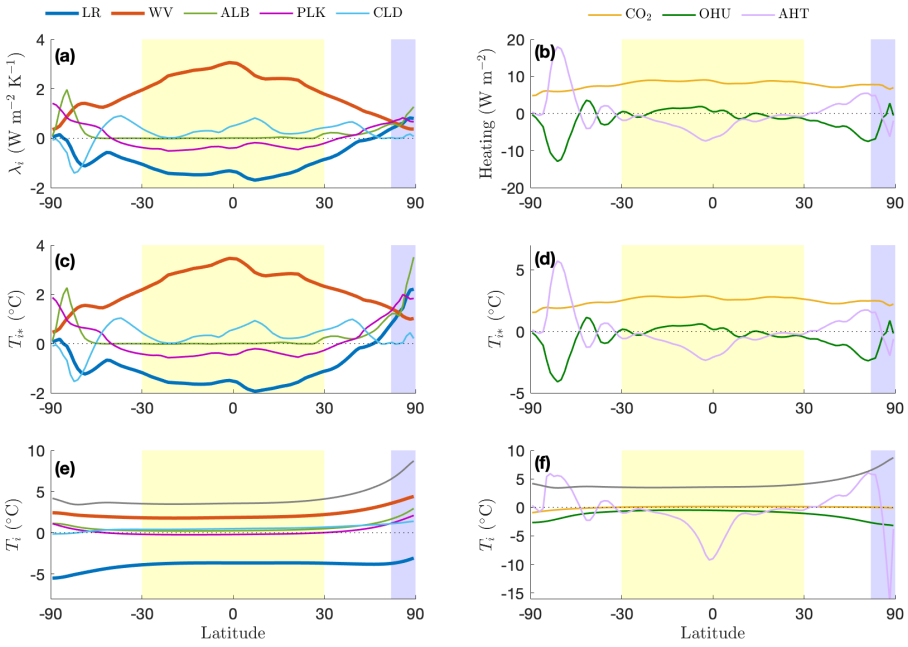


**Figure 2.1.** Latitudinally-varying variables as calculated from CMIP5 simulations and MEBM simulations. Top panel: feedbacks and heating terms diagnosed from CMIP5 simulations. (a) Feedback parameters ($\lambda_i$) for each radiative feedback process: lapse rate (LR), water vapor (WV), surface albedo (ALB), Planck deviation from global-mean value (PLK), and cloud (CLD). (b) Heating terms: $CO_2$ forcing ($CO_2$), changes in ocean heat uptake (OHU), and changes in atmospheric heat transport (AHT). Middle Panel: warming contributions from each feedback process based on a traditional feedback analysis ($T_{i*}$). (c) Warming contributions for each feedback which is proportional to the product of the feedback parameter (panel a) and the total temperature change. (d) Warming contributions for each heating term which is proportional to the heating term (panel b). Bottom panel: results of the feedback locking analysis ($T_i$). (e) Warming for each radiative feedback. (f) Warming for each heating term: deviation from global mean $CO_2$ forcing ($CO_2$), changes in ocean heat uptake (OHU), and changes in atmospheric heat transport (AHT). In all panels, yellow and blue shading represent the tropical and Arctic regions, respectively. This study focuses on the LR and WV feedbacks, which are indicated by thicker lines in panels (a), (c), and (e). The horizontal axes are scaled to be uniform in $x \equiv \sin(\text{latitude})$; note that each increment of $x$ is proportional to the surface area of the associated latitude band.

is subtracted from the total feedback parameter. Since the MEBM we are using is a model of anomalies from the reference climate, turning off a specific feedback is equivalent to keeping the climate fields associated with the feedback locked at the climatological state. Hence, we refer to this approach as "feedback locking", a term used to describe similar experiments in previous studies (e.g., Graversen and Wang, 2009; Langen et al., 2012; Middlemas et al., 2020). Note

that these types of experiments are sometimes described in the literature with other terminology, including "suppressing" feedbacks or "turning off" feedbacks. An example of feedback locking is fixing the surface albedo at its climatological value. This form of feedback locking has been used in previous studies to look at effects of the surface albedo feedback on local and nonlocal warming, global and polar warming, and internal variability (Cess et al., 1991; Hall, 2004; Graversen and Wang, 2009; Roe et al., 2015).

In the MEBM, a feedback is locked by replacing $\lambda(\phi)$ with $\lambda(\phi) - \lambda_i(\phi)$. We refer to the resulting warming simulated by the MEBM as $T_{-i}$. Since the different temperature perturbation causes a different simulated $F_{AHT}$, we refer to the resulting heating as $F_{-i}$. We can then write the perturbation equation for the MEBM (Eq. 2.2) when a feedback is locked as:

$$0 = [\lambda(\phi) - \lambda_i(\phi)]T_{-i}(\phi) + F_{-i}(\phi). \tag{2.9}$$

We calculate the warming attributed to each feedback process in this approach $T_i$ as the difference between the result with all feedbacks active $T$ and the result with the individual feedback locked $T_{-i}$:

$$T_i(\phi) \equiv T(\phi) - T_{-i}(\phi). \tag{2.10}$$

For the warming associated with the latitudinal variations in the $CO_2$ forcing, in the locked simulation we set $F_{RAD}$ to its global-mean value, and we set $F_{OHU} = 0$ or $F_{AHT} = 0$ in the locked simulations for the warming associated with changes in ocean heat uptake or changes in AHT. The warming attributed to each feedback and to each heating term using feedback locking in the MEBM is shown in Fig. 2.1e,f.

## 2.3 Lapse Rate and Water Vapor Feedbacks

In both the feedback locking analysis and the traditional feedback analysis, we average the warming associated with each feedback over the Arctic region (60°N to 90°N) and the tropical

region (30°S to 30°N) in order to quantify the contributions to Arctic amplification (Fig. 2.2). The results show striking differences between the two approaches, especially for the water vapor and lapse rate feedbacks, which we focus on for the remainder of this study. The water vapor feedback is the largest factor opposing Arctic amplification in the traditional feedback analysis, i.e., it is the point farthest in the downward right direction from the dashed line in Fig. 2.2a. In the feedback locking analysis, by contrast, it is the largest contributor to Arctic amplification (the point farthest in the upward left direction from the dashed line in Fig. 2.2b). The lapse rate feedback is the largest contributor to Arctic amplification in the traditional feedback analysis (Fig. 2.2a), warming the Arctic while cooling the tropics. By contrast, it has an approximately neutral effect in the feedback locking analysis (Fig. 2.2b), because it cools the tropics and the Arctic by similar amounts.

These differences between the results of the two analyses in Fig. 2.2 highlight the importance for each feedback process of interactions with other feedback processes and with the meridional energy transport. The water vapor feedback parameter is positive everywhere, but it is considerably larger in the tropical region than in the Arctic (Fig. 2.1a). Warming contributions in the traditional feedback analysis scale as the feedback parameter (Fig. 2.1a) times the total warming (grey line in Fig. 2.1e,f). Although the warming is greater in the Arctic than in the tropics, this difference is not sufficient to overcome the difference in the feedback parameter, and the result is that the warming contribution from water vapor is larger in the tropics than in the Arctic (Figs. 2.1c and 2.2a).

However, things change when the climate system is allowed to respond to the omission of the water vapor feedback. Removing the concentrated warming in the tropical region caused by the water vapor feedback leads to a decrease in the temperature gradient between the equator and the pole, and hence a decrease in the meridional transport of MSE in the MEBM. This is most evident in Fig. 2.3a in the equatorial region, where there is increased heating by AHT when the water vapor feedback is suppressed. A smaller level of decreased heating in the polar region can also be seen in Fig. 2.3a. In other words, the inclusion of the water vapor feedback causes AHT

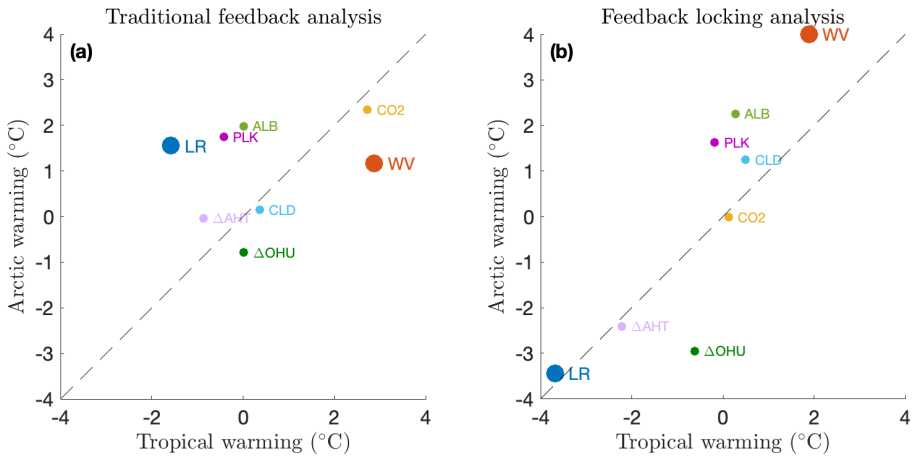


**Figure 2.2.** Contributions of each feedback process and heating term to Arctic amplification, plotted as Arctic warming vs tropical warming. (a) Warming contributions calculated using a traditional feedback analysis (Eq. 2.7), as used in previous studies. (b) Results of the feedback locking analysis (Eq. 2.10), which is suggested here to be a physically intuitive approach. Here the lapse rate feedback (LR), water vapor feedback (WV), surface albedo feedback (ALB), Planck feedback deviation from the global-mean value (PLK), cloud feedbacks (CLD), $CO_2$ forcing (CO2), changes in ocean heat uptake (ΔOHU), and changes in atmospheric heat transport (ΔAHT) are plotted. Note that in the traditional feedback analysis, $CO_2$ forcing includes both the global mean and the spatially-varied deviation, whereas in the feedback locking analysis, $CO_2$ forcing is taken as the deviation from the global-mean value. Tropical warming is averaged over 30°S–30°N, and Arctic warming is averaged over 60°N–90°N. The LR and WV feedbacks, which are the focus of this study, are indicated by larger circles.

to cool the tropics and warm the Arctic.

There are also interactions between the water vapor feedback and other feedbacks in the MEBM, i.e., other feedbacks react to the change in warming due to the inclusion or omission of the water vapor feedback. When the water vapor feedback is locked, the total feedback felt by the model ($\lambda - \lambda_{WV}$) is less negative in the Arctic region than in the tropical region (Fig. 2.3b). Therefore, because water vapor is a positive feedback, it can interact with and enhance the warming from other positive feedbacks in the Arctic, such as the SAF.

The result of this is that the warming in the MEBM when the water vapor feedback is locked has a pattern similar to when all feedbacks are included (orange and blue line in Fig. 2.3c). A similar point was noted in Langen et al. (2012), who found that when they locked the water

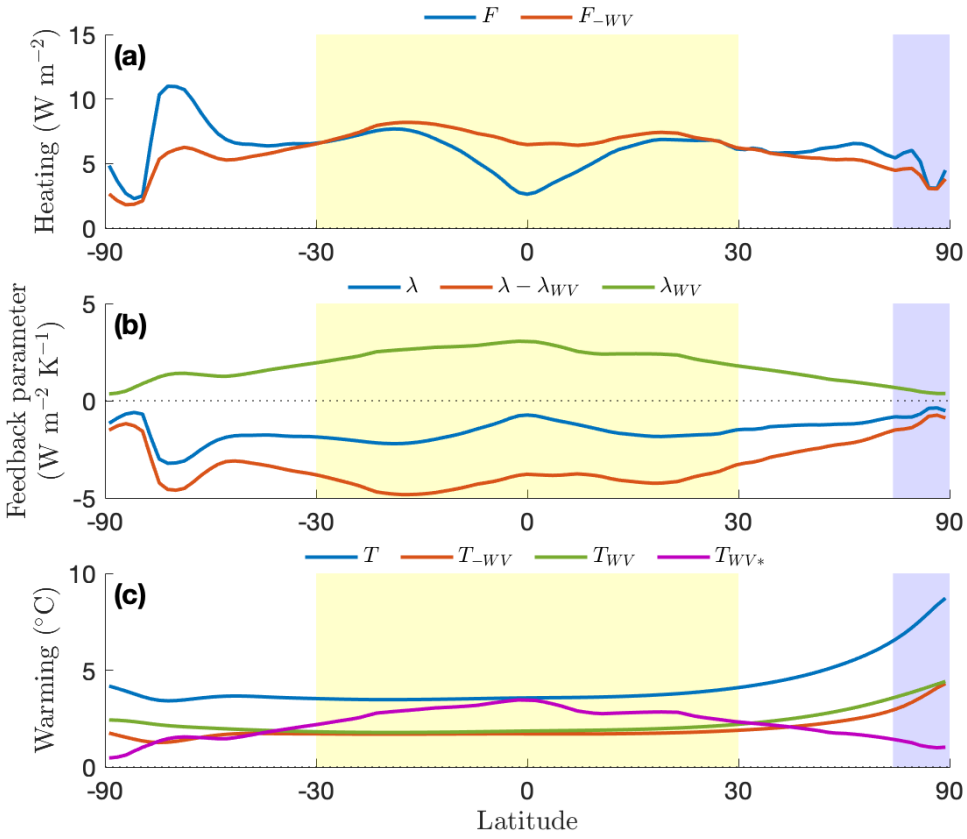


**Figure 2.3.** Feedback locking analysis results for the water vapor feedback. (a) Heating (Eq. 2.3) in the MEBM simulation with all feedbacks active ($F$) and in the MEBM simulation with the water vapor feedback locked ($F_{-WV}$). Note that all changes in heating are due to changes in AHT, since the perturbation to radiative forcing ($F_{RAD}$) and ocean heat uptake ($F_{OHU}$) are specified in the MEBM. (b) Total feedback parameter ($\lambda$) and the feedback parameter when the water vapor feedback is locked ($\lambda - \lambda_{WV}$), with the difference between the two ($\lambda_{WV}$) also indicated. (c) Surface temperature change simulated in the MEBM with all feedbacks ($T$) and with the water vapor feedback locked ($T_{-WV}$), the warming due to the water vapor feedback based on the feedback locking analysis ($T_{WV} \equiv T - T_{-WV}$), and the warming contribution of the water vapor feedback based on the traditional feedback analysis ($T_{WV*} = T\lambda_{WV}/-\lambda_0$). Note that the green and purple curve in panel (c) are equivalent to the red curve in Fig. 2.1e and 2.1c respectively.

vapor feedback in a GCM with doubled $CO_2$, it produced a pattern of warming that was similar to when the WV feedback was included, but with about half the amplitude. In other words, they found that the WV feedback causes an approximately spatially-uniform doubling of the surface temperature response to radiative forcing. Using the MEBM with forcing and feedback fields from individual CMIP5 models, we find that this spatially-uniform doubling is a largely robust

response among the climate models (Fig. 2.7 in appendix C).

Next we turn to the lapse rate feedback. In contrast to the water vapor feedback which is positive everywhere, the lapse rate feedback parameter is negative in the tropical region and positive in the Arctic region (Fig. 2.1a). This causes the lapse rate feedback to have a large contribution to Arctic amplification in the traditional feedback analysis (Figs. 2.1c and 2.2a).

An implication of this for the feedback locking analysis is that the presence of the lapse rate feedback decreases the temperature gradient between the equator and the pole. So when the feedback is locked, the meridional temperature gradient increases, leading to additional transport of MSE into the Arctic. (Note that even under uniform warming there would be a relatively small increase in the transport of MSE into the Arctic due to the Clausius-Clapeyron relation (Merlis and Henry, 2018).) This can be seen in Fig. 2.4a: the inclusion of the lapse rate feedback (going from the red line to the blue line) causes warming in the tropics and cooling in the Arctic due to AHT changes. Hence the AHT changes decrease the level of Arctic amplification, opposing the local feedback effects.

Furthermore, because the lapse rate feedback decreases the level of warming into the tropics, it dampens the effect of other positive feedbacks there, leading to further tropical cooling. Taken together, we find that these effects cause the lapse rate feedback to contribute similar levels of cooling in the tropical and Arctic regions (Figs. 2.4c and 2.2b).

The other radiative feedbacks show less dramatic differences between the traditional feedback analysis and the feedback locking analysis (Fig. 2.2). The differences may be less pronounced because the feedback parameters for the SAF, Planck feedback departure from global mean, and cloud feedbacks do not have such large latitudinal variations between the equator and pole (Fig. 2.1a). Notably, the surface albedo feedback and Planck feedback anomaly contribute substantially to Arctic amplification in both methods. In other words, they contribute more to Arctic warming than tropical warming due to the feedback pattern alone, and similarly when interactions with other feedbacks and with AHT are included.

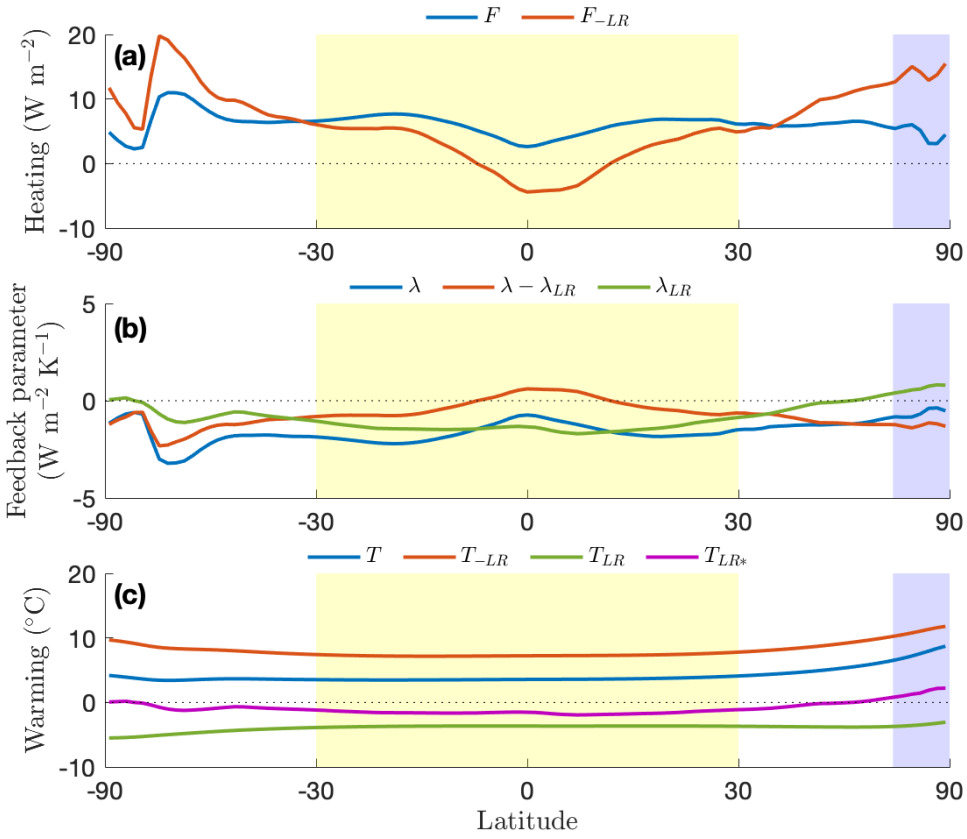


**Figure 2.4.** As in Fig. 2.3, but for the lapse rate feedback. Note that the green and purple curve in panel (c) are equivalent to the blue curve in Fig. 2.1e and 2.1c respectively.

## 2.4 Decomposition of warming in the feedback locking analysis

The MEBM in Eq. 2.2 represents an ordinary differential equation for $T(\phi)$ that is nonlinear due to the inclusion of $q$ in $F_{AHT}$. In the traditional feedback analysis, $F_{AHT}$ is a specified field, so in that case this becomes a linear ordinary differential equation for $T(\phi)$. However, whether or not the terms in Eq. 2.2 depend linearly on $T$, there is a nonlinear dependence on $\lambda$ in the solution for $T$ (as discussed in Roe and Baker, 2007). Therefore interactions between feedbacks can arise when the inclusion of a feedback changes the total warming $T$ and this, in turn, changes the warming produced by other feedbacks. Since $F_{AHT}$ is computed using the

MEBM in each feedback locking simulation, there are also interactions between each feedback and the AHT, in that the AHT adjusts to regional changes in warming induced by each feedback.

Hence the warming attributed to a given feedback process in the feedback locking analysis can be thought of as comprising three separate components: (i) the warming due to the feedback in isolation which is equivalent to the result of the traditional feedback analysis, (ii) the warming due to interactions between the feedback and other climate feedbacks, and (iii) the warming due to interactions between the feedback and AHT. The contributions of these three terms can be identified by subtracting the equation for the MEBM with a feedback locked (2.9) from the equation for the full MEBM (2.2):

$$0 = \lambda T - (\lambda - \lambda_i)T_{-i} + F - F_{-i}, \tag{2.11}$$

where we have omitted the coordinate $\phi$ for brevity. Rewriting the total feedback parameter given by Eq. (2.1) as $\lambda = \lambda_0 + \lambda_i + \sum_{j\neq i}\lambda_j$ and using the definition of $T_i$ in Eq. (2.10), this can be rewritten as

$$0 = \lambda_0 T_i + \lambda_i T + \sum_{j\neq i}\lambda_j T_i + F - F_{-i}, \tag{2.12}$$

which can be rearranged to give:

$$T_i = \underbrace{T_{i*}}_{\substack{\text{individual warming}\\ \text{contribution}}} + \underbrace{\frac{\sum_{j\neq i}\lambda_j T_i}{-\lambda_0}}_{\substack{\text{feedback}\\ \text{interactions}}} + \underbrace{\frac{F - F_{-i}}{-\lambda_0}}_{\substack{\text{AHT}\\ \text{interactions}}}. \tag{2.13}$$

The left-hand side of Eq. 2.13 is the warming from a feedback process in the feedback locking analysis, and the first term on the right-hand side is the warming contribution from the traditional feedback analysis (Eq. 2.8). The results of the two analyses differ due to the other two terms: the second term on the right-hand side is the product of all other feedback parameters and the warming associated with the inclusion of feedback $i$ (normalized by $-\lambda_0$), and the third term arises from changes in AHT (since $F$ and $F_{-i}$ differ only in their values of $F_{AHT}$). The values of

each of the terms in Eq. (2.13) for simulations in which each feedback is locked are shown in Fig. 2.5.

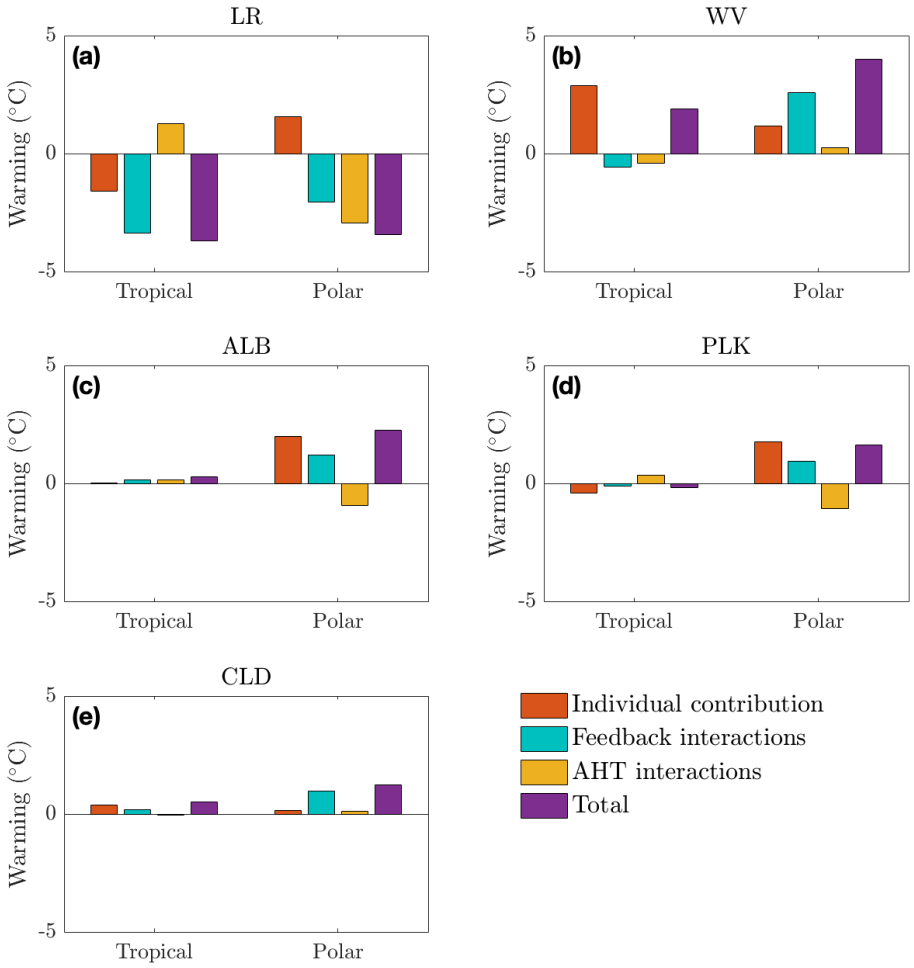


**Figure 2.5.** Decomposition of simulated warming attributed to each feedback using locking simulations (Total) into contributions from the individual contribution of the feedback alone (equivalent to the result from the traditional feedback analysis), interactions with other feedbacks, and interactions with AHT, as described in Eq. 2.13. Tropical (30°S–30°N) and polar (60°N–90°N) values are shown for the warming attributed to the lapse rate feedback (LR), water vapor feedback (WV), surface albedo feedback (ALB), Planck feedback departure from global-mean value (PLK), and cloud feedbacks (CLD).

Decomposing the warming due to the water vapor feedback, we find that the interaction between the water vapor feedback and other positive feedbacks in the Arctic is the largest factor

contributing to why the water vapor feedback warms the Arctic more than the tropics in the feedback locking analysis, with changes in AHT having a smaller effect (Fig. 2.5b). For the lapse rate feedback, we find that interactions with other feedbacks leads to cooling in the Arctic that is nearly as large as the tropical cooling from interactions with other feedbacks (Fig. 2.5a); alongside the changes in AHT, these lead the lapse rate feedback to have a large cooling effect in both regions.

The decomposition of the simulated warming in Fig. 2.5c,d,e also shows that the contributions from changes in AHT and interactions with the other feedbacks are smaller for the warming associated with other feedbacks (surface albedo feedback, deviation from global mean Planck feedback, and cloud feedbacks).

This decomposition illustrates some of the trade-offs between the feedback locking analysis and the traditional feedback analysis. In the traditional feedback analysis, interactions between feedbacks and with AHT, although included, are not easily interpreted, as they are split up among the warming contribution terms. For example, the total warming from feedback interactions that arise from the inclusion of the SAF will not all be included in the SAF warming contribution term using this decomposition (see Eq. 2.8). However, in the traditional feedback analysis the sum of each warming contribution is equal to the total warming, whereas this is not the case when one sums up each of the warming terms found using the feedback locking analysis.

## 2.5 Discussion

### 2.5.1 Changes in global-mean surface temperature

Using a traditional feedback analysis to attribute contributions to Arctic amplification is an expansion of the standard climate feedback approach which analyzes the global-mean surface temperature response to a perturbation in the global-mean TOA radiation. However, unlike for the traditional feedback analysis of contributions to Arctic amplification, we find that the global-mean results of a traditional climate feedback analysis and the global-mean results of a

feedback locking analysis with the MEBM are monotonically related (Fig. 2.8 in appendix D). The relationship between the results from the two types of analysis is not linear due to feedback interactions, but we find that a feedback locking analysis consistently attributes more warming to feedbacks with larger global parameter values. Hence the results of this study should not be seen as at odds with traditional climate feedback analyses that use global-mean feedback parameter values.

### 2.5.2 Comparison with previous studies

Some previous studies have combined the lapse rate feedback with the water vapor feedback when considering their contributions to warming, motivated by the close physical connection between these feedbacks and their compensatory effects in the tropics. This has been found to diminish the differences in global feedback values diagnosed from different comprehensive climate models (e.g., Soden and Held, 2006). An alternative decomposition that can reduce the cancellation between these two feedbacks, as well as the Planck feedback, is to hold the relative humidity fixed in the calculation of the lapse rate and Planck feedbacks and account for changes in relative humidity in a humidity feedback term (Held and Shell, 2012; Zelinka et al., 2020; Jeevanjee et al., 2021), rather than the traditional approach in which specific humidity is held fixed in the calculation of the lapse rate and Planck feedbacks and changes in specific humidity are accounted for in the water vapor feedback. It has also been suggested that partitioning the lapse rate feedback into upper and lower atmosphere contributions allows the roles of local and remote driving mechanisms to be more transparently identified (Feldl et al., 2020). Here we instead adopt the classical separation between the lapse rate and water vapor feedbacks because this allows a more direct comparison with previous traditional feedback analyses which also adopted this separation. A message of this study, however, is that the quantification of feedback contributions depends on how feedbacks and contributions are defined, and this needs to be taken into account when comparing studies.

One such previous study is that of Russotto and Biasutti (2020), who used a feedback

locking approach in order to investigate how feedbacks contribute to Arctic amplification in a set of idealized slab ocean aquaplanet GCM simulations that did not include sea ice. They found the water vapor feedback to have a positive contribution to Arctic amplification, similar to the present study, but their simulations omitted the SAF, which is a large positive feedback in the Arctic and has substantial interactions with the water vapor feedback in the results presented here.

Note that instead of using the feedback locking approach which compares simulations using $\lambda$ and $\lambda - \lambda_i$, an alternative "feedback activation" approach would evaluate the change in temperature response due to activating only a single feedback in a base state with no other feedbacks included (comparing $\lambda_0 + \lambda_i$ with $\lambda_0$). Langen et al. (2012) investigated warming due to the water vapor feedback and cloud feedbacks by locking either one or both feedbacks, which allowed them to dissect the primary warming due to the feedback and secondary warming due to the feedback interactions. In the present study, we adopt the feedback locking approach because we see it as more physically intuitive in that it compares a physically perturbed climate system with the actual climate system. The feedback activation approach does not account for interactions between feedbacks, and neither of the two temperature responses that are compared represents the climate in the presence of all feedbacks.

### 2.5.3 Limitations of the feedback locking analysis

One of the limitations of feedback locking analyses is that the results depend on which other feedbacks and energy transports are included in the model. Consequently, the temperature changes in the MEBM feedback locking simulations are expected to differ somewhat from feedback locking simulations carried out with a comprehensive GCM, which represents more processes and does not have constant feedback parameters. In the MEBM simulations presented here, by contrast, each feedback parameter [$\lambda_i(\phi)$] remains unchanged when other feedbacks are locked. Although this is expected to be a source of inaccuracy, it has been shown previously that it is a relatively accurate approximation to treat feedback patterns as time invariant over climates ranging from pre-industrial to doubled $CO_2$ (Armour et al., 2013).

Another caveat is that the feedback locking analysis and traditional feedback analysis both approximate the warming by feedbacks to be linearly proportional to the surface temperature change, with variations in the vertical structure of warming captured in the lapse rate feedback. However, it is known that certain feedbacks and heating terms have vertical structures that have implications for Arctic amplification. For example, the water vapor feedback primarily warms the surface in the Arctic, as does the surface albedo feedback (e.g., Screen and Simmonds, 2010; Henry et al., 2021). In contrast, poleward heat transport into the Arctic tends to warm the mid-troposphere (e.g., Graversen et al., 2008). This could be addressed in further work that uses the feedback locking approach adopted here with a model that more directly accounts for vertical variations. For example, Cai (2006) used a 4-box formulation to investigate the changes in the meridional temperature gradient in the atmosphere, and Henry et al. (2021) used a single-column model to study polar amplification. The latter study found that the water vapor feedback has a positive contribution to Arctic amplification due to the warming maximum associated with the water vapor feedback being near the surface in high latitudes but in the upper troposphere in low latitudes. This suggests that adding a representation of vertical variations to the present analysis could plausibly enhance the result that the water vapor feedback contributes to Arctic amplification. On the other hand, Henry and Merlis (2019) found that when linearizing the Stefan-Boltzmann law, polar amplification from the Planck feedback reduced as expected, but this was compensated by an increase in polar amplification from the lapse rate feedback due to the non-linearity of the Stefan-Boltzmann law changing the vertical structure of warming. Another approach that accounts for vertical variations in the temperature response is the climate feedback response analysis method (CFRAM Lu and Cai, 2009; Cai and Lu, 2009), which extends the traditional feedback analysis framework to show the 3D warming contribution fields associated with each feedback.

### 2.5.4 Arctic amplification definition

It should be noted that these results depend both on how Arctic amplification is defined and how the separate feedbacks are defined. In this study, we keep the same definition of feedbacks and Arctic amplification for both methods. We define Arctic amplification as the difference in warming between the Arctic and tropical regions depicted in Fig. 2.2, which has similarly been used in previous studies (e.g., Pithan and Mauritsen, 2014; Goosse et al., 2018; Stuecker et al., 2018). This differs from instead defining Arctic amplification as the Arctic warming divided by the tropical (or global-mean) warming, as adopted in some other studies (e.g., Holland and Bitz, 2003; Hwang et al., 2011; Langen et al., 2012). When calculating the level of Arctic amplification using the latter definition, cooling both regions equally has a larger positive effect on Arctic amplification than warming both regions equally, and we find that based on the feedback locking analysis the lapse rate feedback makes a substantial contribution to the ratio definition of Arctic amplification.

## 2.6 Summary

Previous studies have used traditional feedback analyses to investigate the contribution of each climate feedback process to the Arctic amplification of global warming. Here we instead adopted a feedback locking approach, in which the warming is computed with an MEBM when each feedback process is turned off. Traditional feedback analyses do not account for each feedback's interactions with the other feedbacks and with AHT, whereas feedback locking analyses do account for this these interactions. Feedback locking analyses are also arguably more physically intuitive, in that they assess how much warming would occur in the absence of a given climate feedback process. We find that adopting a feedback locking approach substantially changes the warming attributed to each feedback process.

Specifically, we find that the water vapor feedback is the primary factor contributing to Arctic amplification according to the feedback locking analysis, which is largely due to the

water vapor feedback amplifying other positive feedbacks in the Arctic. This is in contrast with previous studies that found the water vapor feedback to be the primary factor opposing Arctic amplification based on traditional feedback analyses. Additionally, we find that the lapse rate feedback has an approximately equivalent contribution to surface cooling in the tropical and Arctic regions in a feedback locking analysis, whereas previous studies found it to be the main driver of Arctic amplification according to traditional feedback analyses. This suggests, for example, that an idealized model that omits a representation of the water vapor feedback would do a worse job of capturing Arctic Amplification than an idealized model that omits a representation of the lapse rate feedback, in contrast with expectations from previous studies that relied on traditional feedback analyses. Overall, these results highlight that determining which feedbacks are most important for Arctic amplification depends crucially on what approach is used to determine the contribution of each feedback process.

## 2.7 Acknowledgments

Many thanks to Kyle Armour for providing the MEBM code, Dave Bonan for helping with the model code and for comments on the manuscript, Tim Merlis for comments on the manuscript and for suggestions that led to the analysis in Fig. 2.7, and Isaac Held and Nadir Jeevanjee for helpful discussions and comments on the manuscript. This work was supported by National Science Foundation Grant OPP-1643445. The CMIP5 data used in this study is accessible at the Earth System Grid Federation (ESGF) Portal (https://esgf-node.llnl.gov/search/cmip5/).

Chapter 2, in full, is a reprint of the material as it appears in Journal of Climate, 2022. Beer, E., and I. Eisenman, 2022: Revisiting the role of the water vapor and lapse rate feedbacks in the Arctic amplification of climate change. *Journal of Climate*, **35(10)**, 2975-2988. The dissertation author was the primary investigator and author of this paper.

## 2.8 Appendix A: Traditional climate feedback analysis framework

The standard framework for analyzing climate feedbacks is illustrated in Fig. 2.6, using a schematic analogy to an electrical circuit. A perturbation to the forcing ($F$) is sent through a reference system, which is taken here as the negative inverse of the global-mean Planck feedback parameter ($\lambda_0$ which is typically in units of W m$^{-2}$ K$^{-1}$) resulting in a change in surface temperature ($T$) to maintain radiative balance. A feedback is incorporated into the system by taking the response at the "pick off point" and sending it through an additional perturbation to the radiative forcing due to the feedback ($\lambda_i$) and then bringing it to the "summing point". The total perturbation to the radiative forcing is then sent through the reference system.

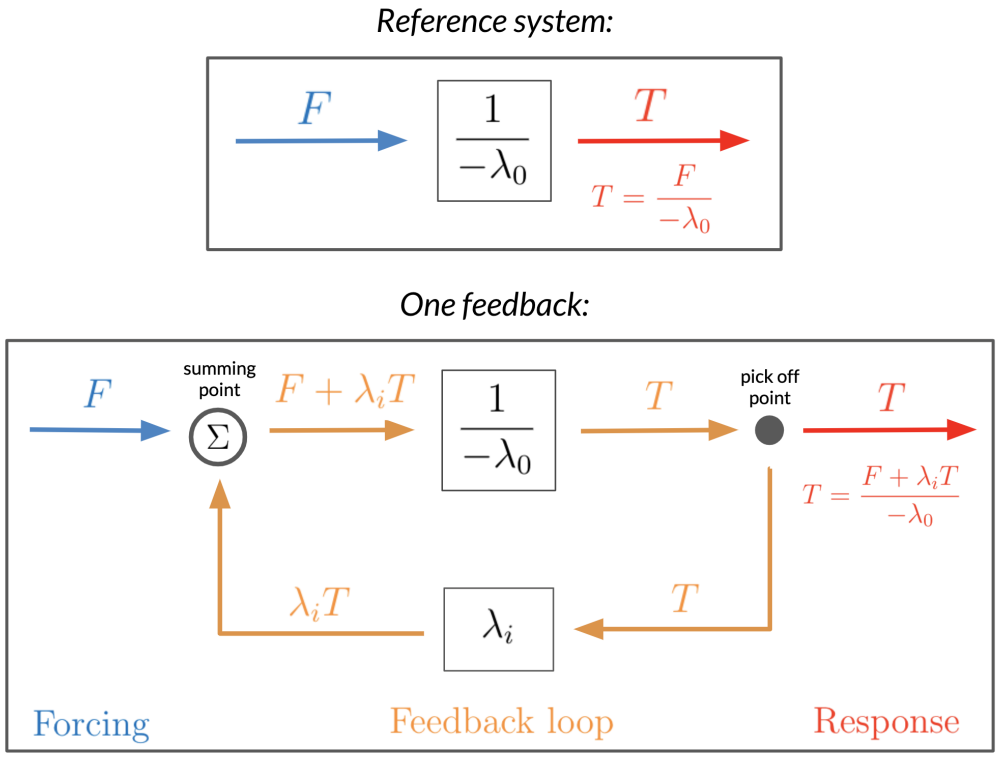


**Figure 2.6.** Schematic of the standard framework for analyzing climate feedbacks, using the analogy to an electrical circuit (based on Roe, 2009; Goosse et al., 2018). (top) Reference system. (bottom) System that includes one feedback.

## 2.9 Appendix B: Spatially-varying fields in the MEBM

The MEBM parameters for spatially-varying feedbacks and heating fields are taken from CMIP5 output, as described by Bonan et al. (2018) and briefly summarized here (Table 2.1). Zonal-mean TOA budget analyses are used to calculate $F_{RAD}$, $F_{OHU}$, and $\lambda$: $F_{RAD}$ is calculated as the change in TOA radiation in fixed sea surface temperature simulations under $CO_2$ quadrupling, $F_{OHU}$ is calculated as the change in net surface heat flux in CMIP5 coupled GCM abrupt $CO_2$ quadrupling simulations averaged over years 85-115, and $\lambda$ is calculated by equating the TOA net radiation anomaly with $\lambda T + F_{RAD}$ in the same CMIP5 coupled GCM output. Radiative kernels are used to partition $\lambda$ into individual feedbacks parameters $\lambda_i$; note that the radiative kernel analysis uses a somewhat different set of CMIP5 GCMs than the TOA budget analysis, as described by Bonan et al. (2018) (Table 1 of their supporting information; with the exception that models FGOALS-S2 and HADGEM2-ES are not used in our calculations of $F_{RAD}$, $F_{OHU}$, and $\lambda$). Throughout the analysis, we use values of $F_{AHT}$ and $T$ that are simulated by the MEBM.

**Table 2.1.** Sources of parameters and variables.

| Variable | Output from MEBM | Calculated using TOA budget analysis | Calculated using radiative kernels |
|---|---|---|---|
| $F_{RAD}$ | | × | |
| $F_{OHU}$ | | × | |
| $\lambda$ | | × | |
| $\lambda_i$ | | | × |
| $F_{AHT}$ | × | | |
| $T$ | × | | |

## 2.10 Appendix C: Comparing the local climate sensitivity of the water vapor feedback in individual models

The water vapor feedback approximately doubles the climate sensitivity at each location, meaning that the warming field in the MEBM without the water vapor feedback is approximately

equal to the warming field in the MEBM with all feedbacks scaled by one half. This is shown for individual CMIP5 models in Fig. 2.7.

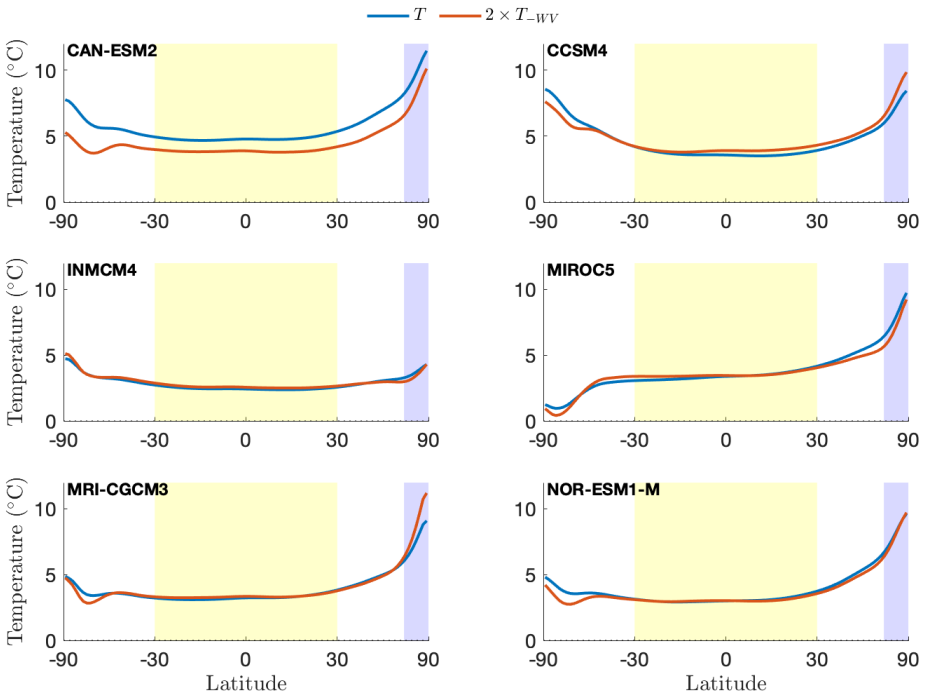


**Figure 2.7.** Water vapor feedback climate sensitivity in individual CMIP5 models. Change in surface temperature in the MEBM with all feedbacks (blue) and twice the change in surface temperature with the water vapor feedback locked (orange) for six CMIP5 models (name in bold). The similarity of the blue and orange lines suggest that water vapor approximately doubles climate sensitivity.

## 2.11 Appendix D: Traditional feedback analysis versus feedback locking for global-mean temperature changes

The traditional feedback analysis is based on analyses used to look at the contributions from individual feedbacks to global-mean surface temperature changes. Here we compare the warming contributions from a feedback analysis with the results of feedback locking for the global-mean temperature. Beginning with the former, the global average of Eq. 2.2 is

$$0 = \langle \lambda T \rangle + \langle F \rangle. \tag{2.14}$$

where $\langle\,\rangle$ indicates the global-mean value. We define the global feedback parameter value $\lambda_i^G$ of each individual feedback as

$$\lambda_i^G \equiv \frac{\langle \lambda_i T \rangle}{\langle T \rangle}. \tag{2.15}$$

Inserting Eq. 2.1 into Eq. 2.14 and rearranging gives

$$\langle T \rangle = \frac{\langle F \rangle}{-\lambda_0} + \sum_i \lambda_i^G \frac{\langle T \rangle}{-\lambda_0}, \tag{2.16}$$

which is the global-mean equivalent of Eq. 2.7, with the warming contributions from each feedback given here as

$$\langle T_{i*} \rangle \equiv \lambda_i^G \frac{\langle T \rangle}{-\lambda_0}. \tag{2.17}$$

Hence since $\lambda_0$ and $\langle T \rangle$ are globally constant, the global warming contribution for each feedback scales with the global feedback parameter value $\lambda_i^G$. We can compare this with the global-mean warming calculated from the locking simulations in the MEBM, given by the global-mean equivalent of Eq. 2.10, which is $\langle T_i \rangle \equiv \langle T \rangle - \langle T_{-i} \rangle$. The levels of warming attributed to each feedback using the two approaches are plotted in Fig. 2.8.

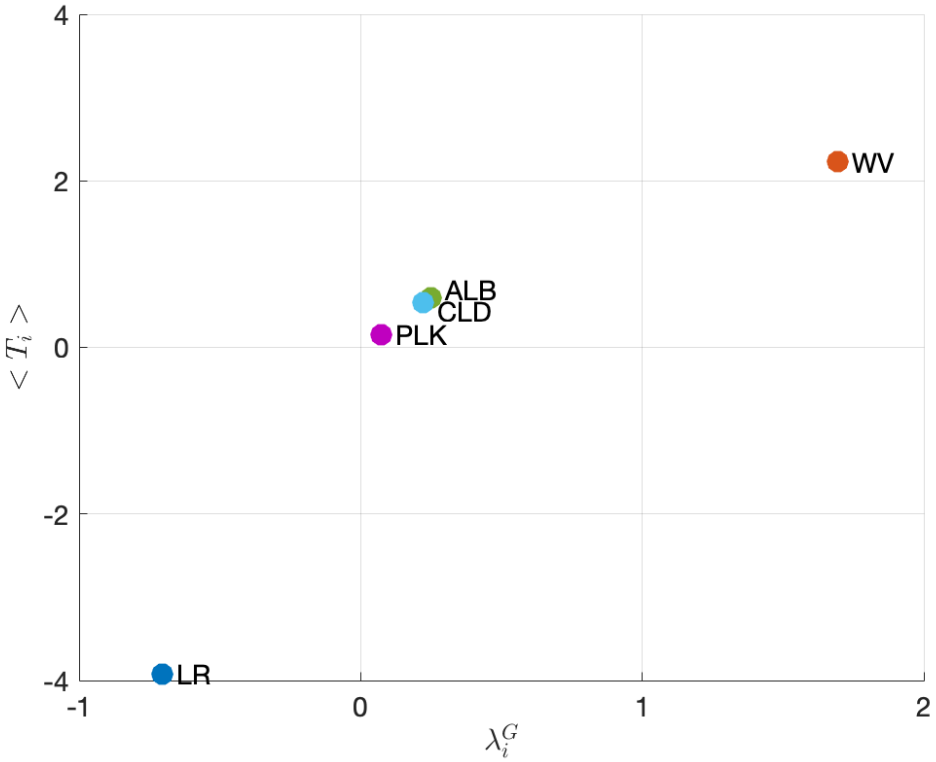


**Figure 2.8.** Global-mean surface warming calculated from locking simulations compared with the global feedback parameter ($\lambda_i^G$) for each radiative feedback. Feedbacks are labeled as in Fig. 2.5. In this global-mean analysis, the contribution of each feedback using locking simulations in the MEBM scales monotonically with the global feedback parameter.

# Chapter 3

# Polar amplification due to enhanced heat flux across the halocline

**Abstract**

Polar amplification is a widely discussed phenomenon, and a range of mechanisms have been proposed to contribute to it, many of which involve atmospheric and surface processes. However, substantial questions remain regarding the role of ocean heat transport. Previous studies have found that ocean heat transport into the Arctic increases under global warming, but the reasons behind this remain unresolved. Here, we investigate changes in oceanic heat fluxes and associated impacts on polar amplification using an idealized ocean–sea ice–climate model of the Northern Hemisphere. We show that beneath the sea ice, vertical temperature gradients across the halocline increase as the ocean warms, since the surface mixed layer temperatures in ice-covered regions are fixed near the freezing point. These enhanced vertical temperature gradients drive enhanced horizontal heat transport into the polar region and can contribute substantially to polar amplification.

## 3.1 Introduction

Polar amplification is a robust feature of both observations and model projections in the Arctic region and of equilibrium global warming simulations in the Antarctic region (Serreze et al., 2000; Collins et al., 2013; Holland and Bitz, 2003). However, there is still substantial

variability in the magnitude of polar amplification across models, and previous studies have proposed a range of different mechanisms as the main driver (Flato et al., 2013).

The surface albedo feedback (SAF) has been identified as the primary driver of polar amplification in some previous studies (Manabe and Wetherald, 1975; Manabe and Stouffer, 1980; Hall, 2004; Screen and Simmonds, 2010; Taylor et al., 2013). However, other processes have also been found to contribute substantially. The lapse rate feedback, which arises from vertical variations in atmospheric temperature changes and it acts as a positive feedback in the Arctic and a negative feedback in lower latitudes, has been found in some studies to be the largest contributor to Arctic polar amplification (Goosse et al., 2018; Pithan and Mauritsen, 2014; Stuecker et al., 2018). The nonlinearity of the Planck feedback, which describes how warmer temperatures lead to more outgoing longwave radiation (OLR) due to the Stefan-Boltzmann law, causes there to be greater warming in cold high-latitude regions for the same increase in OLR and has also been found to be one of the main feedbacks contributing to polar amplification.

Other processes that have been suggested to play a role in polar amplification include increases in poleward heat transport in the atmosphere, changes in cloud cover, and increases in water vapor. Increases in poleward atmospheric heat transport tend to enhance polar amplification, although this can be dampened by other feedbacks (Alexeev et al., 2005; Held and Soden, 2006; Hwang et al., 2011; Alexeev and Jackson, 2013), whereas changes in cloud cover can work as a positive or negative feedback depending on factors such as the time of year (Francis and Hunter, 2006; Schweiger et al., 2008; Kay and Gettelman, 2009). The water vapor feedback increases the level of global warming, but it is strongest in low latitudes and hence opposes polar amplification (Pithan and Mauritsen, 2014). Although these processes are typically thought to play a secondary role in the overall magnitude of polar amplification, they can be important when considering differences between climate models (Winton, 2006).

While previous research on polar amplification has focused mainly on the atmosphere, some studies using general circulation models (GCMs) have found increased northward ocean heat transport (OHT) into the Arctic Ocean under global warming (Holland and Bitz, 2003; Bitz

et al., 2006; Hwang et al., 2011). These changes in OHT are largely consistent among GCMs, with a robust decrease in northward OHT in the mid-latitudes associated with a weakened overturning circulation, and a robust increase in OHT around 60–80 °N (Hwang et al., 2011; Nummelin et al., 2017; van der Linden et al., 2019). Some studies of transient warming in GCMs have found that the ocean contributes to Arctic warming through this increased high-latitude OHT (Holland and Bitz, 2003; Mahlstein and Knutti, 2011) while other studies have found that the net effect of changes in OHT and ocean heat content opposes Arctic warming (Pithan and Mauritsen, 2014; Goosse et al., 2018). Nummelin et al. (2017) suggested that much of this discrepancy results from a focus on different latitude ranges and found that poleward of 75 °N, changes in OHT were positively correlated with Arctic polar amplification. An increase in the temperature of Atlantic Water (AW) that flows into the Arctic Ocean has been suggested to contribute to the increase in OHT in GCMs (Bitz et al., 2006; Nummelin et al., 2017; van der Linden et al., 2019). Paleoproxy evidence also suggests an increase in AW temperature coinciding with Arctic polar amplification (Spielhagen et al., 2011). However, spatially-uniform ocean warming with unchanged circulation would cause warmer AW but no change in OHT, and the underlying physical mechanisms for the increase in OHT have remained unresolved.

In this study, we identify a mechanism by which the upward vertical oceanic heat flux under sea ice increases under global warming, with a corresponding increase in the horizontal OHT into the polar region. We demonstrate the mechanism using an idealized seasonally-varying ocean–sea ice–climate model, which facilitates understanding of the underlying dynamics that could be at play in more complex models and also in the real world. We use a feedback locking approach to show that changes in the vertical heat flux in the Arctic Ocean are a substantial contributor to polar amplification in the present simulations and drive increases in OHT that are comparable to those found in GCMs.

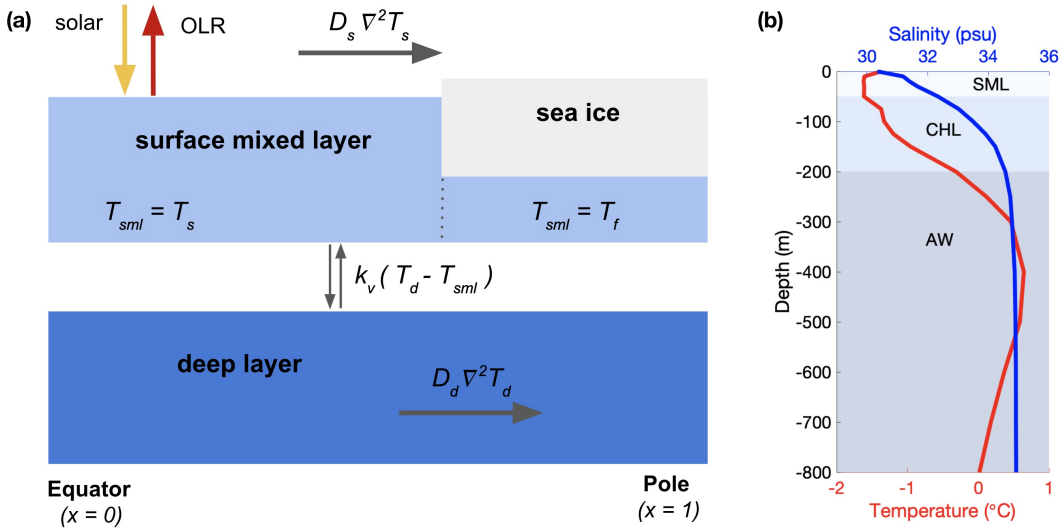


**Figure 3.1.** (a) Schematic of the idealized model, which represents the spatially and seasonally varying zonal-mean atmosphere, sea ice, ocean surface mixed layer (SML), and ocean deep layer in the Northern Hemisphere. The energy flux terms described in the main text are indicated, and $T_s$, $T_d$, and $T_f$ represent the surface temperature, ocean deep layer temperature, and freezing point, respectively. The ocean SML temperature, $T_{sml}$, is set to the surface temperature in ice-free locations and the freezing point where sea ice is present. (b) Annual-mean observed depth profiles in the Arctic Ocean, averaged horizontally over 80–90 °N, for temperature (red) and salinity (blue) (Levitus et al., 1994; Levitus and Boyer, 1994). The shading indicates the approximate depth ranges of three levels: the modeled SML, the cold halocline layer (CHL) separating the model layers, and the modeled deep layer which represents Atlantic Water (AW) in the Arctic.

## 3.2 Idealized Ocean–Sea Ice–Climate Model

A depth profile for the Arctic Ocean is shown in Fig. 3.1b. The upper Arctic Ocean can be characterized as consisting of a fresh and cold ocean surface mixed layer (SML) layer above a warmer AW layer, which is typically found to be below 200 m (Aagaard et al., 1981). The two layers are separated by a cold halocline layer (CHL) of rapidly increasing salinity, which is highly stable and thereby limits the flux of heat from the AW up to the SML and the sea ice cover. We represent these features in an idealized model, which is sketched in Fig. 3.1a. The two layers are fixed in depth to model the current climate's stratification of the SML and AW, where heat fluxes between the layers represent heat fluxes across the halocline. Note that there are regions where the local structure differs from this picture, such as the western Arctic Ocean where the

stratification features an additional layer of Pacific water separating the SML from the AW (e.g., Timmermans et al., 2008).

This model builds on the model developed previously by Wagner and Eisenman (2015, hereafter WE15), which has a single ocean layer representing the SML. WE15 combined the physics from idealized single-column model representations of thermodynamic sea ice processes (e.g., Eisenman and Wettlaufer, 2009; Eisenman, 2012) with that of energy balance models, or EBMs, of latitudinally- and seasonally-varying global surface temperature (e.g., Budyko, 1969; Sellers, 1969; North, 1975; North and Coakley, 1979). Here we add to this model a representation of a deeper ocean layer, somewhat analogous to previous idealized two-layer column models of the climate system (Gregory, 2000; Held et al., 2010). The deeper layer represents AW in the Arctic Ocean, and the two layers are coupled with a simple representation of the vertical heat flux that is proportional to the vertical temperature gradient, as shown in Fig. 3.1a.

The upper layer in the model includes the ocean SML, sea ice, and the atmosphere above (Fig. 3.1a). It is characterized by the surface enthalpy ($E_s$), which is a measure of the energy in the layer. We neglect the relatively small sensible heat contents of the atmosphere and of the sea ice and take $E_s$ to be proportional to the SML temperature ($T_{sml}$) referenced to the freezing point ($T_f$) where no ice is present and proportional to the sea ice thickness ($h$) where ice is present:

$$E_s \equiv \begin{cases} -L_f h & E_s < 0, \\ c_s \left(T_{sml} - T_f\right) & E_s > 0. \end{cases} \tag{3.1}$$

In the deep layer we define a similar enthalpy, which is simply proportional to the deep layer temperature, $T_d$:

$$E_d = c_d \left(T_d - T_f\right). \tag{3.2}$$

Here, $L_f$ is the sea ice latent heat of fusion, and $c_s \equiv \rho\, c_p\, H_s$ and $c_d \equiv \rho\, c_p\, H_d$ are the heat capacities for the surface and deep ocean layers, respectively, with $H_s$ the depth of the SML, $H_d$

the depth of the deep layer, $\rho$ the seawater density, and $c_p$ the seawater specific heat capacity. The freezing point, $T_f$, is fixed in the model. Where there is no ice, the SML temperature is equal to the surface temperature ($T_s$), but where ice is present it is taken to remain at the freezing point:

$$T_{sml} = \begin{cases} T_s & E_s > 0, \\ T_f & E_s < 0. \end{cases} \tag{3.3}$$

The enthalpy $E_s$ at each horizontal location in the layer evolves in response to the top-of-atmosphere incident solar radiation $S$ scaled by the coalbedo $a$ which is defined as one minus the albedo, OLR which is treated as a linear function of surface temperature $T_s$ with parameters $A$ and $B$, meridional heat transport in the atmosphere which is parameterized as diffusion of the surface temperature with constant coefficient $D_s$, vertical heat flux between the SML and the deep layer which is parameterized as a down-gradient heat flux with coefficient $k_v$, and a climate forcing term $F$ which can represent changes in atmospheric $CO_2$:

$$\frac{\partial E_s}{\partial t} = \underbrace{a\,S}_{\text{solar}} - \underbrace{\left[A + B\left(T_s - T_f\right)\right]}_{\text{OLR}} + \underbrace{D_s \nabla^2 T_s}_{\text{horizontal flux}} + \underbrace{k_v\left(T_d - T_{sml}\right)}_{\text{vertical flux}} + \underbrace{F}_{\text{forcing}}. \tag{3.4}$$

In the deep layer, horizontal heat transport is parameterized as diffusion of the ocean temperature with a coefficient $D_d$, leading to

$$\frac{\partial E_d}{\partial t} = \underbrace{D_d \nabla^2 T_d}_{\text{horizontal flux}} + \underbrace{k_v\left(T_{sml} - T_d\right)}_{\text{vertical flux}}. \tag{3.5}$$

Where $E_s < 0$, Eq. (3.4) describes the evolution of sea ice thickness. To find the surface temperature, we approximate a linear temperature profile within the ice between the surface at temperature $T_0$ and the base at the freezing point $T_f$. We define $T_0$ as the surface temperature that would cause the vertical heat flux through the ice to be balanced by the surface flux terms [as in

Eq. (3.4)] to give

$$\underbrace{k\,(T_f - T_0)/h}_{\text{heat flux through ice}} = -\underbrace{a\,S}_{\text{solar}} + \underbrace{[A + B\,(T_0 - T_f)]}_{\text{OLR}} - \underbrace{D_s \nabla^2 T_s}_{\text{horizontal flux}} - \underbrace{F}_{\text{forcing}}, \tag{3.6}$$

where $k$ is the sea ice thermal conductivity. If this balance (3.6) leads to $T_0 < T_f$, then the ice is freezing. Otherwise, the ice is melting and the surface of the ice is fixed at the freezing point. Hence the three cases for the surface temperature are

$$T_s = \begin{cases} T_f + E_s/c_s, & E_s > 0, & \text{(open water)}, \\ T_f, & E_s < 0,\ T_0 > T_f, & \text{(melting ice)}, \\ T_0, & E_s < 0,\ T_0 < T_f, & \text{(freezing ice)}. \end{cases} \tag{3.7}$$

The model accounts for converging meridians on the Earth by using the Laplacian operator for polar variations in spherical coordinates for the horizontal diffusion in the surface and deep layers,

$$\nabla^2 = \frac{\partial}{\partial x}\left[(1 - x^2)\frac{\partial}{\partial x}\right] \tag{3.8}$$

with $x \equiv \sin\theta$ with $\theta$ the latitude. The coalbedo $a$ is included with an empirically-motivated representation for ice-covered ($E_s < 0$) and ice-free ($E_s > 0$) conditions,

$$a = \begin{cases} a_0 - a_2 x^2 & E_s > 0, \\ a_i & E_s < 0, \end{cases}, \tag{3.9}$$

and the solar radiation varies with latitude and season as

$$S = S_0 - S_1 x \cos\omega t - S_2 x^2 \tag{3.10}$$

with $\omega = 2\pi \mathrm{yr}^{-1}$. The model domain is the Northern Hemisphere, and we approximate the heat

flux across the equator to be zero, which gives the boundary conditions

$$\left.\frac{\partial E_s}{\partial x}\right|_{x=0} = 0, \quad \left.\frac{\partial E_d}{\partial x}\right|_{x=0} = 0. \tag{3.11}$$

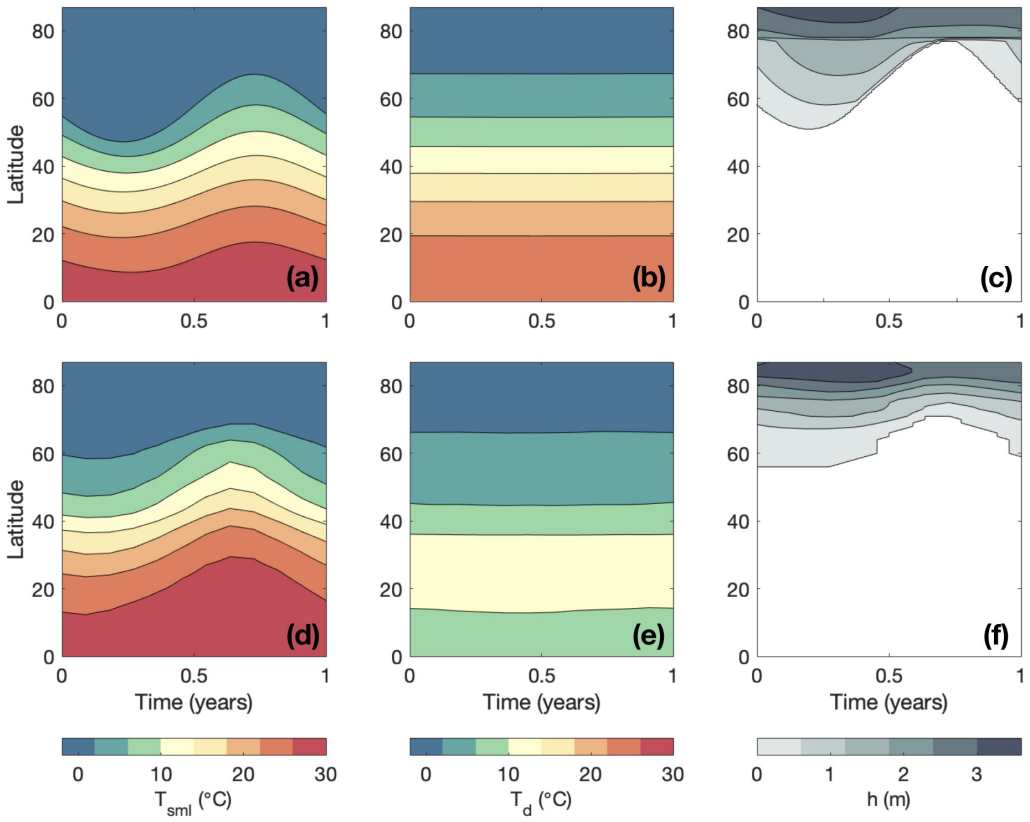


**Figure 3.2.** Idealized model results compared with observations. The top three panels are output for the final year of a model simulation with default parameter values, showing (a) the ocean SML temperature, (b) the ocean deep layer temperature, and (c) the sea ice thickness. The bottom three panels show observational estimates for comparison: (d) the zonal-mean 1950–1993 mean climatological sea surface temperature (Reynolds and Smith, 1995), (e) the 1900–1992 mean climatological ocean temperature averaged zonally and over the depth range 200–800 m (Levitus and Boyer, 1994), and (f) the zonal-mean 1979-2000 mean climatological sea ice thickness omitting grid boxes with less than 15% ice concentration (Zhang and Rothrock, 2003).

These representations are equivalent to WE15 for the SML, sea ice, and atmospheric meridional heat transport, but we add a deeper ocean layer in the present model and replace the specified constant heat flux into the base of the SML in WE15 with the computed flux

$k_v(T_d - T_{sml})$. This adds two new parameters, the horizontal diffusion coefficient in the deep layer $D_d$ and the vertical heat flux coefficient $k_v$. Slight changes have been made to the parameters used in WE15 to better fit observations using the present model. The determination of the parameter values is described in supporting information Text S1, which draws on a number of additional previous studies (Reigstad et al., 2002; Nummelin et al., 2015; Davis et al., 2016; Peterson et al., 2017; Polyakov et al., 2017, 2018). A list of the parameter values is given in Table 3.1 and the model simulation results for the control climate are presented alongside observational estimates in Fig. 3.2.

Although the model domain stretches from the equator to the North Pole, our focus is on the Arctic. The SML depth is set to 50 m, which has been used in previous idealized models of the Arctic (e.g., Thorndike, 1992), although observed mixed layer depths vary widely. The deep layer depth is set to 600 m, corresponding to a depth range of 200–800 m which broadly characterizes the AW beneath the cold halocline in the Arctic Ocean (e.g., Carmack et al., 2015). Outside the Arctic this layer crudely represents the ocean thermocline, although the simulated temperature in this layer does not agree well with observations of this depth range in the tropics (Fig. 3.2b,e), where colder temperatures are associated with equatorial upwelling which is not represented in this model. The two layers are indicated in the Arctic Ocean depth profiles in Fig. 3.1b.

The model takes several centuries to fully spin up. We analytically calculate the approximate e-folding timescales of the surface and deep layer to be 1.6 years and 77 years, respectively (see supporting information Text S2, Fig. 3.4). All plotted simulation results were spun up for a minimum of 2000 years.

## 3.3 Results

In this model, the vertical heat flux from the deep ocean to the ice is proportional to the temperature difference between the SML temperature ($T_{sml}$) and the deep layer temperature ($T_d$).

Since the SML temperature is set to the freezing point ($T_f$) in regions of sea ice cover, rather than having the colder surface temperature, there is a relatively small temperature gradient between the SML and warmer Arctic deep layer, leading to a relatively small upward vertical heat flux across the halocline.

We simulate global warming in the model by increasing the climate forcing parameter $F$, which can be interpreted to represent an increase in atmospheric $CO_2$. We increase $F$ abruptly and then run the model until it is spun up at a new, warmer state. At locations where sea ice remains present, the warming results in a thinner ice cover but the SML temperature remains at the freezing point. Since the deep ocean layer warms, this results in an increase in the vertical heat flux, amplifying the warming in regions with sea ice cover. This is demonstrated in Fig. 3.3a, where midwinter temperatures for the SML and deep layer are shown for $F = 0$ Wm$^{-2}$ (default value, dashed lines) and for $F = 10$ Wm$^{-2}$ (solid lines). This relatively large change in climate forcing is used here to more clearly show the difference between the climates.

The change in the vertical heat flux is spatially dependent on the location of the ice edge. Since the ice edge moves throughout the year, this means the spatial difference in heat flux will change seasonally. This is illustrated for midwinter and midsummer in Fig. 3.5, where plots of the vertical heat flux at $F = 0$ Wm$^{-2}$ and $F = 3$ Wm$^{-2}$ reveal a slight decrease in the vertical heat flux at the initial ice edge (left side of dashed red line), and the greatest increase at the new ice edge (left side of solid red line).

Next, we investigate how this change in vertical heat flux affects the level of polar amplification in the model. This idealized model only feels the effect of one of the processes mentioned in the introduction that could contribute to polar amplification, the SAF, as well as the oceanic heating mechanism that is the focus of this study.

We adopt as the definition of the polar amplification factor

$$\mathrm{PA} \equiv \frac{\overline{\Delta T_{s,\mathrm{polar}}}}{\overline{\Delta T_{s,\mathrm{NH}}}}, \tag{3.12}$$

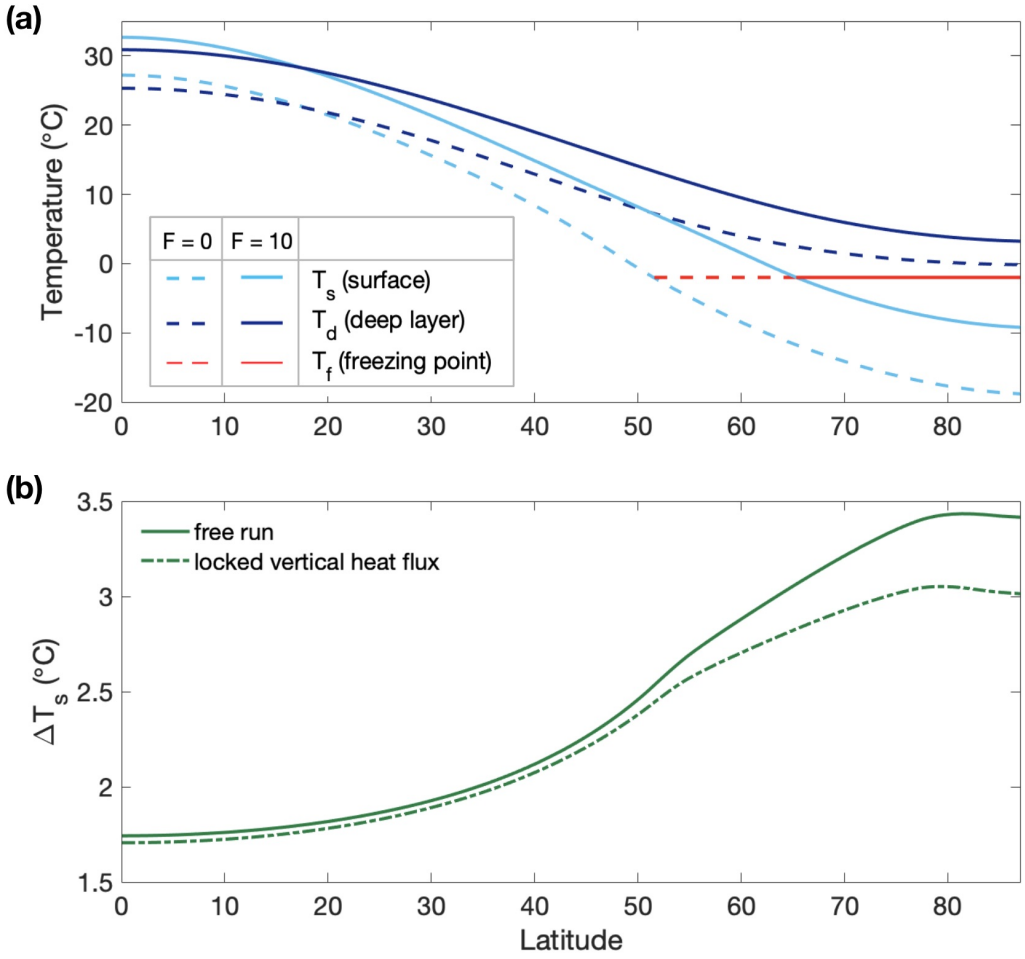


**Figure 3.3.** (a) Temperature variations between the equator and pole at midwinter ($t = 0.25$). Model results with $F = 0$ Wm$^{-2}$ are plotted as dashed lines and results with $F = 10$ Wm$^{-2}$ are plotted as solid lines. The surface temperature is indicated in light blue and the deep layer temperature in dark blue. The freezing point, which is the minimum allowed SML temperature, is indicated in red. This figure illustrates that as the temperature increases under forced warming (from dashed to solid lines), the difference between the deep layer temperature (dark blue) and SML temperature which is fixed at the freezing point in locations with sea ice (red) increases at high latitudes, leading to an increase in the vertical flux upward into the SML. (b) Annual-mean surface temperature difference between simulated climates with climate forcing set at $F = 0$ Wm$^{-2}$ and $F = 3$ Wm$^{-2}$. The solid green line indicates the results from the model in its standard configuration. The dash-dotted line indicates the case with the vertical heat flux locked to match the field simulated in the run with $F = 0$ Wm$^{-2}$.

where $T_{s,\mathrm{polar}}$ is the surface temperature averaged over 70–90 °N and $T_{s,\mathrm{NH}}$ is the surface temperature averaged over 0–90 °N, the bar denotes the annual mean, and $\Delta$ indicates the change between two climates. Note that a range of polar amplification factor definitions have been used

in previous studies (as reviewed in Hind et al., 2016).

In Fig. 3.3b, we plot the change in surface temperature when $F$ is increased from 0 to 3 $\mathrm{Wm}^{-2}$. This increase can be compared with the radiative forcing from doubling of $CO_2$, which is estimated to be 3.7 $\mathrm{Wm}^{-2}$ with a range of ±20% (Collins et al., 2013). Note however that because this idealized model lacks the water vapor feedback and other processes, the hemispheric-mean temperature in the model warms by 2 °C in response to this increase in $F$, compared with equilibrium climate sensitivities to doubling $CO_2$ in GCMs which typically fall in the range 3.2 ± 1.3 °C (Flato et al., 2013).

We lock the feedback associated with changes in the vertical heat flux across the halocline by replacing the vertical flux term in Eq. (3.4) by a specified seasonally-varying and latitudinally-varying field that is equal to the field simulated with the default value of $F = 0$ $\mathrm{Wm}^{-2}$. Previous studies have used similar feedback locking methods to evaluate the strength of the SAF by keeping the surface albedo field fixed while the ice retreats under global warming (Cess et al., 1991; Hall, 2004; Graversen and Wang, 2009). Fig. 3.3b shows temperature variations in simulations with the vertical heat flux locked (dash-dotted green line) compared with free runs (solid green line) that have the vertical heat flux evolve as the climate warms according to Eq. (3.4). The polar amplification factor in the locked case is $\mathrm{PA}_{locked} = 1.45$, and in the free case it is $\mathrm{PA}_{free} = 1.55$. Note that the locked vertical heat flux version of the model is equivalent to a one-layer model with a prescribed heat flux into the bottom. We calculate the contribution to polar amplification by the vertical heat flux as follows (Graversen et al., 2014):

$$\mathrm{PA}_{contribution} = \frac{\mathrm{PA}_{free} - \mathrm{PA}_{locked}}{\mathrm{PA}_{free} - 1}. \tag{3.13}$$

The result in Fig. 3.3b is $\mathrm{PA}_{contribution} = 0.2$. In other words, the contribution to polar amplification from enhanced heat flux across the halocline in the idealized model is 20%. Note that the remaining polar amplification in the model is due to the SAF, since only the SAF and the enhanced vertical heat flux contribute to polar amplification in this idealized model. This is

demonstrated with further feedback locking simulations in Fig. 3.6, where a small amount of polar amplification can be seen in simulations when the surface albedo is locked but the vertical heat flux is free to evolve, but no polar amplification occurs when both the surface albedo and vertical heat flux are locked. Other processes contributing to polar amplification that are not included in the model, such as the lapse rate feedback, could complicate these results.

Nonetheless, the idealized model results can be compared with previous GCM simulations that showed an increase in high-latitude OHT under warming. In a direct test of how this impacts Arctic warming, Singh et al. (2017) found that changes in ocean heat flux convergence in a GCM contributes 23% to Arctic amplification over ocean regions under $CO_2$ doubling, although a physical mechanism was not identified. This result is similar to the idealized model result of 20% in the present study, which is directly attributable to the mechanism proposed here. The increase in OHT found in this idealized model can also be compared with GCMs. Hwang et al. (2011) found that 9 out of the 10 GCMs they analyzed simulated increased OHT at 70 °N under warming, with the OHT per degree of global warming falling between 0.001 PW and 0.03 PW (under the SRES "A2" scenario). The idealized model result falls within this range, with a increase of 0.007 PW at 70 °N per degree of hemispheric warming. The change in OHT for a simulation with the idealized model that undergoes 2 °C of hemispheric-mean warming is shown in Fig. 3.7.

## 3.4 Discussion

In Fig. 3.3b the free run has a larger increase in global-mean temperature than the run with a locked vertical heat flux. This occurs due to the interaction between the two processes that drive polar amplification in the model: changes in vertical heat flux influence the sea ice cover and hence the albedo. Further feedback locking simulations demonstrate that due to these interactions, polar amplification from the enhanced heat fluxes alone plus that due to the SAF alone is smaller than the polar amplification when both processes occur (see Fig. 3.6). Hence the result $PA_{contribution} = 0.2$ represents a combination of the contribution from changes to the

vertical heat flux and the nonlinear contribution from interactions between the vertical heat flux and the surface albedo. The highest contribution from the SAF occurs near the ice edge, which explains why the maximum temperature change in Fig. 3.3b occurs at approximately 80 °N rather than at the pole.

The ocean heat flux mechanism presented here acts to enhance the temperature response to both positive and negative climate forcing anywhere that sea ice is present (and the ocean temperature increases with depth). This is in contrast to the SAF, which enhances changes only in locations where the sea ice cover changes. Both processes are hence expected to contribute to polar amplification of warming in climates resembling the present day or warmer, with sea ice residing in much of the Arctic Ocean. However, the results are expected to differ for climates with the ice edge residing outside of the Arctic. We explore the sensitivity to these factors by varying the initial and final values of $F$ (see Figs. 3.8, 3.9). We find that when the Arctic becomes ice free in the summer, the contribution to polar amplification of the proposed mechanism and the SAF both decrease, and when the Arctic Ocean becomes ice free throughout the year, neither mechanism contributes and the model has no polar amplification, as expected. The results of colder simulated climates are discussed in the supporting information Text S3.

This mechanism is proposed as a possible explanation for the increase in polar OHT in GCM simulations of greenhouse-driven warming. However, it should be emphasized that the model we use to demonstrate the mechanism has idealized diffusive representations of horizontal and vertical ocean heat fluxes, and aspects of the complex ocean circulation and heat transport simulated in GCMs that are not captured by this idealized representation could also contribute to the increase in simulated OHT. One indicator of the proposed mechanism that could be used to help identify whether it is occurring in GCM simulations would be to examine the spatial structure of changes in the vertical heat flux, since the mechanism notably causes an increase in the heat flux across the base of the ocean mixed layer in a given season only in locations that have sea ice in both the initial and final state (as shown in Figs. 3.3a and 3.5). This would be expected to be most readily identifiable in GCM simulations of the equilibrium response to $CO_2$ increases.

All simulations in this study were run to approximate equilibrium, and the caveat should be noted that transient climates could behave differently. In an equilibrium state, ocean heat uptake is zero, but in a transient state, some studies have found that increases in ocean heat uptake oppose polar amplification (Pithan and Mauritsen, 2014; Goosse et al., 2018).

Although the model presented here is focused on Arctic regions where the lower layer represents AW, the proposed mechanism could apply to any warm water mass resting below ice. In ice-covered regions in the Western Arctic, it has been observed that halocline waters at depths of around 50–150 m are heating up faster than the surrounding waters. Since the surface waters under sea ice remain near the freezing point, the mechanism presented here may be expected to cause increased upward heat fluxes into the SML (cf Timmermans et al., 2018). The proposed mechanism could also play a role in the Antarctic, where relatively warm circumpolar deep water resides below a fresher, cooler SML. Antarctic amplification is seen in some GCM simulations of the equilibrium response to increasing greenhouse forcing. Such GCM simulations have found that OHT increases in the polar regions of both hemispheres, although cloud changes in the Southern Hemisphere may compete with this effect (Singh et al., 2017).

## 3.5 Summary

This study presents a mechanism by which changes in the vertical heat flux across the halocline in the Arctic Ocean cause an increase in OHT into the Arctic, amplify sea ice retreat, and contribute to polar amplification. We demonstrate the mechanism using an idealized model of the Northern Hemisphere atmosphere, sea ice, ocean SML, and deeper ocean waters. The mechanism hinges on the surface water beneath the sea ice being fixed near the freezing point. When the climate warms, the deep water warms while surface waters under sea ice remain near the freezing point, which leads to an increase in the vertical temperature gradient and hence also an increase in the vertical heat flux from the deep waters to the surface waters. This enhances the warming in any regions that have sea ice and have subsurface waters that are warmer than the

surface waters, as is the case in much of the Arctic Ocean.

This increase in vertical heat flux in the Arctic region necessitates an increase in the horizontal heat flux into the Arctic deep ocean layer. Such an increase in ocean heat transport under global warming has been noted previously in GCM simulations, but the physical mechanism has remained elusive. The mechanism presented here may provide an explanation for this behavior.

We use a feedback locking approach to suppress the influence of vertical heat flux changes and thereby quantify the contribution of the proposed mechanism to polar amplification. The results show that changes in the vertical heat flux contribute 20% to polar amplification in the idealized model. This result is similar to previous GCM simulations which tested the influence of changes in ocean heat flux convergence on Arctic amplification under global warming (Singh et al., 2017).

Previous work has identified a process by which atmospheric heat transport into the polar regions fundamentally increases under warming due to latent heat effects and the Clausius-Clapeyron relationship (Alexeev et al., 2005; Held and Soden, 2006). This work suggests that there is also a process by which ocean heat transport into the Arctic increases under warming due to changes in the vertical heat flux in the ocean.

## 3.6 Acknowledgments

Many thanks Effie Fine, Marion Alberty, Jen MacKinnon, and Shantong Sun for helpful discussions and also two anonymous reviewers for helpful comments. This work was supported by National Science Foundation grant OPP-1643445. The code to numerically solve the model is available on GitHub: https://eisenman-group.github.io (doi:10.5281/zenodo.3628886). The observational data used in Figs. 3.1 and 3.2 was downloaded from http://iridl.ldeo.columbia.edu and https://pscfiles.apl.uw.edu/zhang/PIOMAS.

Chapter 3, in full, is a reprint of the material as it appears in Geophysical Research Letters, 2020. Beer, E., I. Eisenman, and T. J. W. Wagner, 2020: Polar amplification due to enhanced

heat flux across the halocline. *Geophysical Research Letters*, **47(4)**. The dissertation author was the primary investigator and author of this paper.

## 3.7 Supporting Information

**Text S1. Determining Model Parameter Values.**

The model developed in the present study has two new parameters in addition to the parameters in the previous model of Wagner and Eisenman (2015): the horizontal diffusion coefficient in the deep layer $D_d$ and the vertical heat flux coefficient $k_v$. Some changes have also been made here to the parameter values used in Wagner and Eisenman (2015). These include shifting the freezing point ($T_f$) from 0 °C to −2 °C, which approximates the actual value for the salinities of 31 to 36 psu that are typically found in the Arctic Ocean (see Fig. 3.1b in the main text) and thereby better facilitates comparison with observations (Fig. 3.2 in the main text). The atmospheric diffusion coefficient $D_s$, solar cycle amplitude $S_1$, and OLR parameter $A$ are also adjusted slightly from the values in WE15 to better fit observations using the present model (see bottom row of Fig. 3.2 in the main text). All parameter values are given in Table 3.1.

For the new parameters, the value of $D_d$ is chosen to match observed temperature profiles and observations of horizontal heat transport. It gives an annual-mean northward OHT across 70 °N divided by the area poleward of 70 °N of 4.8 $\mathrm{Wm}^{-2}$, which is consistent with observations that the northward heat transport by AW through Fram Strait contributes a basin-averaged flux to the Arctic Ocean of $5 \pm 1$ $\mathrm{Wm}^{-2}$ (Carmack et al., 2015). The value $k_v = 2$ W $\mathrm{m}^{-2}$ $\mathrm{K}^{-1}$ is chosen to give an observationally consistent seasonal cycle in ice thickness. Note that this value for $k_v$ is similar to the value of 1.6 W $\mathrm{m}^{-2}$ $\mathrm{K}^{-1}$ used for a similar parameter in the column model of the global climate of Gregory (2000), which has upper and lower layer thicknesses of 150 m and 2400 m, respectively. The vertical flux averaged annually and over 70–90 °N in the control climate simulated in the model is 4.8 $\mathrm{Wm}^{-2}$, which is within the observed range of vertical flux for the Eastern Arctic Ocean of 1–5 $\mathrm{Wm}^{-2}$ (Carmack et al., 2015; Peterson et al., 2017; Polyakov

et al., 2017).

The values of these two parameters are expected to influence the contribution to polar amplification from the proposed mechanism, because they control how much heat gets transported into the deep Arctic Ocean and then up to the Arctic Ocean surface. In the model, $k_v$ and $D_d$ are set to constant values to best match the current climate. However, some observations and model results suggest that making these parameters dependent on the background climate state could possibly be more accurate. For example, the surface freshwater flux into the Arctic Ocean is predicted to increase under global warming in the future leading to enhanced stratification (Nummelin et al., 2015; Davis et al., 2016), which would be associated with a decrease in $k_v$. On the other hand, observations during recent decades suggest that there has been a shoaling of the AW as part of "atlantification", which is a term that describes how some characteristics of the Arctic Ocean are becoming more like the North Atlantic (Reigstad et al., 2002; Polyakov et al., 2017, 2018), and this would be associated with an increase in $k_v$ due to a weaker halocline layer insulating the AW from the SML.

Sensitivity to changes in the constant values of both of these parameters are explored in Fig. 3.10, where increases in either parameter are shown to result in an increase in the importance of the vertical heat flux mechanism for polar amplification.

It should be noted that since this model has many parameters, there may be another set of parameter values where the climate looks similar but responds differently to climate forcing.

**Text S2. Analytical Estimate of Model Time Scales.**

The transient evolution of the idealized model can be characterized by two timescales. The behavior is simplest when conditions are ice-free everywhere, which is the case we initially consider here. In this case we can make the simplifications that the surface enthalpy everywhere is proportional to the surface temperature ($E_s = c_s T_s$), the coalbedo ($a$) depends only on latitude, and the surface mixed layer temperature everywhere is equal to the surface temperature ($T_{sml} = T_s$).

Taking the global mean of Eqs. 3.4 and 3.5 in the main text, we find,

$$c_s \frac{d\overline{T_s}}{dt} = \overline{a\,S} - A - B\,(\overline{T_s} - T_f) + k_v\,(\overline{T_d} - \overline{T_s}) + F \tag{3.14}$$

and

$$c_d \frac{d\overline{T_d}}{dt} = k_v\,(\overline{T_s} - \overline{T_d}), \tag{3.15}$$

where bars denote averages over both the hemisphere and the year. To separate the timescales between the surface mixed layer and deep layer, we use that $c_d \gg c_s$. To find the fast timescale, we approximate that $T_d$ is constant and equal to its initial condition, $\overline{T_d} = T_d^0$, giving the solution to Eq. 3.14:

$$\overline{T_s} = (T_s^0 - T_s^F)\,\exp(-t/\tau_f) + T_s^F. \tag{3.16}$$

Here, $T_s^0$ is the initial condition and the steady state solution under forcing $F$ is

$$T_s^F \equiv \frac{\overline{a\,S} - A + B\,T_f + F + k_v T_d^0}{B + k_v}, \tag{3.17}$$

with the fast timescale,

$$\tau_f \equiv \frac{c_s}{B + k_v} = 1.6 \text{ years}. \tag{3.18}$$

To find the slow time scale, we assume the surface mixed layer is in steady state, $c_s \frac{d\overline{T_s}}{dt} = 0$, which allows us to use Eq. 3.14 to find the surface temperature as a function of $\overline{T_d}$. The gives a solution to Eq. 3.15:

$$\overline{T_d} = (T_d^0 - T_d^F)\,\exp(-t/\tau_s) + T_d^F, \tag{3.19}$$

where the steady state solution under forcing $F$ is

$$T_d^F = \frac{\overline{a\,S} - A + B\,T_f + F}{B}, \tag{3.20}$$

and the slow timescale is

$$\tau_s = \frac{c_d\,(B + k_v)}{k_v B} = 77 \text{ years}. \tag{3.21}$$

These take a form analogous to the timescales found in the theoretical model of Held et al. (2010), although they have different values because of the parameters.

In order to consider evolution of the surface temperature on longer timescales, the evolution of the deep layer 3.19-3.21 can be included in the equations for the surface temperature evolution 3.16-3.18 as

$$\overline{T_s} = \frac{k_v F}{B\,(B + k_v)} \exp(-t/\tau_f - t/\tau_s) - \frac{F}{B} \exp(-t/\tau_f) - \frac{k_v F}{B\,(B + k_v)} \exp(-t/\tau_s) + T_s^F. \tag{3.22}$$

This combined analytical approximation describes the annual-mean global-mean surface temperature after the forcing is instantaneously changed by $F$ from an equilibrated model state with $F = 0$. Note that the governing equations for an ice-free climate [Eqs. 3.14-3.15] can also be solved exactly, which leads to a quantitatively similar but less transparent solution.

These analytical approximations to the solution are compared with the numerical solution in Fig. 3.4. For ice-free conditions (top four panels), the simple approximate solution for $\overline{T_s}$ 3.16-3.18 agrees well with the numerical solution during the first few e-foldings, and the combined solution 3.22 agrees fairly well thereafter. When ice is present, the simulated steady state temperature change under a given change in climate forcing is underestimated by this representation because it does not take into account changes in surface albedo, as shown in Fig. 3.4 (bottom two panels).

**Text S3. Widely Varied Climates.**

Both the oceanic mechanism presented in the main text and the surface albedo feedback (SAF) depend on the location of the ice edge. The oceanic mechanism enhances warming in locations where ice is present, whereas the SAF enhances warming only in locations of ice loss.

**Table 3.1.** Model parameters and values

| Parameter | Description | Value |
|---|---|---|
| $A$ | OLR reference value (W $m^{-2}$) | 189 |
| $a_0$ | Ice-free coalbedo at equator | 0.7 |
| $a_2$ | Ice-free coalbedo spatial dependence | 0.1 |
| $a_i$ | Ice-covered coalbedo | 0.4 |
| $B$ | OLR temperature dependence (W $m^{-2}K^{-1}$) | 2.1 |
| $c_d$ | Deep layer heat capacity (W yr $m^{-2}K^{-1}$) | 78.4 |
| $c_s$ | Surface mixed layer heat capacity (W yr $m^{-2}K^{-1}$) | 6.53 |
| $D_d$ | Coefficient for horizontal heat transport in deep layer (W $m^{-2}K^{-1}$) | 0.08 |
| $D_s$ | Coefficient for horizontal heat transport in atmosphere (W $m^{-2}K^{-1}$) | 0.5 |
| $F$ | Climate forcing (W $m^{-2}$) | 0 (varies) |
| $k$ | Sea ice thermal conductivity (W $m^{-1}K^{-1}$) | 2 |
| $k_v$ | Vertical heat flux coefficient (W $m^{-2}K^{-1}$) | 2 |
| $L_f$ | Sea ice latent heat of fusion (W yr $m^{-3}$) | 9.5 |
| $S_0$ | Insolation at equator (W $m^{-2}$) | 420 |
| $S_1$ | Insolation seasonal dependence (W $m^{-2}$) | 355 |
| $S_2$ | Insolation spatial dependence (W $m^{-2}$) | 240 |
| $T_f$ | Freezing temperature (°C) | −2 |

An implication of this is that the SAF would cause the Arctic temperature to change less than the global-mean temperature in cold climates with the sea ice edge residing outside the Arctic, whereas the proposed mechanism would always cause Arctic amplification as long as the Arctic is ice-covered and only a smaller fraction of the global ocean has sea ice. This can be see in Fig. 3.9, which has PA $< 1$ for runs with a locked vertical heat flux (yellow) in the coldest simulated climates (with starting values of $F$ below $-13$ $Wm^{-2}$), which indicates that the SAF acts against Arctic amplification in these climates. On the other hand, nearly all of the runs with the vertical heat flux free to evolve (orange) have more polar amplification than the locked runs in Fig. 3.9, which indicates that the ocean heat flux mechanism enhances Arctic amplification in nearly the full range of the simulated climates. There are exceptions to this, however, at both edges of the plot: when the starting values of $F$ is $-19$ $Wm^{-2}$, the run with free vertical heat flux transitions into a snowball earth state; and when the starting values of $F$ is greater than 16 $Wm^{-2}$, there is no sea ice throughout the year and neither process contributes to Arctic amplification.

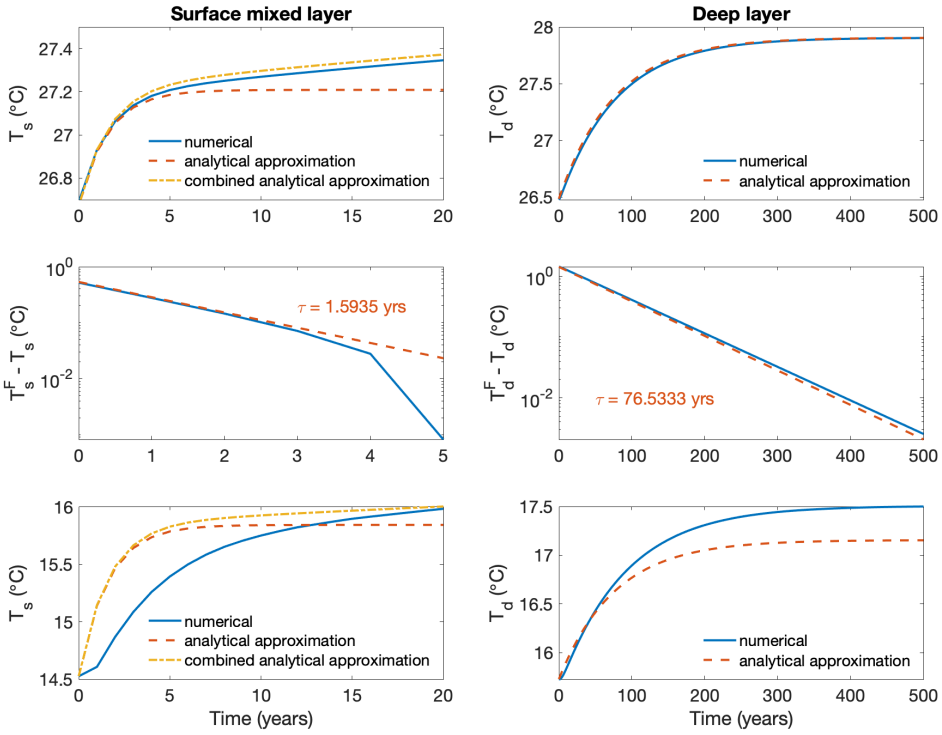


**Figure 3.4.** Transient evolution of the annual-mean hemispheric-mean surface mixed layer temperature (left) and deep layer temperature (right). Numerical solutions of the idealized model are shown in solid blue. For the surface mixed layer, the analytical approximation that holds $T_d$ constant [Eqs. 3.16-3.18] is indicated as an orange dashed line and the combined analytical approximation that includes the evolution of $T_d$ [Eq. 3.22] is indicated as a yellow dash-dotted line. For the deep layer, the analytical approximation that uses a steady-state approximation for $T_s$ [Eqs. 3.19-3.21] is indicated as an orange dashed line. The top four panels are for a simulated climate that is sufficiently warm to be completely ice-free. In the top two panels, the analytical solutions provide fairly accurate approximations to the numerical solutions. Note that after several centuries, when the deep layer temperature is approximately in steady state, the combined analytical solution for $T_s$ matches the numerical solution (not shown). In the middle two panels, the departure of each temperature from it's final steady-state value is plotted using log-linear axis scaling, such that exponential decay appears linear with a slope given by the inverse of the decay timescale $\tau$. The bottom panel shows numerical results and the analytical approximation in the default climate, which has sea ice in high latitudes. In this case the analytical solutions do not capture the changes in albedo, which leads to an underestimation of the final steady-state temperature and an overestimation of the rate at which the surface temperature initially responds.

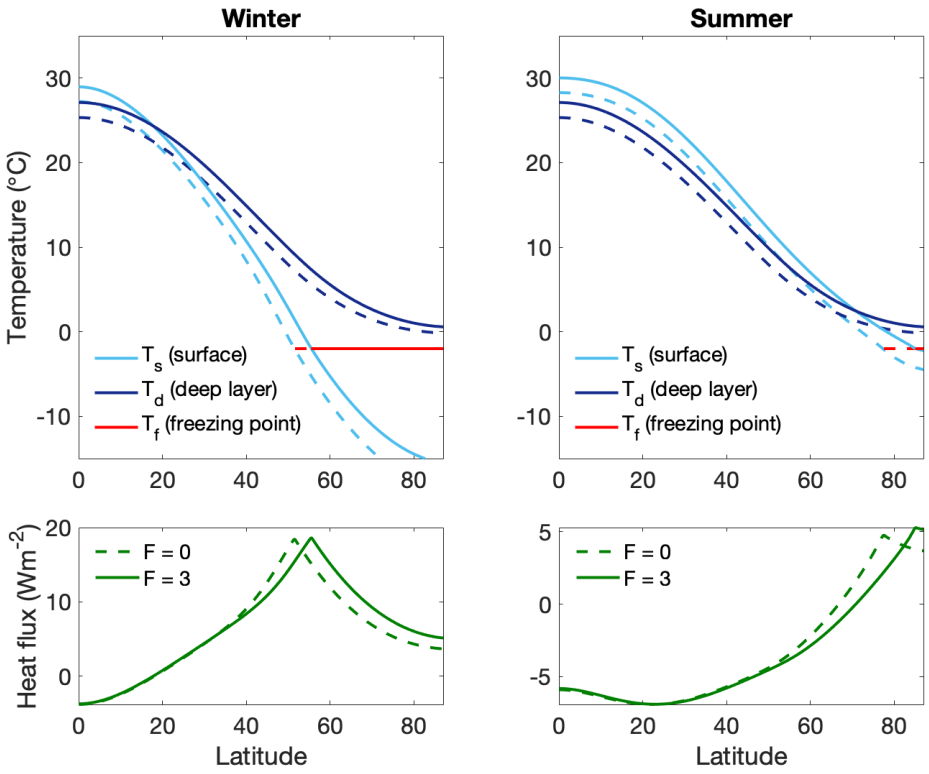


**Figure 3.5.** Temperature and vertical heat flux profiles plotted against latitude for midwinter (left, $t = 0.25$) and midsummer (right, $t = 0.75$). Dashed lines indicate the simulated climate with $F = 0$ Wm$^{-2}$ and solid lines indicate $F = 3$ Wm$^{-2}$. In the top panels, the surface temperature is in light blue, the deep layer temperature is in dark blue, and the freezing point is in red. The bottom panels show the vertical heat flux between the two layers, which is proportional to the difference between the surface mixed layer and deep layer temperatures. Note the surface mixed layer temperature is set to either the surface temperature (light blue) or the freezing point (red) depending whether or not ice is present (i.e., whether the surface temperature is less than the freezing point).

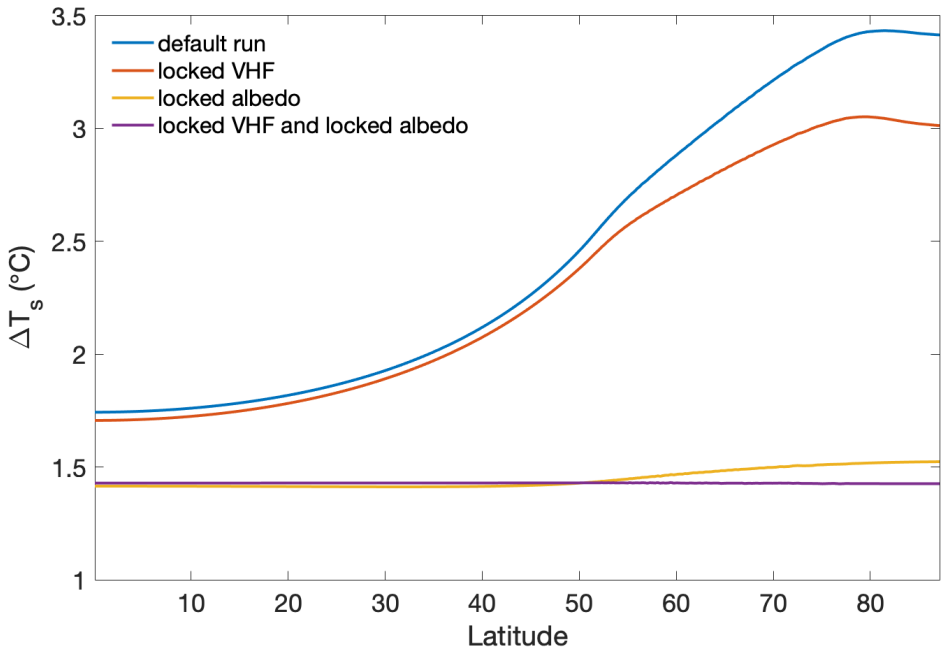


**Figure 3.6.** Annual-mean surface temperature difference between simulated steady-state climates with $F = 3$ Wm$^{-2}$ and $F = 0$ Wm$^{-2}$. The blue and orange lines are equivalent to what is plotted in Fig. 3.3b in the main text (solid and dash-dotted green lines, respectively). Here, the yellow line shows the case when only the albedo is locked, and the purple line shows the case when both the albedo and the vertical heat flux (VHF) are locked (in which case there is no polar amplification as expected). It can be seen that if the contributions from the surface albedo alone (orange line) and VHF alone (yellow line) are linearly added, they do not sum to the total polar amplification shown in blue. This suggests there is a nonlinear contribution from the interaction between the VHF and the surface albedo.

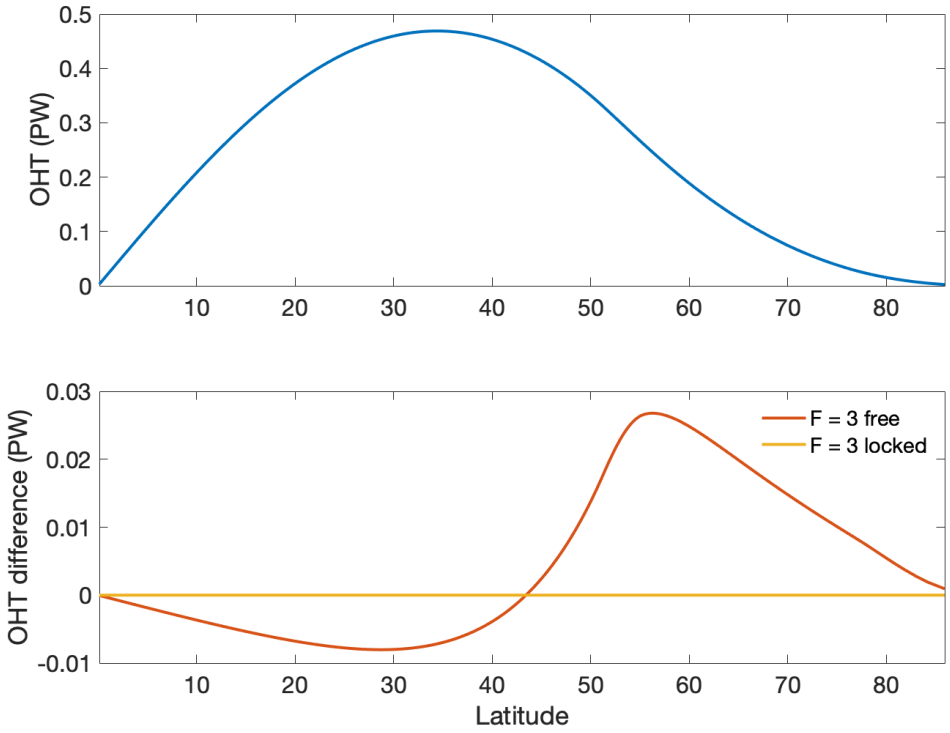


**Figure 3.7.** Annual-mean ocean heat transport (OHT). The top panel shows annual-mean OHT for the default climate scenario ($F = 0$ Wm$^{-2}$). The difference between the default climate case and the warmed climate cases ($F = 3$ Wm$^{-2}$) is plotted in the bottom panel, where simulations using the default model configuration are shown in orange ("free"), and simulations with the vertical heat flux locked to match the initial climate are shown in yellow ("locked"). Since OHT does not change in the locked case, the yellow line is at 0 PW. In the free case, the increase in OHT into the polar region (at 70 °N) is 0.015 PW, or 0.007 PW per degree of hemispheric warming. This value falls within the range of GCM projections, as discussed in the main text, although the maximum increase in OHT occurs at a more southward location than in most GCMs (Hwang et al., 2011). Note however that these results include only heat transport in the depth range 200–800 m, and the idealized model does not include representations of the Atlantic Meridional Overturning Circulation and a range of other processes that influence total heat transport in the global ocean, so the simulated OHT plotted here is not expected to closely match the global distribution of zonally–integrated depth–integrated OHT typically found in GCMs and observational estimates (e.g., Flato et al., 2013).

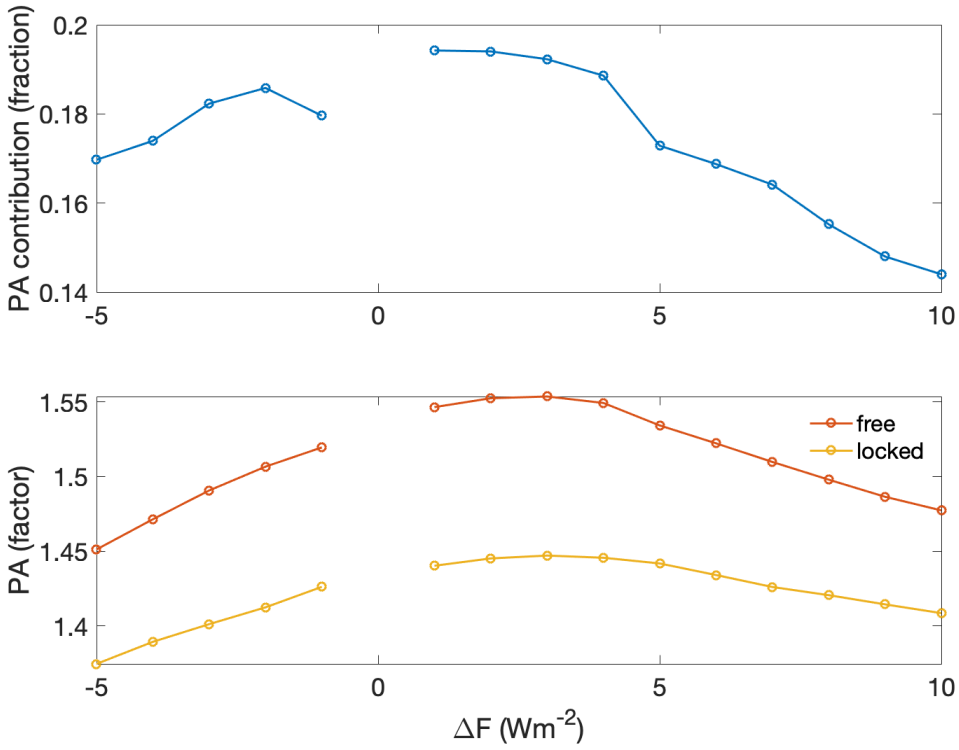


**Figure 3.8.** Sensitivity of polar amplification (PA) to the change in climate forcing for simulations starting at $F = 0$ and ending at $F = \Delta F$. The bottom panel shows PA for simulations using the default model configuration in orange ("free"), and simulations with the vertical heat flux locked to match the initial climate in yellow ("locked"). Note that PA is not defined for $\Delta F = 0$. The top panel shows the corresponding contribution to PA, $\text{PA}_{contribution}$, which is given in Eq. 3.13 of the main text. Note that after warming of at least $\Delta F = 4$ Wm$^{-2}$, the Arctic is seasonally ice-free; this is the range where the PA values start to decrease in the bottom panel. With negative forcing ($\Delta F < 0$), the model is being cooled and polar amplification refers to enhanced cooling rather than enhanced warming. In this scenario, the vertical heat fluxes are still contributing to polar amplification.

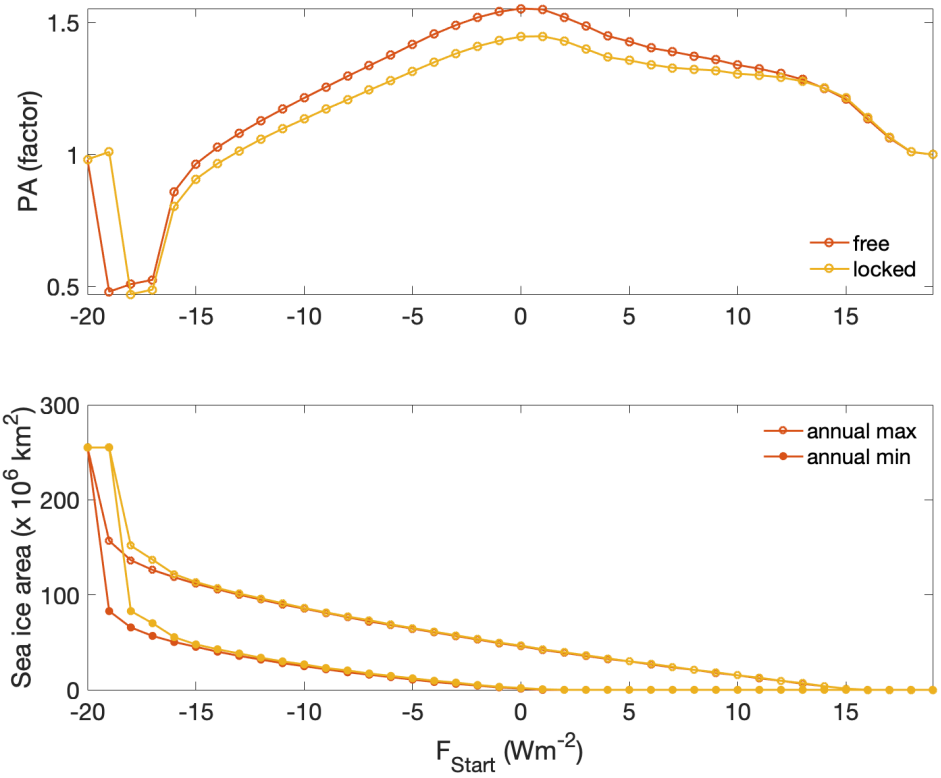


**Figure 3.9.** Sensitivity of polar amplification (PA) to the initial climate. The model is initially run to steady state under forcing $F_{\text{Start}}$, and then the forcing is increased by $\Delta F = 3$ Wm$^{-2}$ and the model is run until it again reaches steady state. The top panel shows the level of PA associated with the difference between the two steady-state climates. Simulations using the default model configuration are shown in orange ("free"), and simulations with the vertical heat flux locked to match the initial climate are shown in yellow ("locked"). The bottom panel shows the annual minimum (closed circles) and maximum (open circles) sea ice area after warming by $\Delta F = 3$ Wm$^{-2}$ for the range of values of $F_{\text{Start}}$. Note the transitions at $F_{\text{Start}} = 1$ Wm$^{-2}$, when the warmer steady state has only seasonal ice, and at $F_{\text{Start}} = 4$ Wm$^{-2}$, when the initial climate has only seasonal ice, which are most evident in the top panel. In the colder climates, there is a jump to a completely ice-covered hemisphere (snowball earth) at $F_{\text{Start}} = -19$ and $-20$ for the locked and free cases, respectively. Note that here the PA is not exactly at one as the system is not in steady state in the simulated snowball earth. At $F_{\text{Start}} = 19$, both runs becomes completely ice-free throughout the year, and there is no polar amplification in the model (PA = 1).

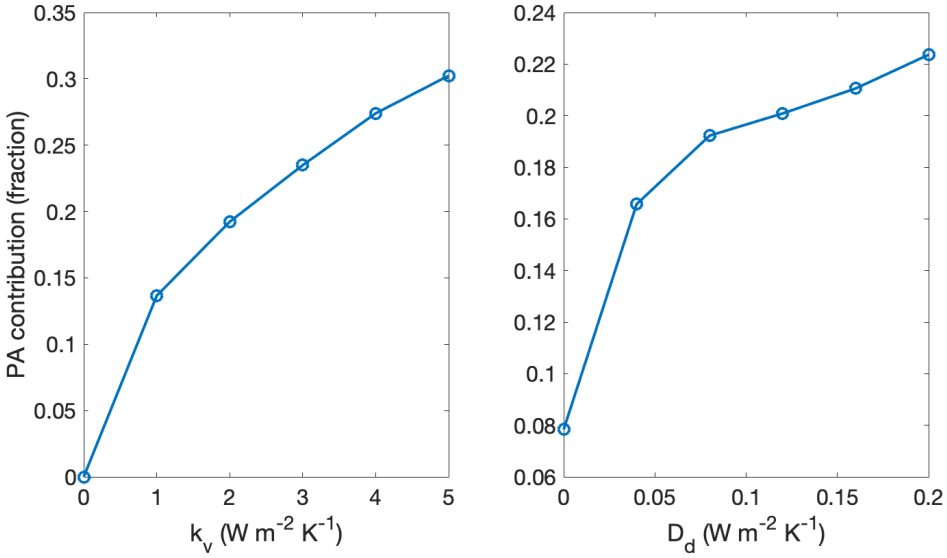


**Figure 3.10.** Sensitivity of polar amplification (PA) to model parameters when $F$ is increased from 0 $\mathrm{Wm}^{-2}$ to 3 $\mathrm{Wm}^{-2}$. Fractional contribution to PA [$\mathrm{PA}_{contribution}$, given in Eq. 3.13 of the main text] for changes in the model parameters $k_v$, which is related to the insulating effect of the halocline, and $D_d$, which is related to horizontal heat transport in the deep layer. (left) All model parameters are fixed at the default values except $k_v$ which is varied between 0 and 5, with the default value being 2. (right) All model parameters are fixed at the default values except $D_d$ which is varied between 0 and 0.2, with the default value being 0.08. Note that the PA contribution is not zero when $D_d$ is zero, which is due to the interaction between the surface albedo and the seasonal cycle of the vertical heat flux in the model: even without horizontal transport in the deep layer, heat can still enter the deep layer in ice-free areas during the summer and be released under ice in winter. Note also that the initial climate varies with the parameter values, which is not explicity taken into account here.

# Chapter 4

# A possible hysteresis in the Arctic Ocean due to release of subsurface heat during sea ice retreat

**Abstract**

The Arctic Ocean is characterized by an ice-covered layer of cold and relatively fresh water above layers of warmer and saltier water. It is estimated that enough heat is stored in these deeper layers to melt all the Arctic sea ice many times over, but they are isolated from the surface by a stable halocline. Current vertical mixing rates across the Arctic Ocean halocline are small, due in part to sea ice reducing wind-ocean momentum transfer and damping internal waves. However, recent observational studies have argued that sea ice retreat results in enhanced mixing. This could create a positive feedback whereby increased vertical mixing due to sea ice retreat causes the previously isolated subsurface heat to melt more sea ice. Here, we use an idealized climate model to investigate the impacts of such a feedback. We find that an abrupt "tipping point" can occur under global warming, with an associated hysteresis window bounded by saddle-node bifurcations. We show that the presence and magnitude of the hysteresis are sensitive to the choice of model parameters, and the hysteresis occurs for only a limited range of parameters. During the critical transition at the bifurcation point, we find that only a small percentage of the heat stored in the deep layer is released, although this is still enough to lead to substantial sea ice melt. Furthermore, no clear relationship is apparent between this change in

heat storage and the level of hysteresis when the parameters are varied.

## 4.1 Introduction

The Arctic Ocean is strongly salinity stratified, featuring a cold, relatively fresh, and often ice-covered surface layer above a halocline which has rapidly increasing salinity with depth. Below this, there is a reservoir of relatively warm, salty waters which can be a source of heat if it reaches the surface. These warmer and saltier waters have two origins. The first is Atlantic Water (AW) which flows into the Arctic Ocean through Fram Strait and the Barents Sea and resides at depths of approximately 200-800 m in much of the Arctic Ocean with temperatures around 0-3°C (Carmack et al., 2015). The second is Pacific Water which flows into the Arctic Ocean through the Chukchi Sea and resides at depths of 50-100 m in the Canada Basin with temperatures between -1°C and 1°C (Timmermans and Marshall, 2020).

For much of the upper Arctic Ocean away from steep topography, vertical mixing rates are lower than in the midlatitudes (Rippeth et al., 2015). The low mixing rates have been attributed to the halocline inhibiting deep convection, low tidal energy, and sea ice damping internal waves and reducing wind momentum transfer from the atmosphere (Morison et al., 1985; Dosser and Rainville, 2016). These low mixing rates prevent much of the heat stored at depth from reaching the surface (D'Asaro and Morison, 1992; Fer, 2009). As sea ice retreats under global warming and is replaced by open water, surface winds are expected to become more efficient at generating surface waves and internal waves (e.g., Rainville and Woodgate, 2009; Liu et al., 2016), thereby leading to increased vertical mixing. This vertical mixing may increase the heat flux from the warm deep waters to the surface, which in turn will accelerate sea ice melt, thus closing a positive feedback loop. We refer to this as the "wind-ice-ocean feedback" (cf. Fine and Cole, 2022). Note that similar processes have been referred to recently as the "ice/internal-wave feedback" (Dosser et al., 2021) and the "ice–ocean-heat feedback" (Polyakov et al., 2020).

This proposed feedback is supported by observations of increasing vertical heat fluxes

in the Eurasian Basin coinciding with sea ice retreat and a weakening stratification during the past decade (Polyakov et al., 2017, 2020). This is related to the phenomenon widely referred to as the "Atlantification" of the Arctic Ocean (e.g. Reigstad et al., 2002; Arthun et al., 2012; Polyakov et al., 2017). The proposed feedback is further supported by observed differences in internal wave amplitudes between ice-free and ice-covered conditions. Cole et al. (2018) found that the amplitude of internal waves in the Arctic Ocean was 80% larger in ice-free regions than in completely ice-covered regions. Further, the median amplitude of internal waves in the Arctic Ocean has been found to be larger in summer than winter despite weaker winds (Dosser and Rainville, 2016), suggesting that the ice cover limits the amplitude of internal waves. It has also been observed that the frequency of fall phytoplankton blooms, which have not typically been seen in the Arctic historically, are increasingly occurring (Ardyna et al., 2014). The emergence of fall blooms has been linked to increased storm activity in the fall, since strong wind events can mix nutrients up from depth (Nishino et al., 2015). On the other hand, looking at dissipation rates in the Arctic Ocean, Rippeth et al. (2015) found no difference between ice-free and ice-covered conditions. Other measurements in the western Arctic Ocean, where upper-ocean stratification is stronger (Lincoln et al., 2016; Dosser et al., 2021; Fine et al., 2021), similarly find little evidence of elevated dissipation at depth in response to wind forcing even under ice-free conditions, indicating that this feedback may not have a large effect in the western Arctic Ocean at present.

Motivated by these observations, here we explore the dynamics of a possible wind-ice-ocean feedback in the Eurasian Basin. To investigate this feedback in isolation, we use an idealized climate model in which we specify vertical mixing rates for ice-covered and ice-free surface conditions under a range of possible parameter choices. We then investigate the possibility of hysteresis and bifurcations under climate change, as well as the changes in heat transport and storage associated with the proposed feedback.

## 4.2 A Possible Hysteresis

Hysteresis occurs in a system when two stable states coexist in the same parameter regime (known as a bistability) in a limited region of the parameter space, and hence the history of the system determines which state it is in. When a parameter (such as greenhouse forcing) is varied such that a system becomes no longer bistable, a bifurcation is crossed, which can lead to an abrupt transition from one state to another. This is sometimes referred to as a "tipping point". Hence if the climate system passes such a threshold during global warming, the previous climate state cannot be recovered unless the level of greenhouse forcing is reduced substantially below its level immediately before the transition. In this case, when the greenhouse forcing is raised and then lowered, the climate system follows a hysteresis loop. Note however that during transient warming, the climate system is not in equilibrium and hence does not directly follow the underlying hysteresis loop, which could make bifurcation points less readily apparent.

Here we focus on the wind-ice-ocean feedback. We propose that this feedback could plausibly lead to a novel hysteresis in the climate system, implying an irreversible transition during sea ice decline. We consider a simple picture of this feedback in which vertical mixing in the upper Arctic Ocean is reduced where sea ice is present. The plausibility of multiple stable states under the same greenhouse forcing due to this feedback is illustrated schematically in Fig. 4.1. There is a cold climate state with polar sea ice present and hence reduced vertical mixing in the polar region, which allows the surface mixed layer to remain cold. And there is a warm ice-free state with enhanced vertical mixing which brings heat upward from the warm subsurface layer, thereby keeping the surface mixed layer warm. In the warm state, while the Arctic Ocean has a warmer surface, it actually has a colder subsurface, which is a striking signature of the proposed bistability. This is due to the enhanced upward heat flux in the polar region in the absence of sea ice, which is balanced by an enhanced horizontal heat transport in the subsurface layer. This bistability can only occur for a limited range of greenhouse forcing levels. When the greenhouse forcing is so large that subfreezing Arctic surface temperatures cannot occur, there

can no longer be bistability.

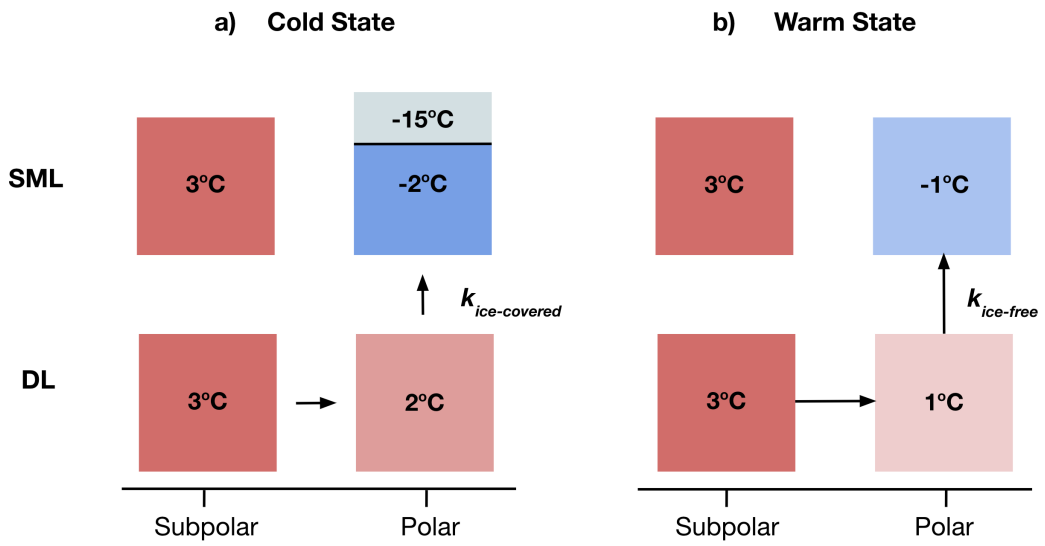


**Figure 4.1.** Schematic of the proposed plausible bistability, showing the surface mixed layer (SML) and ocean deeper layer (DL) temperatures at subpolar latitudes and polar latitudes for (a) the cold climate state and (b) the warm climate state, which are both possible under the same climate forcing. The surface temperature of the sea ice is also shown in panel a. The DL represents the Atlantic Water in polar latitudes. The vertical heat fluxes are modulated by the mixing coefficient $k$, which is larger under ice-free conditions than under ice-covered conditions. The length of the arrows indicate the magnitudes of the heat fluxes between boxes, which are equal to the temperature differences between the boxes multiplied by the mixing coefficients.

## 4.3 Idealized Climate Model

We use an idealized climate model in order to illustrate the proposed plausibility of bistable climate states supported by the wind-ice-ocean feedback. The model builds on the long-standing framework of diffusive energy balance models (EBMs). Such EBMs typically simulate the steady-state annual-mean zonal-mean surface temperature as a function of latitude within a global or hemispheric domain, based on the balance between top-of-atmosphere net solar radiation; top-of-atmosphere outgoing longwave radiation (OLR) which is approximated to depend linearly on the surface temperature; and meridional atmospheric heat transport which is represented as diffusion of the surface temperature (Budyko, 1969; Sellers, 1969; North, 1975).

For this study, we have added a second ocean layer to a classic EBM representation of the zonally-averaged annual-mean climate in the Northern Hemisphere. The top layer is taken to represent the ocean surface mixed layer (SML) and the atmosphere above, and below this the model has an added deeper layer (DL). The DL in the Arctic Ocean represents the Atlantic Water below the halocline. This is based on the stratification in the Eurasian Basin, which is thought to be more susceptible than other regions of the Arctic to increased internal wave activity and a wind-ice-ocean feedback under warming (Davis et al., 2016; Dosser et al., 2021). Pacific Water doesn't constitute a well-formed layer in the Eurasian Basin, and Atlantic water is the primary source of subsurface heat. Although the inclusion of the DL is motivated by Arctic Ocean characteristics, for simplicity we have it extend over the full hemispheric domain. Horizontal heat transport in the DL is parameterized as diffusion of the DL temperature, similar to the treatment of horizontal heat transport in the top layer. This is a crude treatment of heat transport in the ocean, which arises primarily due to large-scale advection and eddy mixing, but it offers a simple representation that moves heat from warmer regions to colder regions. The two layers are coupled using a simple representation of vertical heat flux that is proportional to the vertical temperature gradient. Hence the model is an idealized representation of the Northern Hemisphere that focuses on changes in ocean temperature and heat transport that arise from the wind-ice-ocean feedback.

The model is illustrated schematically in Fig. 4.2a. The SML is chosen to be 50 m thick, as in some previous idealized models (e.g., Thorndike, 1992; Eisenman and Wettlaufer, 2009). Note that the observed SML depth in the Arctic Ocean varies substantially with location and season. The DL is chosen to be 600 m thick, corresponding to a depth extending from 200 m to 800 m (see temperature and salinity profiles of the central Arctic in Fig. 4.2b). In most of the depth range of the DL, temperatures in 85-90 °N in Fig. 4.2b are warmer than 0°C (a typical definition of AW), and above 200 m, the salinity rapidly changes within the halocline. The halocline is not represented explicitly in the model but rather as the boundary between the two layers, so that vertical heat fluxes between the two ocean layers are interpreted as heat fluxes across the halocline. This two-layer representation is similar to the seasonally-varying model

used in a previous study (Beer et al., 2020), and it builds on earlier idealized two-layer column models of the climate system (e.g., Gregory, 2000; Held et al., 2010). Note that we focus here on equilibrium model states, which do not depend on the thicknesses of the SML and DL.

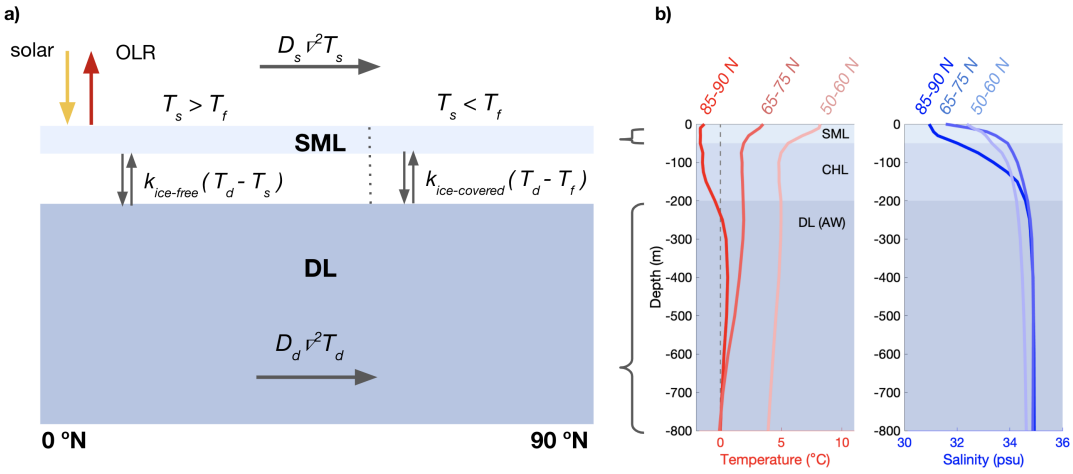


**Figure 4.2.** (a) Schematic of the idealized climate model, which represents the latitudinally-varying atmosphere, ocean surface mixed layer (SML), and ocean deeper layer (DL). In the Arctic Ocean the DL represents the Atlantic Water below the halocline. The surface temperature ($T_s$), DL temperature ($T_d$), and freezing point ($T_f$) are indicated, and energy fluxes represented in the model are shown as arrows. (b) Profiles of annual mean temperature and salinity from Levitus94 (Levitus et al., 1994; Levitus and Boyer, 1994). Profiles are averaged zonally and over latitude ranges as labelled. The SML, cold halocline layer (CHL) where salinity rapidly increases with depth, and Atlantic Water (AW) layer are indicated. The model layers in panel a are indicative of the Arctic Ocean stratification shown by the 85-90 °N profiles in panel b.

As in other standard EBMs, the surface temperature $T_s$ is determined from the balance of radiation and heat transport terms. Here we add a term representing the vertical heat flux between the SML and DL, as well as a spatially-uniform climate forcing term $F$ that can represent changes in greenhouse gases:

$$c_s \frac{\partial T_s}{\partial t} = \underbrace{(1-\alpha)\,S}_{\text{solar}} - \underbrace{[A + B\,(T_s - T_f)]}_{\text{OLR}} + \underbrace{D_s \nabla^2 T_s}_{\text{horizontal transport}} + \underbrace{k\,(T_d - T_{SML})}_{\text{vertical flux}} + \underbrace{F}_{\text{forcing}}, \qquad (4.1)$$

where the net solar radiation is equal to incident solar radiation at the top of the atmosphere $S$ minus reflected solar radiation $\alpha S$ with $\alpha$ the planetary albedo, the dependence of OLR on $T_s$ is

linearized about the freezing point $T_f$ with constants $A$ and $B$, and the constant coefficient $D_s$ scales the equator-to-pole atmospheric heat transport.

We represent the wind-ice-ocean feedback in the model by setting the vertical heat flux between the two ocean layers to depend on the temperature difference with the coefficient

$$k = \begin{cases} k_{ice-covered}, & T_s \leq T_f, \\ k_{ice-free}, & T_s > T_f \end{cases} \tag{4.2}$$

with $k_{ice-covered} < k_{ice-free}$. The smaller vertical heat flux coefficient under subfreezing surface temperatures represents the effects of damped internal waves and reduced momentum input from the wind when sea ice is present.

The temperature of the SML ($T_{SML}$) is taken to be equal to the surface temperature as long as it is above the freezing point; with colder surface temperatures, the ocean is considered to be ice-covered, and the SML below the sea ice is taken to be at the freezing point:

$$T_{SML} = \begin{cases} T_f, & T_s \leq T_f, \\ T_s, & T_s > T_f. \end{cases} \tag{4.3}$$

Hence, the top layer evolves both the surface temperature and surface mixed layer temperature, and it includes a representation of atmospheric heat transport which is a function of the surface temperature. The temperature of the DL ($T_d$) is determined from the balance of horizontal heat transport in the DL, which is scaled by $D_d$, and the vertical heat flux between the two ocean layers:

$$c_d \frac{\partial T_d}{\partial t} = \underbrace{D_d \nabla^2 T_d}_{\text{horizontal transport}} + \underbrace{k\,(T_{SML} - T_d)}_{\text{vertical flux}}. \tag{4.4}$$

The heat capacities for the SML and DL are $c_s \equiv \rho\, c_p\, H_s$ and $c_d \equiv \rho\, c_p\, H_d$, respectively, where $H_s$ is the thickness of the SML, $H_d$ is the thickness of the DL, $\rho$ is the seawater density,

and $c_p$ is the seawater specific heat capacity.

To account for converging meridians on the sphere, the Laplacian operator in spherical coordinates is used for the horizontal diffusion in the SML and DL,

$$\nabla^2 = \frac{\partial}{\partial x}\left[(1-x^2)\frac{\partial}{\partial x}\right] \tag{4.5}$$

where $x \equiv \sin\theta$ with $\theta$ the latitude. We use as a boundary condition that there is no heat flux across the equator in either layer, which is consistent with an assumption that the annual-mean climate is hemispherically symmetric. This implies that $\frac{\partial T_{SML}}{\partial x} = \frac{\partial T_d}{\partial x} = 0$ at $x = 0$. As in previous EBM studies, we approximate the latitudinal variation in annual-mean incident solar radiation as $S = S_0 - S_2 x^2$, and we approximate the zenith angle dependence of the reflectivity of clouds by letting the planetary albedo similarly vary with latitude as $\alpha = \alpha_0 + \alpha_2 x^2$, with specified constants $S_0$, $S_2$, $\alpha_0$, and $\alpha_2$.

Many simplifications are made in the idealized process model in order to focus on the effects of the wind-ice-ocean feedback in isolation. However, we still expect that the inclusion of omitted features could have a substantial impact on this feedback and leave the study of these interactions to future work. For example, the model does not include seasonally-varying forcing, a representation of sea ice growth and ablation, or a representation of changes in albedo associated with the onset of icy surface conditions. Here, the surface temperature is allowed to cool below the freezing point, at which point the vertical heat flux coefficient decreases, but the SML temperature remains at the freezing point. Since the surface layer is taken to be well mixed, any heat gain or loss into the layer is instantly added to the surface temperature budget (Eq. 4.1). Therefore the only thing that changes in the model equations when the surface temperature drops below the freezing point is the jump in the vertical heat flux between the two layers.

Two approaches are used to solve the model 4.1-4.5. The first approach is to numerically integrate the system in time until a steady state is reached, using implicit Euler time–stepping and centered differencing in space (see Appendix A for details). This allows us to simulate the

time evolution of the system and provides a solution that is numerically stable for any time step size. The second approach is to use an approximate solution for the steady-state fields $T_s(x)$ and $T_d(x)$ written in terms of Legendre polynomial expansions (hereafter "steady-state solution"; see Appendix B for details). This allows us to solve for both stable and unstable model states. The results presented are calculated using numerical integration unless otherwise stated.

The default parameter values are adapted from previous EBM studies and chosen to give approximate qualitative agreement with observational estimates (Table 4.1).

**Table 4.1.** Model parameter values for the default parameter regime that approximately match observational estimates. Values for the alternative parameter regime in which hysteresis occurs are listed in parentheses and otherwise the same as the default parameter regime values. Both regimes are shown in Fig. 4.4 where $F$ is varied. In the alternative parameter regime, after $D_s$, $D_d$, and $k_{ice-covered}$ are chosen to increase the amount of hysteresis, the value of $A$ is tuned so that the sea ice edge is at a similar latitude to the default parameter regime when $F = 0$.

| Parameter | Default (Alternative) | Units |
|---|---|---|
| $c_s$ | 6.53 | W yr m$^{-2}$ K$^{-1}$ |
| $c_d$ | 78.4 | W yr m$^{-2}$ K$^{-1}$ |
| $\alpha_0$ | 0.3 | |
| $\alpha_2$ | 0.1 | |
| $S_0$ | 420 | W m$^{-2}$ |
| $S_2$ | 240 | W m$^{-2}$ |
| $A$ | 192 (177) | W m$^{-2}$ |
| $B$ | 2.1 | W m$^{-2}$ K$^{-1}$ |
| $D_s$ | 0.5 (0.1) | W m$^{-2}$ K$^{-1}$ |
| $D_d$ | 0.15 (0.5) | W m$^{-2}$ K$^{-1}$ |
| $k_{ice-free}$ | 5 | W m$^{-2}$ K$^{-1}$ |
| $k_{ice-covered}$ | 2 (1) | W m$^{-2}$ K$^{-1}$ |
| $T_f$ | -2 | °C |
| $F$ | 0 | W m$^{-2}$ |

## 4.4 Idealized Climate Model Results

Simulated fields under the default parameter regime are compared with observational estimates in Fig. 4.3a-c. Note, however, that given the idealized nature of the model, there is

substantial uncertainty in what specific parameter values provide the best point of contact with the real world. The parameter values that give rise to the temperature field that most closely resembles observations may not give rise to the most realistic response to forced heating due to compensating errors associated with omitted physical processes. The sensitivity of the model results to changes in the horizontal transport coefficients $D_s$ and $D_d$ is explored in Fig.4.3d-f.

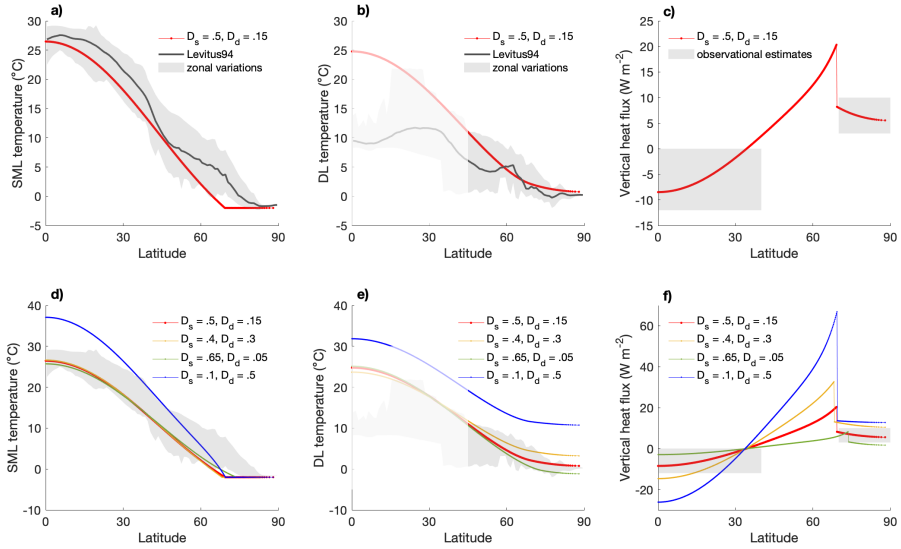


**Figure 4.3.** (a) Surface mixed layer (SML) temperature taken as the surface temperature in "ice-free" conditions and the freezing point in "ice-covered" conditions, (b) ocean deeper layer (DL) temperature, and (c) vertical heat flux between the two layers as a function of latitude. The model results using the default parameter regime are in red. In panels a and b, gray lines show climatology from Levitus94 (Levitus and Boyer, 1994), and gray shading represents zonal variations. In panel c, gray shading represents observational estimates of vertical ocean heat fluxes in the Arctic of 2 to 10 W $m^{-2}$ (Carmack et al., 2015; Peterson et al., 2017; Polyakov et al., 2017), and vertical ocean heat fluxes between 0 and 40 N of -12 to 0 W $m^{-2}$ (Cummins et al., 2016). The DL temperature south of 45 °N (faded) does not match well with observations since the model does not include equatorial upwelling and other processes. (d)-(f) As in panels (a)-(c), with the model output for the default parameter regime in red and observational estimates in gray shading, but including the model output for the alternative parameter regime in blue and two other parameter cases with varied values of $D_s$ and $D_d$. The two other parameter cases enclose the range of values of horizontal heat transport that most closely match the current climate. The values of $D_s$ are based on values of idealized model parameters similar to $D_s$ used in previous studies, and the values of $D_d$ are determined by comparing the model output to observational estimates.

### 4.4.1 Bistability and hysteresis

In the idealized climate model, the only differences between ice-free and ice-covered states are in the representations of the SML temperature and the vertical heat flux between the two ocean layers. When the surface temperature warms and crosses above the freezing point, the SML temperature is no longer fixed at $T_f$ but freely evolves (Eq. 4.3), and the vertical heat flux coefficient jumps from $k_{ice-covered}$ to $k_{ice-free}$.

We test for the possibility of bistability and hysteresis due to this nonlinear jump in vertical heat flux, as considered schematically in Fig. 4.1, by slowly ramping the climate forcing term $F$ up and then back down. We let the model spin up under constant forcing for 1000 years at the start of the simulation, and the forcing is then increased steadily from 0 to 10 W m$^{-2}$ over 15000 years. The same process is used when the forcing is ramped down from 10 to 0 W m$^{-2}$.

Using the default parameter regime (Table 4.1), which gives a simulated climate with $F = 0$ that is approximately consistent with observational estimates (Fig. 4.3a-c), we find that no hysteresis occurs (Fig. 4.4a-c). The sea ice edge displays an approximately linear retreat and growth when the forcing is ramped up and down. Next, we examine whether hysteresis can occur in other parameter regimes. Based on the schematic in Fig. 4.1, increasing the horizontal heat transport coefficient in the deep layer should make hysteresis more likely because it allows more heat supply to the deep polar ocean, and decreasing the horizontal heat transport coefficient in the surface layer should make hysteresis more likely because it reduces the influence of the subpolar surface ocean on the polar surface ocean. Hence we examine the simulated climate in an alternative parameter regime that has an increased value of $D_d$ and a decreased value of $D_s$. In this alternative parameter regime we also reduce the vertical heat flux coefficient when ice is present in order to enhance the jump in heat flux when the climate is varied. The alternative parameter values are listed in parentheses in Table 4.1.

We find that a striking hysteresis occurs in this alternative parameter regime (Fig. 4.4d-f). The steady-state solution (black solid and dashed lines in Fig. 4.4d) indicates that there is an

unstable climate state for climate forcing values between around $F = 4.5$ Wm$^{-2}$ and $F = 6.5$ Wm$^{-2}$. The bifurcation points at the edge of this range coincide with the edges of the hysteresis loop in the numerical solution. The spatial structures of the temperature and horizontal heat transport in each model layer, as well as the vertical heat flux between the layers, are shown in Fig. 4.5 for the cold and warm states under the same climate forcing. The state with a warmer surface temperature in high latitudes clearly has a colder deep layer temperature in high latitudes, as anticipated in the conceptual sketch (Fig. 4.1). And although it is difficult to discern in Fig. 4.5, the state with a warmer high-latitude surface temperature has a slightly colder surface temperature in lower latitudes (note that this small temperature difference is not indicated in the schematic in Fig. 4.1). This is because the bistability involves only heat transport feedbacks and not radiative feedbacks. Thus, the global-mean outgoing longwave radiation needs to be the same in both states, which in this idealized model implies the same global-mean surface temperature. This feature of the two states is in contrast to bistability brought on by the ice-albedo feedback or other radiative feedbacks.

Note that in the default parameter regime, atmospheric and oceanic heat transport have a meridional maximum of 3.2 PW and 0.8 PW, respectively, which is approximately in line with the partitioning of heat transport from observational estimates and other EBM-style models (e.g. Armour et al., 2019). However, the partitioning of heat transport is different in the alternative parameter regime where hysteresis occurs (Fig. 4.5c,f).

Next, we consider many values for the horizontal heat transport coefficients in the surface and deep layers. For each set of coefficients, we compute the width of the hysteresis loop ($\Delta F$ indicated in Fig. 4.4d) using the steady-state solution of the model. Here, $\Delta F$ is computed as the maximum forcing at which the model can have ice (first saddle-node bifurcation) minus the minimum forcing at which the model can be ice-free (second saddle-node bifurcation); $\Delta F = 0$ in simulations with no hysteresis. The results are shown in Fig. 4.6.

The occurrence of a bifurcation in some parameter regimes is meaningful because it signifies that in those regimes there is a range of forcing values for which there exist two stable

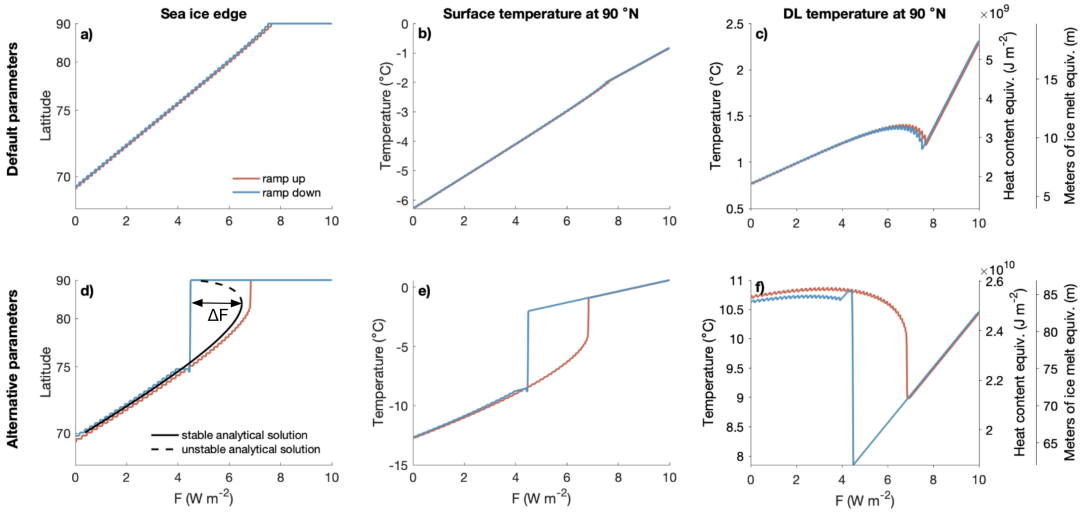


**Figure 4.4.** Sea ice edge latitude and polar temperature in the two layers when the forcing is slowly ramped up and then ramped down. (a) The sea ice edge latitude, defined as the location at which $T_s = T_f$, when $F$ is increased from 0 to 10 W m$^{-2}$ (ramp-up, shown in red) and when $F$ is decreased from 10 to 0 W m$^{-2}$ (ramp-down, shown in blue). (b,c) The same but for $T_s$ and $T_d$ at 90°N. The top row shows the results under the default parameter regime, and the bottom row shows the results under an alternative parameter regime where hysteresis occurs (values listed in parentheses Table 4.1). The vertical axis in panels (a,d) is scaled to be linear in sea ice area. The solid and dashed black line in panel (d) show the stable and unstable states in the steady-state solution for the model.

climate states with different sea ice edges under the same greenhouse forcing. During forced warming or cooling, an abrupt jump between the two states occurs when the bifurcation point (or "tipping point") is crossed.

### 4.4.2 Storage and release of heat

The simulated DL has a more horizontally-uniform temperature distribution than the SML, with the DL being colder than the SML in low latitudes and warmer than the SML in high latitudes (Fig. 4.3). As can be inferred from Eq. 4.4, the global-mean temperature of the DL would be equal to the SML if $k$ were globally uniform, but variations in $k$ cause an offset between the temperatures of the two layers.

The temperature of the DL tends to rise with increasing climate forcing $F$. However,

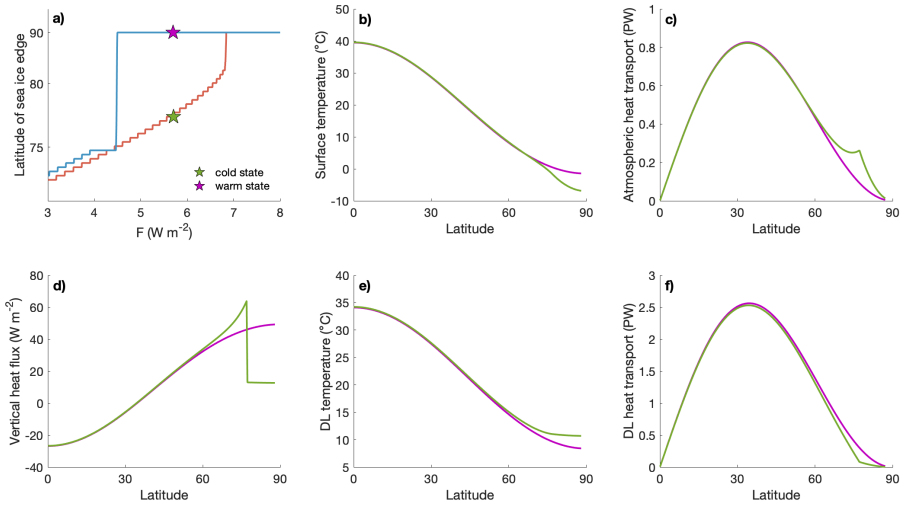


**Figure 4.5.** Temperature and heat transport for the two stable climate states. (a) Sea ice edge (latitude where $T_s = T_f$) in the model under the alternative parameter regime when the forcing $F$ is slowly ramped up and ramped down, as in Fig. 4.4d but using a narrower range of forcing values. The two stars indicate two stable climate states under the same forcing $F = 5.7$ Wm$^{-2}$: a cold state (green star) and a warm state (pink star). (b) Surface temperature ($T_s$), (c) atmospheric meridional heat transport, (d) vertical heat flux between the two layers, (e) DL temperature ($T_d$), and (f) DL meridional heat transport; the spatial structure of each of these fields is plotted for the cold state (green curves) and warm state (pink curves) with $F = 5.7$ Wm$^{-2}$.

at high-latitude locations where the surface becomes ice free ($T_s > T_f$), the mixing coefficient increases so that more heat is transported out of the DL and into the colder SML above. This causes the DL temperature in high latitudes to drop as the model approaches an ice-free state. In the alternative parameter regime which has hysteresis, there is a sudden drop in the DL temperature when warming causes the model to cross the bifurcation point, with an associated release of heat equivalent to about 15 m of ice melt (Fig. 4.4f). In the default parameter regime which has no hysteresis, there is no sudden drop in the DL temperature, but there is still a gradual decrease in DL temperature, with a release of heat equivalent to about 2 m of ice melt (Fig. 4.4c). This implies that even in the absence of hysteresis, the change in the vertical mixing coefficient can lead to enough heat being released from the DL to dramatically melt the sea ice.

In both cases, this is only a small fraction of the total heat stored in the DL, which has the potential to melt 10-85 meters of ice depending on the model parameters. We find this to be

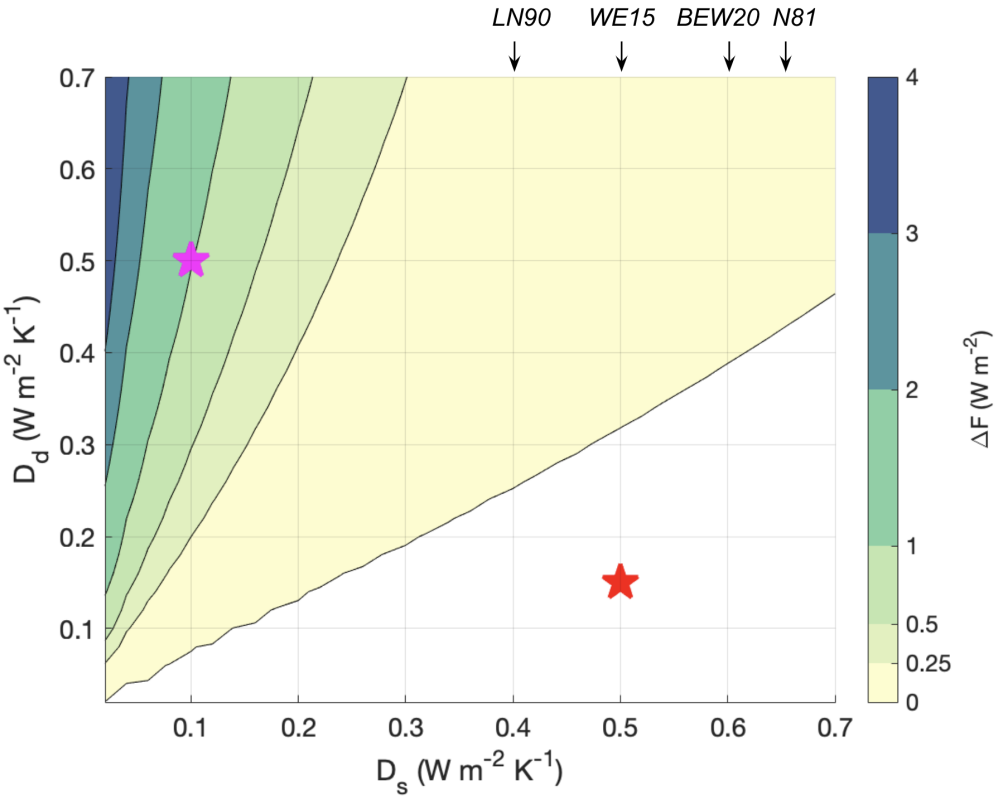


**Figure 4.6.** Level of hysteresis when the horizontal heat transport coefficients $D_s$ and $D_d$ are varied. Other parameters are set to their default values (Table 4.1). Here hysteresis is measured as the range of forcing values with bistability, $\Delta F$, using the steady-state solution as indicated in Fig. 4.4d. The values of $D_s$ and $D_d$ used in the default parameter regime and the alternative parameter regime are indicated by the red and magenta stars, respectively. Note that the level of hysteresis indicated by the magenta star is different from the level of hysteresis in Fig. 4.4d due to different $k_{ice-covered}$ values. Values for $D_s$ used in previous studies with idealized models that had a similar surface layer are indicted by arrows along the top of the figure [LN90 is Lin and North (1990); WE15 is Wagner and Eisenman (2015); BEW20 is Beer et al. (2020); and N81 is North et al. (1981)].

true for a range of parameter values that produce hysteresis. To demonstrate this, we measure the fraction of heat lost in the DL, $H = (T_d^{max} - T_d^{min})/T_d^{max}$, where $T_d^{max}$ is the DL temperature maximum before the bifurcation and $T_d^{min}$ is the DL temperature minimum after the bifurcation. We then compare the heat loss percentage ($H$) to the amount of hysteresis ($\Delta F$), and we vary the horizontal and vertical heat transport coefficients, starting from a parameter regime which allows hysteresis. A larger value of $D_d$ or a smaller value of $D_s$ both lead to more hysteresis, as does a

larger vertical heat transport coefficient in ice-free conditions (Fig. 4.7d-f). However, there is no consistent relationship between the amount of hysteresis and the percentage of stored heat released. The percentage of stored heat that is released increases for larger values of $k_{ice-free}$, decreases for larger values $D_d$, and remains largely unaffected by variations $D_s$ (Fig. 4.7a). Nonetheless, the small fraction of heat that is lost from the DL when the system crosses the bifurcation point in a ramp-up simulation is striking.

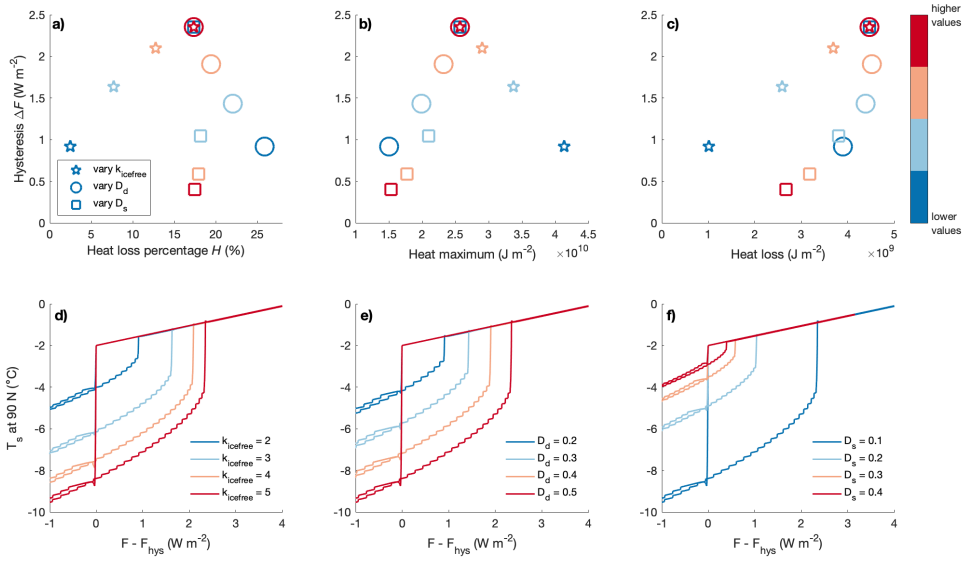


**Figure 4.7.** Top panels: Hysteresis width $\Delta F$ versus (a) the percentage of heat lost $H$ from the DL, (b) the heat maximum before the bifurcation in the DL, and (c) the heat loss from the DL during the bifurcation for simulations in a number of different parameter regimes. Star symbols indicate simulations where $k_{ice-free}$ is varied and all other parameters are set to the values indicated in parenthesis in Table 4.1. Circles and squares indicate simulations with varied $D_d$ and $D_s$. The specific values of $k_{ice-free}$, $D_d$, $D_s$ are specified in panels d, e, and f, and identified with the same color in panels a, b, and c. Bottom panels: The surface temperature at 90°N when forcing is ramped up and ramped down in the alternative parameter regime ($k_{ice-free} = 5$, $D_d = 0.5$, $D_s = 0.1$) and using 3 other values of (d) $k_{ice-free}$, (e) $D_d$, and (f) $D_s$ (values indicated are in W m$^{-2}$ K$^{-1}$). The horizontal axis shows the forcing anomaly relative to the value of $F$ at which the first bifurcation occurs, $F_{hys}$.

How relative heat loss varies with these parameters can be understood by considering the DL heat maximum before the bifurcation point and the amount of heat loss (Fig. 4.7b,c). A larger value of $k_{ice-free}$ leads to a smaller heat maximum in the DL due to increased vertical

heat transport. It also leads to a larger heat loss, and therefore a larger heat loss percentage. A larger value of $D_d$ leads to a larger heat maximum in the DL but minimal change in the amount of heat lost, and therefore a smaller heat loss percentage. A smaller value of $D_s$ sustains a larger temperature difference between the two layers at the pole, which leads to a larger heat maximum in the DL and a larger heat loss, so its heat loss percentage remains largely unchanged.

### 4.4.3 Caveats

The current study describes a highly idealized model, which is intended to isolate a single process. There are caveats in interpreting results from this idealized system in the context of a world with numerous interacting processes. For example, the model only represents annual-mean temperature. In the case of the surface albedo feedback, including a seasonal cycle diminishes the degree of hysteresis (Wagner and Eisenman, 2015). However, the role of the seasonal cycle is less straightforward in the case of vertical mixing, for which winter storms have a large effect. Furthermore, we only consider steady-state climates in our analysis. The change in heat storage does not directly correspond with sea ice volume loss in steady-state climates, in contrast with transient climate changes. For example, when changing only the depth of the DL in the steady-state analysis, the amount of heat storage is altered, as is the heat loss when transitioning to an ice-free state. However, the heat loss percentage remains unchanged, as does the amount of hysteresis and the change in the DL temperature, which we focus on in the present analysis.

Given the simple representations of heat transport in the atmosphere and ocean, the values of the heat transport coefficients are not well constrained. Previous studies have used a similar representation for primarily atmospheric heat transport, and we use these to guide the value of $D_s$. However, since the two-layer model presented in this paper includes heat transport in the lower layer, it would be reasonable to use a lower value of $D_s$ compared with previous one-layer models. The value of $D_d$ is tuned so that the model output approximately matches observations. However, the DL temperature does not match well in low latitudes. It is therefore plausible that a larger value of $D_d$ would be more appropriate. This could have implications for a possible

hysteresis, and we explore the impacts of variations in the values of $D_s$ and $D_d$ for two further parameter cases in Fig. 4.3d-f (as discussed above). For one of the two variations ($D_s = 0.4$, $D_d = 0.3$), hysteresis occurs.

## 4.5 Summary and Discussion

In this study, we use an idealized model of the global climate to investigate the possible impacts of a proposed "wind-ice-ocean feedback" between retreating sea ice and enhanced ocean mixing. This has consequences for the release of heat stored in the deep Arctic Ocean, causing the sea ice retreat to accelerate. We find this feedback can cause a novel bistability in the climate system, with an associated hysteresis occurring under forced warming and cooling. The hysteresis loop is characterized by an abrupt and irreversible transition to ice-free conditions when the bifurcation point is crossed during gradual forced warming.

However, we find that hysteresis occurs in only a limited range of the model parameter space. For the parameter regime that gives rise to temperatures that most closely resemble the current climate, hysteresis does not occur. This could imply that bistable regimes only occur for climates with unrealistic deep water temperatures and heat transports, but note that given the idealized nature of the model, the parameter regime that gives rise to the most realistic temperature distribution may not give rise to the most realistic response to forced heating. Hence we conclude that hysteresis is possible in principle due to this feedback, but we are not able to determine whether this hysteresis can occur in the real world. The reversibility of Arctic sea ice loss has been investigated in comprehensive climate models, and no evidence of hysteresis has been found (Armour et al., 2011; Li et al., 2013). However, the wind-ice-ocean feedback may not be well represented in these models (even if it is present in the physical ocean) due to the limits of coarse-resolution mixing parameterizations and poorly resolved upper-ocean processes in the Arctic Ocean. For example, Manucharyan and Thompson (2022) suggest that such coarse-resolution climate models may not capture the changes in the dissipation of eddies

under sea ice retreat. In a higher-resolution model, they found that sea ice loss reduced the dissipation of upper-ocean eddies, allowing more subsurface heat to be brought into the mixed layer and creating a positive feedback. Thus, high-resolution models could be used to further explore this feedback.

A consequence of hysteresis is the abrupt release of heat from the subsurface layer, which has enough heat to melt 10s of meters of sea ice. However, even without hysteresis, the wind-ice-ocean feedback enhances vertical mixing in the Arctic Ocean, which leads to a decrease in the subsurface temperature. In the parameter regime that gives rise to temperatures that most closely resemble the current climate, this reduction of heat is equivalent to about 2 m of ice melt.

We find that even though there is enough heat in the deep Arctic Ocean to melt all the Arctic sea ice many times over, only a small fraction of the stored heat is released during warming, whether or not hysteresis occurs. This suggests the current amount of heat stored in the Atlantic Water layer in the deep Arctic Ocean is not a good indicator of how much subsurface heat will reach the surface as the Arctic sea ice retreats. We furthermore show that the percentage of heat lost from the deep Arctic Ocean is not robustly related to the amount of hysteresis in the model.

By caveat, there are many aspects of the climate that could influence this feedback but are not included in the present idealized model. For example, it is possible that increased river runoff or net precipitation changes in a warming climate could lead to an increase in salinity stratification in the Arctic Ocean, which would further isolate heat in the DL and could mask the effects of this feedback (as reviewed in Timmermans and Marshall, 2020). On the other hand, we also omit the surface albedo feedback, which could plausibly work together with the proposed positive feedback to accelerate sea ice decline. Therefore, work using more complex models and observations is called for to further investigate how this feedback interacts with the rest of the climate system.

## 4.6 Acknowledgments

Thanks to Tim Merlis, Nicole Shibley, Marion Alberty, and Jen MacKinnon for helpful discussions and also to two anonymous reviewers for helpful comments. This work was supported by National Science Foundation grant OCE-2048590. The Levitus94 data used in Fig. 4.2b and Fig. 4.3 was downloaded online (from http://iridl.ldeo.columbia.edu). The model code is available on GitHub (at https://github.com/emma-beer/two-ocean-layer-EBM-2022).

Chapter 4, in full, is a reprint of the material as it appears in Journal of Physical Oceanography, 2023. Beer, E., I. Eisenman, T. J. W. Wagner, and E. C. Fine, 2023: A Possible Hysteresis in the Arctic Ocean due to Release of Subsurface Heat during Sea Ice Retreat. *Journal of Physical Oceanography*, **53(5)**, 1323–1335. The dissertation author was the primary investigator and author of this paper.

## 4.7 Appendix A: Model Numerics

We numerically integrate the system in Eqs. 4.1-4.5 using implicit Euler time–stepping and centered differencing in space.

### 4.7.1 Implicit Euler time-stepping

Using implicit Euler time-stepping (with time index $n$), Eqs. 4.1-4.4 can be written as,

$$k^n = \begin{cases} k_{ice-free} & T_s^n > T_f \\ k_{ice-covered} & T_s^n \leq T_f \end{cases}, \tag{4.6}$$

$$T_s^{n+1} - T_s^n = \frac{\Delta t}{c_s}\Big[C - M_s^n(T_s^{n+1} - T_f) + N_s^n(T_d^{n+1} - T_f)\Big], \tag{4.7}$$

$$T_d^{n+1} - T_d^n = \frac{\Delta t}{c_d}\Big[ - M_d^n(T_d^{n+1} - T_f) + N_d^n(T_s^{n+1} - T_f)\Big]. \tag{4.8}$$

In Eq. 4.7, we have defined the vector $C \equiv (1 - \mathrm{diag}(\alpha))\, S - A + F$ and matrices $M_s^n =$

$BI - D_s\Lambda + \text{diag}(K^n)$ and $N_s^n = \text{diag}(k^n)$, where

$$K^n \equiv \begin{cases} k^n & T_s^n > T_f \\ 0 & T_s^n \leq T_f \end{cases},$$

$I$ is the identity matrix, and $\Lambda \equiv \partial_x[(1-x^2)\partial_x]$ is the diffusion operator. The operator $\text{diag}(v)$ constructs a diagonal matrix with the vector $v$ along the main diagonal. Similarly in Eq. 4.8, we have defined the matrices $M_d^n \equiv -D_d\Lambda + \text{diag}(k^n)$ and $N_d^n = \text{diag}(K^n)$.

The temperatures at time $n+1$ can then be calculated as

$$T_s^{n+1} - T_f = \left[I + \frac{\Delta t}{c_s}M_s^n - \frac{\Delta t^2}{c_s c_d}N_s^n\left(I + \frac{\Delta t}{c_d}M_d^n\right)^{-1}N_d^n\right]^{-1}\left[T_s^n - T_f + \frac{\Delta t}{c_s}C + \frac{\Delta t}{c_s}N_s^n\left(I + \frac{\Delta t}{c_d}M_d^n\right)^{-1}(T_d^n - T_f)\right], \quad (4.9)$$

$$T_d^{n+1} - T_f = \left(I + \frac{\Delta t}{c_d}M_d^n\right)^{-1}\left[T_d^n - T_f + \frac{\Delta t}{c_d}N_d^n(T_s^{n+1} - T_f)\right]. \quad (4.10)$$

With $C \equiv (1 - \text{diag}(\alpha))\,S - A + F$ and matrices $M_s^n = BI - D_s\Lambda + \text{diag}(K^n)$, $N_s^n = \text{diag}(k^n)$, $M_d^n \equiv -D_d\Lambda + \text{diag}(k^n)$ and $N_d^n = \text{diag}(K^n)$ where $I$ is the identity matrix, and $\Lambda \equiv \partial_x[(1-x^2)\partial_x]$ is the diffusion operator.

### 4.7.2 Diffusion operator with central difference

We use a central difference spatial derivative stencil for the diffusion operator (Eq. 4.5). The model output and diffusion operator are defined on staggered grids. Using a first-order central difference scheme (spatial grid points indexed with $i$), $\frac{\partial T}{\partial x}$ can be written as:

$$\left(\frac{\partial T}{\partial x}\right)_i = \frac{T_{i+1/2} - T_{i-1/2}}{\Delta x}. \quad (4.11)$$

Next, we define $\gamma_i \equiv (1 - x_i^2)\frac{T_{i+1/2} - T_{i-1/2}}{\Delta x}$. Using another first-order central difference

scheme, $\frac{\partial \gamma}{\partial x}$ can be written as:

$$\left(\frac{\partial \gamma}{\partial x}\right)_i = \frac{1}{\Delta x^2}\left\{\left(1-x_{i+1/2}^2\right)T_{i+1} - \left[\left(1-x_{i+1/2}^2\right)+\left(1-x_{i-1/2}^2\right)\right]T_i + \left(1-x_{1-1/2}^2\right)T_{i-1}\right\}. \tag{4.12}$$

Finally, we construct a diffusion operator matrix $\Lambda$ to act on $T$ with:

$$\Lambda_{i,i-1} = \frac{1}{\Delta x^2}\left(1-x_{i-1/2}^2\right), \tag{4.13}$$

$$\Lambda_{i,i} = \frac{1}{\Delta x^2}\left[\left(1-x_{i-1/2}^2\right)+\left(1-x_{i+1/2}^2\right)\right], \tag{4.14}$$

$$\Lambda_{i,i+1} = \frac{1}{\Delta x^2}\left(1-x_{i+1/2}^2\right). \tag{4.15}$$

## 4.8 Appendix B: Model Steady-state Solution using Legendre Polynomial Expansions

We calculate an approximate steady-state solution by expressing the temperature as an expansion of Legendre polynomials. Using Legendre polynomials is not essential to obtaining a steady-state solution, which could alternatively be done by inverting the diffusion operator matrices to get a solution of the spatially gridded algebraic equations, but it reduces the computation time substantially. To do this, we rewrite the jump in the vertical heat flux coefficient as a function of the ice edge latitude $x_s$ and use Legendre polynomial identities to write an expression for the surface temperature. Since the surface temperature is at the freezing point at the ice edge, the forcing can then be calculated as a function of the ice edge latitude. An expansion of Legendre polynomials needs to then be calculated at each individual ice edge latitude, which is somewhat different from previous EBM solutions that included a surface albedo feedback but not a second layer (North et al., 1981).

First we rewrite Eqs. 4.1-4.5 in equilibrium with $x_s$ defined as the latitude where $T_s = T_f$:

$$0 = \left[1-\alpha(x)\right]S(x) - A - B\left[T_s(x) - T_f\right] + D_s\partial_x\left[(1-x^2)\partial_x T_s(x)\right] + k(x,x_s)\left[T_d(x) - T_{SML}(x,x_s)\right] + F, \quad (4.16)$$

$$0 = D_d\partial_x\left[(1-x^2)\partial_x T_d(x)\right] + k(x,x_s)\left[T_{SML}(x,x_s) - T_d(x)\right]. \quad (4.17)$$

$$\text{with} \quad k = \begin{cases} k_{ice-covered}, & x > x_s, \\ k_{ice-free}, & x \le x_s, \end{cases} \quad \text{and} \quad T_{SML} = \begin{cases} T_f, & x > x_s, \\ T_s(x), & x \le x_s. \end{cases} \quad (4.18)$$

Next we introduce solutions to $T_s$ and $T_d$ as a sum of Legendre polynomials $P_n$:

$$T_s(x) - T_f = \sum_{n\ even} T_n P_n(x), \quad T_d(x) - T_f = \sum_{n\ even} V_n P_n(x). \quad (4.19)$$

Next we multiply Eqs. 4.16 and 4.17 by $(2m+1)P_m(x)$ and integrate between 0 and 1, using the definitions in Eq. 4.19 and orthogonality relation to simplify:

$$0 = \delta_{0,m}(F-A) + L_m - BT_m - m(m+1)D_sT_m + (2m+1)\sum_{n\ even} V_n \int_0^1 k(x,x_s)P_n(x)P_m(x)dx - (2m+1)\sum_{n\ even} T_n \int_0^{x_s} k(x,x_s)P_n(x)P_m(x)dx, \quad (4.20)$$

$$0 = -m(m+1)D_dV_m + (2m+1)\sum_{n\ even} T_n \int_0^{x_s} k(x,x_s)P_n(x)P_m(x)dx - (2m+1)\sum_{n\ even} V_n \int_0^1 k(x,x_s)P_n(x)P_m(x)dx, \quad (4.21)$$

$$\text{with} \quad L_m = (2m+1)\int_0^1 [1-\alpha(x)]S(x)P_m(x)dx. \quad (4.22)$$

Next we insert the definition of $k$ (4.18) into Eqs. 4.20-4.22 and simplify:

$$0 = \delta_{0,m}(F - A) + L_m - BT_m - m(m+1)D_sT_m + k_{ice-covered}V_m + \sum_{n\ even} \left[\Delta k V_n - k_{ice-free}T_n\right] I_m^n(x_s), \tag{4.23}$$

$$0 = -m(m+1)D_dV_m - k_{ice-covered}V_m + \sum_{n\ even} \left[k_{ice-free}T_n - \Delta k V_n\right] I_m^n(x_s), \tag{4.24}$$

$$\text{where} \quad \Delta k = k_{ice-free} - k_{ice-covered} \quad \text{and} \quad I_m^n(x_s) = (2m+1)\int_0^{x_s} P_n(x)P_m(x)dx. \tag{4.25}$$

We truncate at $n = 80$ and solve for $T_m(x_s, F)$, $V_m(x_s, F)$. Then the surface temperature can be written as

$$T_s(x) - T_f = \sum_{m\ even}^{80} T_m(x_s, F)P_m(x). \tag{4.26}$$

Using that $T_s = T_f$ at $x = x_s$, we are left with the expression

$$0 = \sum_{m\ even}^{80} T_m(x_s, F)P_m(x_s). \tag{4.27}$$

We can then solve for $F(x_s)$. Because the solution for $T_m$ includes a sum over index $n$, an expansion of Legendre polynomials needs to be calculated at each ice edge latitude, $x_s$, as noted above.

# Chapter 5

# Conclusion

The processes that contribute to the Arctic amplification of global surface warming are often described in the context of climate feedbacks. Previous studies have used a traditional feedback analysis framework to partition the regional surface warming into contributions from each feedback process. However, this partitioning does not account for interactions between feedbacks and with atmospheric heat transport. In Chapter 2, we instead inactivated individual feedback processes during forced warming and evaluated the resulting change in the surface temperature field, thereby allowing interactions between processes. The results are strikingly different from previous feedback analyses. Specifically, we found that the water vapor feedback is the largest contributor to Arctic amplification and that the lapse rate feedback has a roughly even contribution to cooling in the tropical and Arctic regions. In contrast, previous analyses found the lapse rate feedback to be the largest contributor to and the water vapor feedback to be the largest opposer of Arctic amplification when considering feedbacks in isolation. This highlights the importance of comparing different methods in order to build a better understanding of how feedbacks influence climate change.

A range of mechanisms have been proposed to contribute to the Arctic amplification of global warming, which typically involve atmospheric and surface processes. However, substantial questions remain regarding the role of ocean heat transport. In Chapter 3, we investigated changes in oceanic heat fluxes and associated impacts on Arctic amplification using an idealized ocean-sea

ice-climate model of the Northern Hemisphere. We showed that beneath the sea ice, vertical temperature gradients across the halocline increase as the ocean warms since the surface mixed layer temperatures in ice-covered regions are fixed near the freezing point. These enhanced vertical temperature gradients drive enhanced horizontal heat transport into the Arctic region and can contribute substantially to Arctic amplification. Using a feedback-locking approach, we quantified this mechanism to contribute 20% to Arctic amplification in the idealized model. A similar increase in ocean heat transport under global warming has been identified previously in GCM simulations, but the physical mechanism remained elusive. The mechanism presented here may provide an explanation for this behavior.

It is estimated that the heat stored in the subsurface layers of the Arctic Ocean is enough to melt all the Arctic sea ice many times over. Current vertical mixing rates in the upper Arctic Ocean are small, but recent observational studies have argued that sea ice retreat could result in enhanced ocean mixing. In Chapter 4, we expanded on our previous idealized ocean-sea ice-climate model to investigate the impacts of a positive feedback whereby increased vertical mixing due to sea ice retreat causes the previously isolated subsurface heat to melt more sea ice. We found this feedback can cause a bistability in the climate system, with an associated hysteresis characterized by an abrupt release of heat from the subsurface layer and an irreversible transition to ice-free conditions. The hysteresis occurs in only a limited range of the model parameter space, and does not occur for the parameter regime that gives rise to temperatures that most closely resemble the current climate. However, given the idealized nature of the model, the parameter regime that gives rise to the most realistic temperature distribution may not give rise to the most realistic behaviour. Hence, we conclude that hysteresis is possible in principle due to this feedback, but we are not able to determine whether this hysteresis occurs in the real world.

This thesis demonstrates the use of idealized models to explore physical mechanisms that can not be readily investigated in comprehensive climate models, and it assesses the possible implications resulting from them. We hope to motivate work in combination with observations and models to further investigate their impact on the Arctic response to global warming.

# References


Aagaard, K., L. Coachman, and E. Carmack, 1981: On the halocline of the Arctic Ocean. *Deep-Sea Research Part A-Oceanographic Research Papers*, **28 (6)**, 529–&, doi:{10.1016/0198-0149(81)90115-1}.

Alexeev, V., P. Langen, and J. Bates, 2005: Polar amplification of surface warming on an aquaplanet in "ghost forcing" experiments without sea ice feedbacks. *Climate Dynamics*, **24 (7-8)**, 655–666, doi:{10.1007/s00382-005-0018-3}.

Alexeev, V. A., and C. H. Jackson, 2013: Polar amplification: is atmospheric heat transport important? *Climate Dynamics*, **41 (2)**, 533–547, doi:{10.1007/s00382-012-1601-z}.

Amante, C., and B. W. Eakins, 2009: ETOPO1 arc-minute global relief model: procedures, data sources and analysis. *NOAA Technical Memorandum NESDIS NGDC-24*.

Ardyna, M., M. Babin, M. Gosselin, E. Devred, L. Rainville, and J.-E. Tremblay, 2014: Recent Arctic Ocean sea ice loss triggers novel fall phytoplankton blooms. *Geophysical Research Letters*, **41 (17)**, 6207–6212, doi:{10.1002/2014GL061047}.

Armour, K. C., C. M. Bitz, and G. H. Roe, 2013: Time-varying climate sensitivity from regional feedbacks. *Journal of Climate*, **26 (13)**, 4518–4534, doi:{10.1175/JCLI-D-12-00544.1}.

Armour, K. C., I. Eisenman, E. Blanchard-Wrigglesworth, K. E. McCusker, and C. M. Bitz, 2011: The reversibility of sea ice loss in a state-of-the-art climate model. *Geophysical Research Letters*, **38**, doi:10.1029/2011GL048739.

Armour, K. C., N. Siler, A. Donohoe, and G. H. Roe, 2019: Meridional atmospheric heat transport constrained by energetics and mediated by large-scale diffusion. *Journal of Climate*, **32 (12)**, 3655–3680, doi:{10.1175/JCLI-D-18-0563.1}.

Arthun, M., T. Eldevik, L. H. Smedsrud, O. Skagseth, and R. B. Ingvaldsen, 2012: Quantifying the influence of Atlantic heat on Barents sea ice variability and retreat. *Journal of Climate*, **25 (13)**, 4736–4743, doi:{10.1175/JCLI-D-11-00466.1}.

Beer, E., I. Eisenman, and T. J. W. Wagner, 2020: Polar amplification due to enhanced heat flux

across the halocline. *Geophysical Research Letters*, **47 (4)**, doi:{10.1029/2019GL086706}.

Bitz, C., P. Gent, R. Woodgate, M. Holland, and R. Lindsay, 2006: The influence of sea ice on ocean heat uptake in response to increasing CO2. *Journal of Climate*, **19 (11)**, 2437–2450, doi:{10.1175/JCLI3756.1}.

Bonan, D. B., K. C. Armour, G. H. Roe, N. Siler, and N. Feldl, 2018: Sources of uncertainty in the meridional pattern of climate change. *Geophysical Research Letters*, **45 (17)**, 9131–9140, doi:{10.1029/2018GL079429}.

Budyko, M., 1969: Effect of solar radiation variations on climate of Earth. *Tellus*, **21 (5)**, 611–&.

Cai, M., 2006: Dynamical greenhouse-plus feedback and polar warming amplification. Part I: A dry radiative-transportive climate model. *Climate Dynamics*, **26 (7-8)**, 661–675, doi:{10.1007/s00382-005-0104-6}.

Cai, M., and J. Lu, 2009: A new framework for isolating individual feedback processes in coupled general circulation climate models. Part II: Method demonstrations and comparisons. *Climate Dynamics*, **32 (6)**, 887–900, doi:{10.1007/s00382-008-0424-4}.

Carmack, E., I. Polyakov, L. Padman, I. Fer, E. Hunke, J. Hutchings, J. Jackson, D. Kelley, R. Kwok, C. Layton, H. Melling, D. Perovich, O. Persson, B. Ruddick, M. L. Timmermans, J. Toole, T. Ross, S. Vavrus, and P. Winsor, 2015: Toward quantifying the increasing role of oceanic heat in sea ice loss in the new Arctic. *Bulletin of the American Meteorological Society*, **96 (12)**, 2079–2105, doi:{10.1175/BAMS-D-13-00177.1}.

Cess, R., G. Potter, M. Zhang, J. Blanchet, S. Chalita, R. Colman, D. Dazlich, A. Delgenio, V. Dymnikov, V. Galin, D. Jerrett, E. Keup, A. Lacis, H. Letruet, X. Liang, J. Mahfouf, B. McAvaney, V. Meleshko, J. Mitchell, J. Morcrette, P. Norris, D. Randall, L. Rikus, E. Roeckner, J. Royer, U. Schlese, D. Sheinin, J. Slingo, A. Sokolov, K. Taylor, W. Washington, R. Wetherald, and I. Yagai, 1991: Interpretation of snow-climate feedback as produced by 17 general-circulation models. *Science*, **253 (5022)**, 888–892, doi:{10.1126/science.253.5022.888}.

Cole, S. T., J. M. Toole, L. Rainville, and C. M. Lee, 2018: Internal waves in the Arctic: Influence of ice concentration, ice roughness, and surface layer stratification. *Journal of Geophysical Research-Oceans*, **123 (8)**, 5571–5586, doi:{10.1029/2018JC014096}.

Collins, M., R. Knutti, J. Arblaster, J.-L. Dufresne, T. Fichefet, P. Friedlingstein, X. Gao, W. Gutowski, T. Johns, G. Krinner, M. Shongwe, C. Tebaldi, A. Weaver, and M. Wehner, 2013: Long-term climate change: Projections, commitments and irreversibility. *Climate Change 2013: The Physical Science Basis. Contribution of Working Group I to the Fifth Assessment Report of the Intergovernmental Panel on Climate Change*, T. Stocker, D. Qin, G.-K. Plattner, M. Tignor, S. Allen, J. Boschung, A. Nauels, Y. Xia, V. Bex, and P. M. (eds.), Eds., Cambridge

University Press, Cambridge, United Kingdom and New York, NY, USA, book section 12, 1029–1136, doi:10.1017/CBO9781107415324.024, URL www.climatechange2013.org.

Cummins, P. F., D. Masson, and O. A. Saenko, 2016: Vertical heat flux in the ocean: Estimates from observations and from a coupled general circulation model. *Journal of Geophysical Research-Oceans*, **121 (6)**, 3790–3802, doi:{10.1002/2016JC011647}.

D'Asaro, E., and J. Morison, 1992: Internal waves and mixing in the Arctic-Ocean. *Deep-Sea Research Part A-Oceanographic Research Papers*, **39 (2A, S)**, S459–S484, doi:{10.1016/S0198-0149(06)80016-6}.

Davis, P. E. D., C. Lique, H. L. Johnson, and J. D. Guthrie, 2016: Competing effects of elevated vertical mixing and increased freshwater input on the stratification and sea ice cover in a changing Arctic Ocean. *Journal of Physical Oceanography*, **46 (5)**, 1531–1553, doi:{10.1175/JPO-D-15-0174.1}.

Dee, D. P., S. M. Uppala, A. J. Simmons, P. Berrisford, P. Poli, S. Kobayashi, U. Andrae, M. A. Balmaseda, G. Balsamo, P. Bauer, P. Bechtold, A. C. M. Beljaars, L. van de Berg, J. Bidlot, N. Bormann, C. Delsol, R. Dragani, M. Fuentes, A. J. Geer, L. Haimberger, S. B. Healy, H. Hersbach, E. V. Holm, L. Isaksen, P. Kallberg, M. Koehler, M. Matricardi, A. P. McNally, B. M. Monge-Sanz, J. J. Morcrette, B. K. Park, C. Peubey, P. de Rosnay, C. Tavolato, J. N. Thepaut, and F. Vitart, 2011: The ERA-Interim reanalysis: configuration and performance of the data assimilation system. *Quarterly Journal of the Royal Meteorological Society*, **137 (656, A)**, 553–597, doi:{10.1002/qj.828}.

Dosser, H. V., M. Chanona, S. Waterman, N. C. Shibley, and M. L. Timmermans, 2021: Changes in internal wave-driven mixing across the Arctic Ocean: Finescale estimates from an 18-year pan-arctic record. *Geophysical Research Letters*, **48 (8)**, doi:{10.1029/2020GL091747}.

Dosser, H. V., and L. Rainville, 2016: Dynamics of the changing near-inertial internal wave field in the Arctic Ocean. *Journal of Physical Oceanography*, **46 (2)**, 395–415, doi:{10.1175/JPO-D-15-0056.1}.

Dufresne, J.-L., and S. Bony, 2008: An assessment of the primary sources of spread of global warming estimates from coupled atmosphere-ocean models. *Journal of Climate*, **21 (19)**, 5135–5144, doi:{10.1175/2008JCLI2239.1}.

Eisenman, I., 2012: Factors controlling the bifurcation structure of sea ice retreat. *Journal of Geophysical Research-Atmospheres*, **117**, doi:{10.1029/2011JD016164}.

Eisenman, I., and J. S. Wettlaufer, 2009: Nonlinear threshold behavior during the loss of Arctic sea ice. *Proceedings of the National Academy of Sciences of the United States of America*, **106 (1)**, 28–32, doi:{10.1073/pnas.0806887106}.

England, M. R., I. Eisenman, N. J. Lutsko, and T. J. W. Wagner, 2021: The recent emergence of arctic amplification. *Geophysical Research Letters*, **48 (15)**, doi:10.1029/2021GL094086.

Feldl, N., S. Po-Chedley, H. K. A. Singh, S. Hay, and P. J. Kushner, 2020: Sea ice and atmospheric circulation shape the high-latitude lapse rate feedback. *NPJ Climate and Atmospheric Science*, **3 (1)**, doi:{10.1038/s41612-020-00146-7}.

Fer, I., 2009: Weak vertical diffusion allows maintenance of cold halocline in the central Arctic. *Atmospheric and Oceanic Science Letters*, **2 (3)**, 148–152, doi:{10.1080/16742834.2009.11446789}.

Fine, E. C., M. H. Alford, J. A. MacKinnon, and J. B. Mickett, 2021: Microstructure mixing observations and finescale parameterizations in the Beaufort Sea. *Journal of Physical Oceanography*, **51 (1)**, 19–35, doi:{10.1175/JPO-D-19-0233.1}.

Fine, E. C., and S. T. Cole, 2022: Decadal observations of internal wave energy, shear, and mixing in the western Arctic Ocean. *Journal of Geophysical Research-Oceans*, **127 (5)**, doi:10.1029/2021JC018056.

Flannery, B., 1984: Energy-balance models incorporating transport of thermal and latent energy. *Journal of the Atmospheric Sciences*, **41 (3)**, 414–421, doi:{10.1175/1520-0469(1984)041⟨0414:EBMITO⟩2.0.CO;2}.

Flato, G., J. Marotzke, B. Abiodun, P. Braconnot, S. Chou, W. Collins, P. Cox, F. Driouech, S. Emori, V. Eyring, C. Forest, P. Gleckler, E. Guilyardi, C. Jakob, V. Kattsov, C. Reason, and M. Rummukainen, 2013: Evaluation of climate models. *Climate Change 2013: The Physical Science Basis. Contribution of Working Group I to the Fifth Assessment Report of the Intergovernmental Panel on Climate Change*, T. Stocker, D. Qin, G.-K. Plattner, M. Tignor, S. Allen, J. Boschung, A. Nauels, Y. Xia, V. Bex, and P. M. (eds.), Eds., Cambridge University Press, Cambridge, United Kingdom and New York, NY, USA, book section 9, 741–866, doi:10.1017/CBO9781107415324.020, URL www.climatechange2013.org.

Francis, J. A., and E. Hunter, 2006: New insight into the disappearing Arctic sea ice. *Eos, Transactions American Geophysical Union*, **2006 (46)**, 509–511.

Goosse, H., J. E. Kay, K. C. Armour, A. Bodas-Salcedo, H. Chepfer, D. Docquier, A. Jonko, P. J. Kushner, O. Lecomte, F. Massonnet, H.-S. Park, F. Pithan, G. Svensson, and M. Vancoppenolle, 2018: Quantifying climate feedbacks in polar regions. *Nature Communications*, **9**, doi:{10.1038/s41467-018-04173-0}.

Graversen, R. G., P. L. Langen, and T. Mauritsen, 2014: Polar amplification in CCSM4: Contributions from the lapse rate and surface albedo feedbacks. *Journal of Climate*, **27 (12)**, 4433–4450, doi:{10.1175/JCLI-D-13-00551.1}.

Graversen, R. G., T. Mauritsen, M. Tjernstrom, E. Kallen, and G. Svensson, 2008: Vertical structure of recent Arctic warming. *Nature*, **451 (7174)**, 53–U4, doi:{10.1038/nature06502}.

Graversen, R. G., and M. Wang, 2009: Polar amplification in a coupled climate model with locked albedo. *Climate Dynamics*, **33 (5)**, 629–643, doi:{10.1007/s00382-009-0535-6}.

Gregory, J., 2000: Vertical heat transports in the ocean and their effect an time-dependent climate change. *Climate Dynamics*, **16 (7)**, 501–515, doi:{10.1007/s003820000059}.

Hall, A., 2004: The role of surface albedo feedback in climate. *Journal of Climate*, **17 (7)**, 1550–1568, doi:{10.1175/1520-0442(2004)017⟨1550:TROSAF⟩2.0.CO;2}.

Held, I. M., and K. M. Shell, 2012: Using relative humidity as a state variable in climate feedback analysis. *Journal of Climate*, **25 (8)**, 2578–2582, doi:{10.1175/JCLI-D-11-00721.1}.

Held, I. M., and B. J. Soden, 2006: Robust responses of the hydrological cycle to global warming. *Journal of Climate*, **19 (21)**, 5686–5699, doi:{10.1175/JCLI3990.1}.

Held, I. M., M. Winton, K. Takahashi, T. Delworth, F. Zeng, and G. K. Vallis, 2010: Probing the fast and slow components of global warming by returning abruptly to preindustrial forcing. *Journal of Climate*, **23 (9)**, 2418–2427, doi:{10.1175/2009JCLI3466.1}.

Henry, M., and T. M. Merlis, 2019: The role of the nonlinearity of the Stefan-Boltzmann law on the structure of radiatively forced temperature change. *Journal of Climate*, **32 (2)**, 335–348, doi:{10.1175/JCLI-D-17-0603.1}.

Henry, M., T. M. Merlis, N. J. Lutsko, and B. E. J. Rose, 2021: Decomposing the drivers of polar amplification with a single-column model. *Journal of Climate*, **34 (6)**, 2355–2365, doi:{10.1175/JCLI-D-20-0178.1}.

Hind, A., Q. Zhang, and G. Brattstrom, 2016: Problems encountered when defining Arctic amplification as a ratio. *Scientific Reports*, **6**, doi:{10.1038/srep30469}.

Holland, M., and C. Bitz, 2003: Polar amplification of climate change in coupled models. *Climate Dynamics*, **21 (3-4)**, 221–232, doi:{10.1007/s00382-003-0332-6}.

Hwang, Y.-T., and D. M. W. Frierson, 2010: Increasing atmospheric poleward energy transport with global warming. *Geophysical Research Letters*, **37**, doi:{10.1029/2010GL045440}.

Hwang, Y.-T., D. M. W. Frierson, and J. E. Kay, 2011: Coupling between Arctic feedbacks and changes in poleward energy transport. *Geophysical Research Letters*, **38**, doi:{10.1029/2011GL048546}.

Jeevanjee, N., D. D. B. Koll, and N. Lutsko, 2021: "simpson's law" and the spectral cancellation

of climate feedbacks. *Geophysical Research Letters*, **48 (14)**, doi:{10.1029/2021GL093699}.

Kay, J. E., and A. Gettelman, 2009: Cloud influence on and response to seasonal Arctic sea ice loss. *Journal of Geophysical Research-Atmospheres*, **114**, doi:{10.1029/2009JD011773}.

Langen, P. L., R. G. Graversen, and T. Mauritsen, 2012: Separation of contributions from radiative feedbacks to polar amplification on an aquaplanet. *Journal of Climate*, **25 (8)**, 3010–3024, doi:{10.1175/JCLI-D-11-00246.1}.

Lee, J.-Y., J. Marotzke, G. Bala, L. Cao, S. Corti, J. P. Dunne, F. Engelbrecht, E. Fischer, J. C. Fyfe, C. Jones, and Coauthors, 2021: Future global climate: scenario-based projections and near-term information. *Climate Change 2021: The Physical Science Basis. Contribution of Working Group I to the Sixth Assessment Report of the Intergovernmental Panel on Climate Change*, V. Masson-Delmotte, P. Zhai, A. Pirani, S. Connors, C. Péan, S. Berger, N. Caud, Y. Chen, L. Goldfarb, M. Gomis, M. Huang, K. Leitzell, E. Lonnoy, J. Matthews, T. Maycock, T. Waterfield, O. Yelekçi, R. Yu, and B. Zhou, Eds., Cambridge University Press.

Levitus, S., and T. Boyer, 1994: World Ocean Atlas 1994. Volume 4. Temperature. Tech. rep., National Environmental Satellite, Data, and Information Service, Washington.

Levitus, S., R. Burgett, and T. P. Boyer, 1994: World Ocean Atlas 1994. Volume 3. Salinity. Tech. rep., National Environmental Satellite, Data, and Information Service, Washington.

Li, C., D. Notz, S. Tietsche, and J. Marotzke, 2013: The transient versus the equilibrium response of sea ice to global warming. *Journal of Climate*, **26 (15)**, 5624–5636, doi:10.1175/JCLI-D-12-00492.1.

Lin, R., and G. North, 1990: A study of abrupt climate change in a simple nonlinear climate model. *Climate Dynamics*, **4 (4)**, 253–261.

Lincoln, B. J., T. P. Rippeth, Y.-D. Lenn, M. L. Timmermans, W. J. Williams, and S. Bacon, 2016: Wind-driven mixing at intermediate depths in an ice-free Arctic Ocean. *Geophysical Research Letters*, **43 (18)**, 9749–9756, doi:{10.1002/2016GL070454}.

Liu, Q., A. V. Babanin, S. Zieger, I. R. Young, and C. Guan, 2016: Wind and wave climate in the Arctic Ocean as observed by altimeters. *Journal of Climate*, **29 (22)**, 7957–7975, doi:10.1175/JCLI-D-16-0219.1.

Lu, J., and M. Cai, 2009: A new framework for isolating individual feedback processes in coupled general circulation climate models. Part I: formulation. *Climate Dynamics*, **32 (6)**, 873–885, doi:{10.1007/s00382-008-0425-3}.

Mahlstein, I., and R. Knutti, 2011: Ocean heat transport as a cause for model uncertainty in projected arctic warming. *Journal of Climate*, **24 (5)**, 1451–1460, doi:{10.1175/2010JCLI3713.

1}.

Manabe, S., and R. Stouffer, 1980: Sensitivity of a global climate model to an increase of CO2 concentration in the atmosphere. *Journal of Geophysical Research-Oceans*, **85 (NC10)**, 5529–5554, doi:{10.1029/JC085iC10p05529}.

Manabe, S., and R. Wetherald, 1975: Effects of doubling CO2 concentration on climate of a general circulation model. *Journal of the Atmospheric Sciences*, **32 (1)**, 3–15, doi:{10.1175/1520-0469(1975)032⟨0003:TEODTC⟩2.0.CO;2}.

Manucharyan, G. E., and A. F. Thompson, 2022: Heavy footprints of upper-ocean eddies on weakened Arctic sea ice in marginal ice zones. *Nature Communications*, **13 (1)**, doi:10.1038/s41467-022-29663-0.

Merlis, T. M., 2014: Interacting components of the top-of-atmosphere energy balance affect changes in regional surface temperature. *Geophysical Research Letters*, **41 (20)**, 7291–7297, doi:{10.1002/2014GL061700}.

Merlis, T. M., and M. Henry, 2018: Simple estimates of polar amplification in moist diffusive energy balance models. *Journal of Climate*, **31 (15)**, 5811–5824, doi:{10.1175/JCLI-D-17-0578.1}.

Middlemas, E. A., J. E. Kay, B. M. Medeiros, and E. A. Maroon, 2020: Quantifying the influence of cloud radiative feedbacks on Arctic surface warming using cloud locking in an earth system model. *Geophysical Research Letters*, **47 (15)**, doi:{10.1029/2020GL089207}.

Morison, J., C. Long, and M. Levine, 1985: Internal wave dissipation under sea ice. *Journal of Geophysical Research-Oceans*, **90 (NC6)**, 1959–1966, doi:{10.1029/JC090iC06p11959}.

Myhre, G., D. Shindell, F.-M. Bréon, W. Collins, J. Fuglestvedt, J. Huang, D. Koch, J.-F. Lamarque, D. Lee, B. Mendoza, T. Nakajima, A. Robock, G. Stephens, T. Takemura, and H. Zhang, 2013: Anthropogenic and natural radiative forcing. *Climate Change 2013: The Physical Science Basis. Contribution of Working Group I to the Fifth Assessment Report of the Intergovernmental Panel on Climate Change*, T. Stocker, D. Qin, G.-K. Plattner, M. Tignor, S. Allen, J. Boschung, A. Nauels, Y. Xia, V. Bex, and P. M. (eds.), Eds., Cambridge University Press, Cambridge, United Kingdom and New York, NY, USA, book section 8.

Nishino, S., Y. Kawaguchi, J. Inoue, T. Hirawake, A. Fujiwara, R. Futsuki, J. Onodera, and M. Aoyama, 2015: Nutrient supply and biological response to wind-induced mixing, inertial motion, internal waves, and currents in the northern Chukchi Sea. *Journal of Geophysical Research-Oceans*, **120 (3)**, 1975–1992, doi:{10.1002/2014JC010407}.

North, G., 1975: Theory of energy-balance climate models. *Journal of the Atmospheric Sciences*, **32 (11)**, 2033–2043, doi:{10.1175/1520-0469(1975)032⟨2033:TOEBCM⟩2.0.CO;2}.

North, G., R. Cahalan, and J. Coakley, 1981: Energy-balance climate models. *Reviews of Geophysics*, **19 (1)**, 91–121, doi:{10.1029/RG019i001p00091}.

North, G., and J. Coakley, 1979: Differences between seasonal and mean annual energy-balance model calculations of climate and climate sensitivity. *Journal of the Atmospheric Sciences*, **36 (7)**, 1189–1204, doi:{10.1175/1520-0469(1979)036⟨1189:DBSAMA⟩2.0.CO;2}.

Nummelin, A., C. Li, and P. J. Hezel, 2017: Connecting ocean heat transport changes from the midlatitudes to the Arctic Ocean. *Geophysical Research Letters*, **44 (4)**, 1899–1908, doi:{10.1002/2016GL071333}.

Nummelin, A., C. Li, and L. H. Smedsrud, 2015: Response of Arctic Ocean stratification to changing river runoff in a column model. *Journal of Geophysical Research-Oceans*, **120 (4)**, 2655–2675, doi:{10.1002/2014JC010571}.

Peterson, A. K., I. Fer, M. G. McPhee, and A. Randelhoff, 2017: Turbulent heat and momentum fluxes in the upper ocean under Arctic sea ice. *Journal of Geophysical Research-Oceans*, **122 (2)**, 1439–1456, doi:{10.1002/2016JC012283}.

Pithan, F., and T. Mauritsen, 2014: Arctic amplification dominated by temperature feedbacks in contemporary climate models. *Nature Geoscience*, **7 (3)**, 181–184, doi:{10.1038/NGEO2071}.

Polyakov, I. V., A. V. Pnyushkov, and E. C. Carmack, 2018: Stability of the Arctic halocline: a new indicator of Arctic climate change. *Environmental Research Letters*, **13 (12)**, doi:{10.1088/1748-9326/aaecle}.

Polyakov, I. V., A. V. Pnyushkov, M. B. Alkire, I. M. Ashik, T. M. Baumann, E. C. Carmack, I. Goszczko, J. Guthrie, V. V. Ivanov, T. Kanzow, R. Krishfield, R. Kwok, A. Sundfjord, J. Morison, R. Rember, and A. Yulin, 2017: Greater role for Atlantic inflows on sea-ice loss in the Eurasian Basin of the Arctic Ocean. *Science*, **356 (6335)**, 285+, doi:{10.1126/science.aai8204}.

Polyakov, I. V., T. P. Rippeth, I. Fer, M. B. Alkire, T. M. Baumann, E. C. Carmack, R. Ingvaldsen, V. V. Ivanov, M. Janout, S. Lind, L. Padman, A. Pnyushkov, V, and R. Rember, 2020: Weakening of cold halocline layer exposes sea ice to oceanic heat in the eastern Arctic Ocean. *Journal of Climate*, **33 (18)**, 8107–8123, doi:{10.1175/JCLI-D-19-0976.1}.

Pörtner, H.-O., D. Roberts, V. Masson-Delmotte, P. Zhai, E. Poloczanska, K. Mintenbeck, M. Tignor, A. Alegría, M. Nicolai, A. Okem, and Coauthors, Eds., 2019: *IPCC, 2019: Technical Summary*.

Rainville, L., and R. A. Woodgate, 2009: Observations of internal wave generation in the seasonally ice-free Arctic. *Geophysical Research Letters*, **36**, doi:{10.1029/2009GL041291}.

Reigstad, M., P. Wassmann, C. Riser, S. Oygarden, and F. Rey, 2002: Variations in hydrography,

nutrients and chlorophyll a in the marginal ice-zone and the central Barents Sea. *Journal of Marine Systems*, **38 (1-2)**, 9–29, doi:{10.1016/S0924-7963(02)00167-7}.

Reynolds, R., and T. Smith, 1995: A high-resolution global sea-surface temperature climatology. *Journal of Climate*, **8 (6)**, 1571–1583, doi:{10.1175/1520-0442(1995)008⟨1571:AHRGSS⟩2.0.CO;2}.

Rippeth, T. P., B. J. Lincoln, Y.-D. Lenn, J. A. M. Green, A. Sundfjord, and S. Bacon, 2015: Tide-mediated warming of Arctic halocline by Atlantic heat fluxes over rough topography. *Nature Geoscience*, **8 (3)**, 191–194, doi:{10.1038/NGEO2350}.

Roe, G., 2009: Feedbacks, timescales, and seeing red. *Annual Review of Earth and Planetary Sciences*, **37**, 93–115, doi:{10.1146/annurev.earth.061008.134734}.

Roe, G. H., and M. B. Baker, 2007: Why is climate sensitivity so unpredictable? *Science*, **318 (5850)**, 629–632, doi:{10.1126/science.1144735}.

Roe, G. H., N. Feldl, K. C. Armour, Y.-T. Hwang, and D. M. W. Frierson, 2015: The remote impacts of climate feedbacks on regional climate predictability. *Nature Geoscience*, **8 (2)**, 135–139, doi:{10.1038/NGEO2346}.

Rose, B. E. J., K. C. Armour, D. S. Battisti, N. Feldl, and D. D. B. Koll, 2014: The dependence of transient climate sensitivity and radiative feedbacks on the spatial pattern of ocean heat uptake. *Geophysical Research Letters*, **41 (3)**, 1071–1078, doi:{10.1002/2013GL058955}.

Russotto, R. D., and M. Biasutti, 2020: Polar amplification as an inherent response of a circulating atmosphere: results from the TRACMIP aquaplanets. *Geophysical Research Letters*, **47 (6)**, doi:{10.1029/2019GL086771}.

Schweiger, A. J., R. W. Lindsay, S. Vavrus, and J. A. Francis, 2008: Relationships between Arctic sea ice and clouds during autumn. *Journal of Climate*, **21 (18)**, 4799–4810, doi:{10.1175/2008JCLI2156.1}.

Screen, J. A., and I. Simmonds, 2010: The central role of diminishing sea ice in recent Arctic temperature amplification. *Nature*, **464 (7293)**, 1334–1337, doi:{10.1038/nature09051}.

Sellers, W. D., 1969: A global climatic model based on the energy balance of the earth-atmosphere system. *Journal of Applied Meteorology*, **8 (3)**, 392–400.

Serreze, M., J. Walsh, F. Chapin, T. Osterkamp, M. Dyurgerov, V. Romanovsky, W. Oechel, J. Morison, T. Zhang, and R. Barry, 2000: Observational evidence of recent change in the northern high-latitude environment. *Climatic Change*, **46 (1-2)**, 159–207, doi:{10.1023/A:1005504031923}.

Siler, N., G. H. Roe, and K. C. Armour, 2018: Insights into the zonal-mean response of the hydrologic cycle to global warming from a diffusive energy balance model. *Journal of Climate*, **31 (18)**, 7481–7493, doi:{10.1175/JCLI-D-18-0081.1}.

Singh, H. A., P. J. Rasch, and B. E. J. Rose, 2017: Increased ocean heat convergence into the high latitudes with CO2 doubling enhances polar-amplified warming. *Geophysical Research Letters*, **44 (20)**, 10 583–10 591, doi:{10.1002/2017GL074561}.

Sirevaag, A., and I. Fer, 2009: Early spring oceanic heat fluxes and mixing observed from drift stations north of Svalbard. *Journal of Physical Oceanography*, **39 (12)**, 3049–3069, doi:{10.1175/2009JPO4172.1}.

Soden, B. J., and I. M. Held, 2006: An assessment of climate feedbacks in coupled ocean-atmosphere models (vol 19, pg 3354, 2006). *Journal of Climate*, **19 (23)**, 6263, doi:{10.1175/JCLI9028.1}.

Spielhagen, R. F., K. Werner, S. A. Sorensen, K. Zamelczyk, E. Kandiano, G. Budeus, K. Husum, T. M. Marchitto, and M. Hald, 2011: Enhanced modern heat transfer to the Arctic by warm Atlantic Water. *Science*, **331 (6016)**, 450–453, doi:{10.1126/science.1197397}.

Stuecker, M. F., C. M. Bitz, K. C. Armour, C. Proistosescu, S. M. Kang, S.-P. Xie, D. Kim, S. McGregor, W. Zhang, S. Zhao, W. Cai, Y. Dong, and F.-F. Jin, 2018: Polar amplification dominated by local forcing and feedbacks. *Nature Climate Change*, **8 (12)**, 1076+, doi:{10.1038/s41558-018-0339-y}.

Taylor, K. E., R. J. Stouffer, and G. A. Meehl, 2012: An overview of CMIP5 and the experiment design. *Bulletin of the American Meteorological Society*, **93 (4)**, 485–498, doi:{10.1175/BAMS-D-11-00094.1}.

Taylor, P. C., M. Cai, A. Hu, G. A. Meehl, W. Washington, and G. J. Zhang, 2013: A decomposition of feedback contributions to polar warming amplification (vol 26, pg 7023, 2013). *Journal of Climate*, **26 (21)**, 8706, doi:{10.1175/JCLI-D-13-00511.1}.

Thorndike, A., 1992: A toy model linking atmospheric thermal-radiation and sea ice growth. *Journal of Geophysical Research-Oceans*, **97 (C6)**, 9401–9410, doi:{10.1029/92JC00695}.

Timmermans, M., J. Toole, R. Krishfield, and P. Winsor, 2008: Ice-tethered profiler observations of the double-diffusive staircase in the Canada Basin thermocline. *Journal of Geophysical Research-Oceans*, **113**, doi:{10.1029/2008JC004829}.

Timmermans, M.-L., and J. Marshall, 2020: Understanding Arctic Ocean circulation: A review of ocean dynamics in a changing climate. *Journal of Geophysical Research-Oceans*, **125 (4)**, doi:{10.1029/2018JC014378}.

Timmermans, M.-L., J. Toole, and R. Krishfield, 2018: Warming of the interior Arctic Ocean linked to sea ice losses at the basin margins. *Science Advances*, **4 (8)**, doi:{10.1126/sciadv.aat6773}.

Timmermans, M.-L., A. Proshutinsky, E. Golubeva, J. M. Jackson, R. Krishfield, M. McCall, G. Platov, J. Toole, W. Williams, T. Kikuchi, and S. Nishino, 2014: Mechanisms of Pacific Summer Water variability in the Arctic's central Canada Basin. *Journal of Geophysical Research-Oceans*, **119 (11)**, 7523–7548, doi:{10.1002/2014JC010273}.

van der Linden, E. C., D. Le Bars, R. Bintanja, and W. Hazeleger, 2019: Oceanic heat transport into the Arctic under high and low CO2 forcing. *Climate Dynamics*, **53 (7-8)**, 4763–4780, doi:{10.1007/s00382-019-04824-y}.

Wagner, T. J. W., and I. Eisenman, 2015: How climate model complexity influences sea ice stability. *Journal of Climate*, **28 (10)**, 3998–4014, doi:{10.1175/JCLI-D-14-00654.1}.

Winton, M., 2006: Amplified Arctic climate change: What does surface albedo feedback have to do with it? *Geophysical Research Letters*, **33 (3)**, doi:{10.1029/2005GL025244}.

Zelinka, M. D., T. A. Myers, D. T. Mccoy, S. Po-Chedley, P. M. Caldwell, P. Ceppi, S. A. Klein, and K. E. Taylor, 2020: Causes of higher climate sensitivity in CMIP6 models. *Geophysical Research Letters*, **47 (1)**, doi:{10.1029/2019GL085782}.

Zhang, J., and D. Rothrock, 2003: Modeling global sea ice with a thickness and enthalpy distribution model in generalized curvilinear coordinates. *Monthly Weather Review*, **131 (5)**, 845–861, doi:{10.1175/1520-0493(2003)131⟨0845:MGSIWA⟩2.0.CO;2}.